The LHCb SciFi Tracker: studies on scintillating fibres and development of quality assurance procedures for the SciFi serial production

Dissertation
zur Erlangung des akademischen Grades
Dr. rer. nat.

vorgelegt von
Janine Menne
geboren am 27.11.1989 in Herborn

Fakultät Physik
Technische Universität Dortmund

Dortmund im März 2018

Der Fakultät Physik der Technischen Universität Dortmund zur Erlangung des akademischen Grades eines Doktors der Naturwissenschaften vorgelegte Dissertation.

1. Gutachter: Prof. Dr. Spaan
2. Gutachter: Prof. Dr. Kröninger

Datum des Einreichens der Arbeit: 05.03.2018
Datum der mündlichen Prüfung: 02.05.2018

Abstract

For 2019 an upgrade of the LHCb detector is foreseen. The tracking stations behind the magnet will be replaced by a detector made of scintillating fibres with a silicon photomultiplier read out. To achieve a spatial resolution better than $100\,\mu m$, fibres with a diameter of $250\,\mu m$ are accurately positioned in several layers and glued to $2.4\,m$ long mats. To ensure a proper quality of these fibre mats quality assurance during the production of these mats is mandatory.

This thesis presents quality assurance procedures which were developed for the serial production of the Scintillating Fibre (SciFi) Tracker. In the production scintillating fibres are wound on a threaded wheel. To directly check the winding procedure, a live monitoring setup including a software based on machine learning and image recognition has been developed. The introduced quality assurance procedures enabled a smooth running serial production with high quality fibre mats.

An essential parameter to assess the quality is the light yield of a fibre mat. The mean light yield loss at the end of the nominal lifetime of the SciFi tracker obtained from simulations is about 35%. An in situ irradiation campaign in the LHCb cavern monitoring the radiation damage over time is presented in this thesis. The obtained results confirm results from simulations based on former irradiation campaigns.

Kurzfassung

Für das Jahr 2019 ist ein Upgrade des LHCb Detektors geplant. Die Trackingstationen hinter dem Magneten sollen dabei durch einen Detektor aus szintillierenden Fasern mit Silizium-Photomultiplier-Auslese ersetzt werden. Um die gewünschte Ortsauflösung von unter $100\,\mu m$ zu erreichen, werden Fasern mit einem Durchmesser von $250\,\mu m$ präzise in mehreren Lagen positioniert und zu $2.4\,m$ langen Matten verklebt. Qualitätskontrollen während der Produktion der Fasermatten sind zwingend notwendig, um eine hohe Qualität der Fasermatten zu gewährleisten.

In dieser Arbeit werden Qualitätskontrollen diskutiert, die für die Serienproduktion des Scintillating Fibre (SciFi) Trackers entwickelt wurden. Für die Produktion von Fasermatten werden die szintillierenden Fasern auf ein Rad mit einem Gewinde gewickelt. Innerhalb dieser Arbeit wurde eine Kameraüberwachung basierend auf maschinellem Lernen und Bilderkennung entwickelt, welche diesen Produktionschritt überwacht. Alle hier vorgestellten Qualitätskontrollen ermöglichen eine problemlos laufende Serienproduktion und Fasermatten von hoher Qualität.

Ein wichtiger Parameter für die Qualität einer Fasermatte ist die Lichtausbeute. Simulationen zeigen einen Lichtverlust von 35% am Ende der nominellen Laufzeit des SciFi Trackers. Im Rahmen dieser Arbeit wird eine in situ Bestrahlung in der LHCb Kaverne vorgestellt, bei der der Strahlenschaden über die Zeit aufgenommen wurde. Die gewonnenen Ergebnisse entsprechen denen der Simulationen und damit auch früheren Bestrahlungskampagnen.

Contents

1. Introduction

All existing matter was created from energy in the Big Bang at the beginning of the universe. As matter and antimatter can only be produced in equal parts, it remains one of the major challenges in modern physics to explain why almost no antimatter can be observed in today's universe. A promising approach to resolve this discrepancy is the study of CP violation, which is an asymmetry in the laws of nature, causing particles and antiparticles to interact differently. Therefore, precision measurements of CP violation are performed at high energies. The Large Hadron Collider at CERN near Geneva in Switzerland provides four large experiments with collisions of very high energetic protons. In a circular tunnel with a circumference of about 27 km proton bunches collide up to 40 million times a second. Each of these collisions produces various short-lived particles which decay within the detectors. The LHCb experiment is one of those major experiments. It is a forward spectrometer specialised to the search for New Physics by precision measurements of CP violation, especially in B meson decays. Every second 4000 events are recorded and stored on large computing farms.

A fast, high resolution tracking system is necessary to allow for these precision measurements at a high rate. The current tracking system behind the magnet consists of the combination of the silicon strip Inner Tracker and the drift tube Outer Tracker. The higher read out rate of 40 MHz and higher multiplicities at the upgrade conditions require a replacement of these. A tracking detector made of scintillating fibres and silicon photomultipliers is planned to improve LHCb's current tracking system within the 2019 upgrade and will enable the detector to work with increasing event rates. Scintillating fibres will be arranged in mats consisting of six layers of fibres. With a diameter of 250 μm the scintillating fibres utilised in the so-called scintillating fibre (SciFi) Tracker will increase the granularity and therefore ensure a spatial resolution of below 100 μm.

During the scope of this thesis several contributions to the LHCb SciFi Tracker have been made. The main responsibility was set up of the serial production of fibre mats in Dortmund. During this work quality assurance and quality measurement procedures for the serial production have been developed as well as studies on the quality of fibre mats been performed. In addition, R&D investigations on single scintillating fibres have been done. Measurements on different impacts on the fibres have been studied as well as an in situ irradiation campaign in the LHCb cavern performed, which shows the radiation damage over time.

The first chapter of this thesis gives a short introduction to the physics at the LHC and the second chapter introduces the LHCb detector. In Chap. 4, the LHCb SciFi Tracker is introduced and the requirements for a tracker upgrade are described. Chapter 5 focusses on the serial production of fibre mats and illustrates the different procedures. In the following Chap. 6 the properties of scintillating fibres are described and the performed studies on single scintillating fibres, such as an irradiation campaign, are presented. Chapter 7 explains the quality assurance during the serial production of fibre mats and presents the developed procedures and performed studies.

2. Physics at the Large Hadron Collider

The Large Hadron Collider (LHC) is the world's largest and most powerful hadronic particle accelerator. It is operated by CERN[1] near Geneva, Switzerland. With its four large detectors LHCb, ATLAS, CMS and ALICE proton-proton collisions as well as ion collisions are recorded. This data allows a wide physics program for the experiments. This chapter gives an overview over the LHC and shortly introduce the physics. The information given in this chapter is mainly inspired by the description in Ref. [1] and Ref. [2].

2.1. The Standard Model of particle physics

The Standard Model of particle physics represents the state-of-the-art theory in the field of particle physics. It describes three of the four known fundamental forces, namely the weak, strong and electromagnetic interactions, omitting gravity, but as well all known elementary particles in the universe. The Standard Model includes several classes of elementary particles, which are either fermions with a half-integer spin or bosons with integer spin. Quarks and leptons are fermions which can be arranged into three generations as shown in Fig. 2.1. The corresponding antifermions have the same mass,
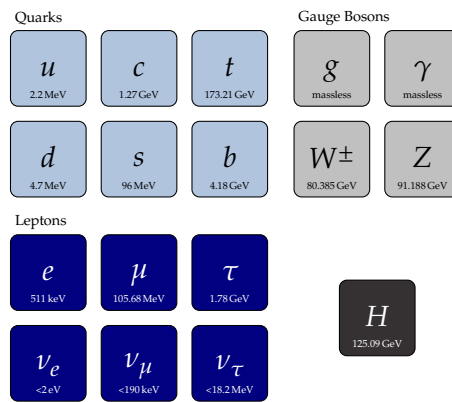
Fig. 2.1.: Fundamental particles, gauge bosons and Higgs boson described by the Standard Model. Information from [3].

but opposite charge and spin. There are six different types of quarks: up, down, strange, charm, top, and bottom with a respective feature called flavour. Quarks are carrying colour charge to which gluons are coupling. Because of the colour confinement, quarks are strongly bound together and form colour-neutral composite particles called hadrons. Hadrons containing a quark and an antiquark form mesons and hadrons made from three quarks are called baryons. Six different types of leptons are included in the Standard Model: electron, muon, tau with their corresponding neutrinos. Leptons do not carry

---

[1]European Organization for Nuclear Research

colour charge but interact via the weak and electromagnetic force. Neutrinos do not carry electric charge either, so that their interactions are only driven by the weak force. However, due to carrying electric charge, the electron, muon and tau all interact via the electromagnetic force. As the particles of the first generation are the lightest ones and are therefore stable, all known matter consists of up and down quarks, which combine to protons (*uud*) and neutrons (*ddu*), and electrons.

Gauge bosons mediate the forces between those fermions. The properties of the interaction of particles are determined by their attributes. So called Feynman diagrams are a graphical visualization of the mathematical description of these interactions. The eight gluons mediate the strong force between colour charged particles with a small range. The electromagnetical force is mediated by massless photons, which is well described by the theory of quantum electrodynamics and has an in principle infinity range. The $W^{\pm}$ and Z bosons mediate the weak interactions between particles of different flavour and therefore allow a change of the flavour and to break *CP* symmetry. Due to the high mass of these bosons, the range of the weak force is very limited. The discovery of the Higgs boson at the LHC in 2012 [4, 5] completed the Standard Model with the last predicted fundamental particle. Theorized by Peter Higgs in 1964 [6] the Higgs field plays a unique role in the Standard Model, by explaining how the elementary particles gain their masses.

The Standard Model is a theory of great success, as all measurements are well within the prediction. Despite its accuracy in describing particles and forces on a subatomic level, the Standard Model cannot be considered a complete theory. Many observations have been made, which are not included in the Standard Model: gravity and neutrino masses, as well as dark energy and dark matter. These observations and the corresponding open questions demand new theories beyond the reach of the Standard Model, so-called new physics models.

2.2. The LHC accelerator complex

The LHC and its experiments is designed to enable the search for New Physics at unprecedented centre-of-mass energies and luminosities. It is a proton-proton ring accelerator installed in the existing tunnel of the former accelerator LEP (Large Electron Positron Collider). A sketch of the whole accelerator complex is shown in Fig. 2.2. The information is mostly obtained from [7].

The design centre-of-mass energy of up to 14 TeV with a luminosity of $10^{34}\,\mathrm{cm^{-2}\,s^{-1}}$ can only be reached with superconducting magnets which have to be cooled with super fluid helium to a temperature below 2 K. In addition, space and cost limitations required to adopt a two-in-one design for almost all LHC magnets. This design holds the two beam channels in a common cold mass and cryostat [7]. The LHC is arranged in eight arcs and eight straight sections. The two high luminosity experiments ATLAS and CMS are located at diametrically opposite straight sections. ATLAS is situated at Point 1 and CMS at Point 5. LHCb and ALICE are located at Point 8 and Point 2, which also include the injections points, respectively.

Protons are accelerated and brought to collision inside the four experiments with an angle of 150 to 200 µrad [7]. First, the protons need to be pre-accelerated before entering the LHC. A chain of smaller accelerators (LINAC2, BOOSTER, PS and SPS) fills the LHC with 2808 bunches of about 10^{11} protons each and a bunch spacing of 25 ns. This
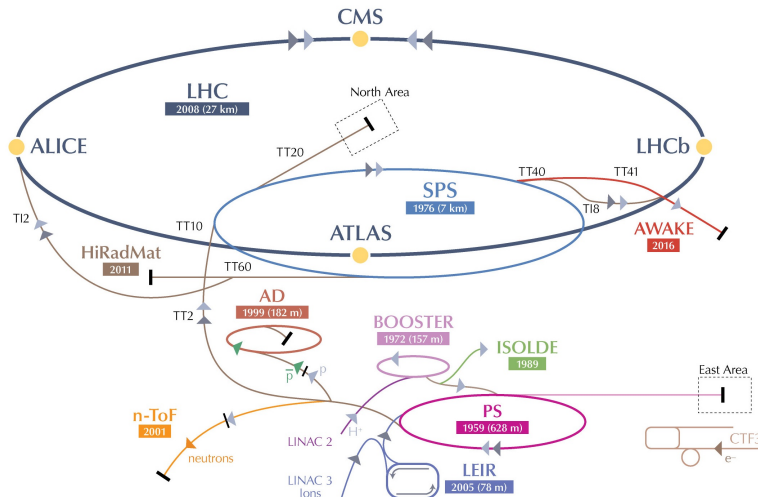
Fig. 2.2.: CERN's accelerator complex with its four large experiments ALICE, ATLAS, CMS and LHCb as well as the pre-accelerators SPS, PS, BOOSTER and LINAC2 [8].

corresponds to a maximum bunch crossing rate of 40 MHz [7]. The LHC is also able to be filled with heavy ions. Mostly the ALICE experiment is interested in these collisions, but also ATLAS, CMS and LHCb are using this data for their physics goals. Operating in this mode, centre-of-mass energies up to 1.15 PeV can be reached. The LHC is currently performing Run II, which will be followed by the Long Shutdown 2 (LS2) beginning of 2019. During this two year long shutdown of the LHC, several detectors will undergo an upgrade to reach their physics goals. The upgrade of the LHCb detector, which will take place during LS2 is further explained in Chap. 3.

2.3. The LHC experiments

The physics goal of all experiments is to measure the parameters of the Standard Model to a precise level and to make possible deviations from the theory predictions visible. ATLAS [9] and CMS [10] are the largest experiments with multi-purpose detectors to cover a wide physics spectrum. The search for the Standard Model Higgs boson is an important benchmark for these two experiments and establish the performance of their detectors. In 2012, a Higgs-like particle has been found [4, 5] and with more data available in 2013, the properties of this particle were determined, which are in agreement with the Standard Model Higgs boson [6, 11]. ALICE [12] is a general-purpose detector specialised for heavy-ion collisions. It is designed to focus on the strong interaction sector of the Standard Model and the physics of a quark-gluon plasma. However, it also takes data and performs analyses with proton beams to address several QCD topics for which ALICE is complementary to the other LHC experiments. The LHCb experiment [13] is dedicated to high precision measurements in heavy flavour physics. The main goal is to find evidence for new phenomena in CP violation and rare decays of beauty and charm hadrons. At the birth of our universe, 13.8 billion years ago [14], matter and antimatter have been created in equal parts. Today we are only surrounded by matter and no antimatter clusters were found. One possible explanation for this observation is the so-called CP violation, the combination of charge conjugation and parity symmetry. Previous results from other

experiments are consistent with the Standard Model prediction, however, this level of $C\!P$ violation cannot explain this mismatch of matter and antimatter. Many models of new physics show contributions of a new source of $C\!P$ violation, which should be visible in the LHCb observables [13].

The detectors of the LHC are dedicated to record the decay product of the particle collisions and to cope with the high bunch crossing rate of up to 40 MHz with high multiplicities. With up to 10^9 observed inelastic events per second and 1000 charged particles per bunch crossing, there is huge requirement to a fast read-out system. The amount of particles crossing the detector demand high-granularity tracking detectors to ensure high spatial resolution. The general purpose detectors (ATLAS, CMS and ALICE) are designed to have a large geometric coverage and a good calorimetry system to calculate missing energy in events. These so-called 4π detectors are arranged in a cylindrical way around the beam pipe (see Fig. 2.3 as example). In principle, the sub-detectors can be
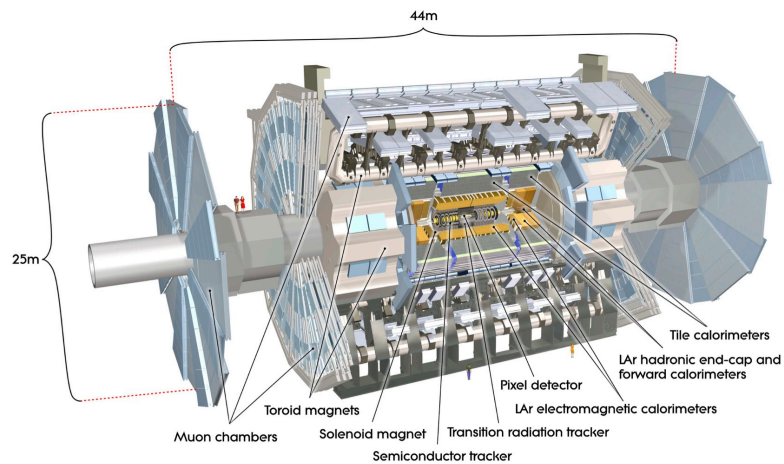
Fig. 2.3.: Cut-away view of the ATLAS detector. [9].

classified into two groups: track finding and particle identification. To have a sufficient tracking, these detectors are located closely to the interacting point, which allows to determine the decay vertices. With the help of a magnet, which bends the tracks of the produced charged particles, also their momentum can be measured. Electromagnetic and hadronic calorimeters allow to determine the energy of the respectively interacting particle. As muons are not absorbed by such calorimeters, they are detected by specialised muon chambers, which are the outermost sub-detectors. The LHCb detector (Fig. 3.1) is designed as a single-arm forward spectrometer optimised for the study of the decay of B hadrons. The b quark production at the LHC is dominated by gluon-gluon fusion in which the momenta of the gluons show a strong asymmetry. This leads to a centre-of-mass energy of the produced $b\bar{b}$ pair, which is boosted along the direction of the higher momentum gluon. It is very likely that both b hadrons are produced in small angles in the same forward (or backward) direction [16]. Despite its very small acceptance of 10 mrad to 300 mrad (4% of the solid angle) 24% of all $b\bar{b}$ pairs produced in pp collision with an energy of 14 TeV are decaying inside the LHCb detector [17] as shown in Fig. 2.5. For more details on the LHCb detector see Chap. 3.
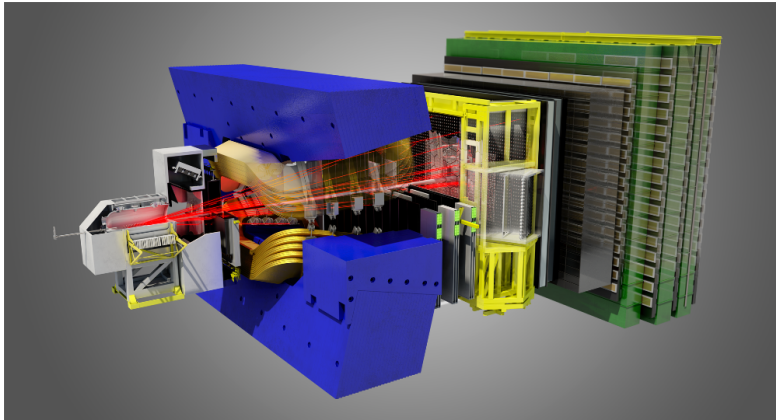
Fig. 2.4.: Cut-away view of the LHCb detector [15].
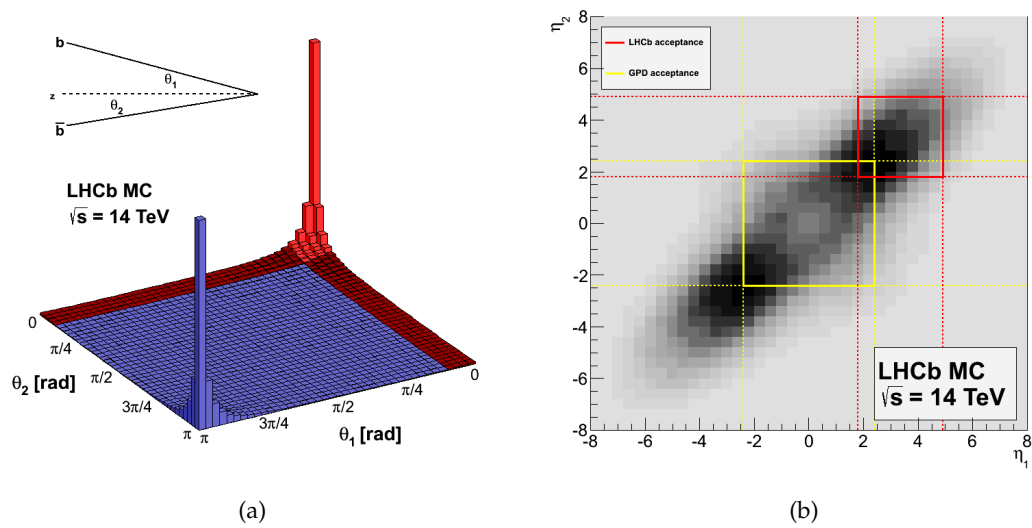

| (a) | (b) |

Fig. 2.5.: $b\bar{b}$ production angles at $\sqrt{s} = 14\,\text{TeV}$ created with PYTHIA [17]. (a) Number of produced $b\bar{b}$ pairs as a function of the angles θ_1 and θ_2 (b) and as the pseudo rapidity η. The LHCb acceptance is marked in red.

3. The LHCb experiment

The LHCb experiment is one of the four large experiments at the LHC accelerator at CERN in Geneva, Switzerland. It is dedicated to test the Standard Model of particle physics by performing indirect searches for New Physics. The main goal of the LHCb experiment is to investigate *CP* violation in the *b* and *c* quark sector as well as rare decays of *B* mesons [13]. With the world's largest sample of charm and beauty decays collected during Run I, LHCb was able to perform a lot of measurements. An upcoming detector upgrade is able to significantly lower the statistical uncertainties by a major increase of the data sample. This chapter describes the current LHCb detector and motivates the size of the LHCb upgrade.

3.1. The LHCb detector

The LHCb detector, illustrated in Fig. 3.1, is a single-arm forward spectrometer [13], *i.e.* its sub-detectors are not arranged around the interaction point but successively in the forward direction. Designed as such, it is covering an angular range from 10 mrad to 300 mrad (250 mrad) in the bending (non-bending) plane. This corresponds to a pseudo rapidity range of $2 < \eta < 5$ and approx. 4% of the solid angle [13]. With this acceptance
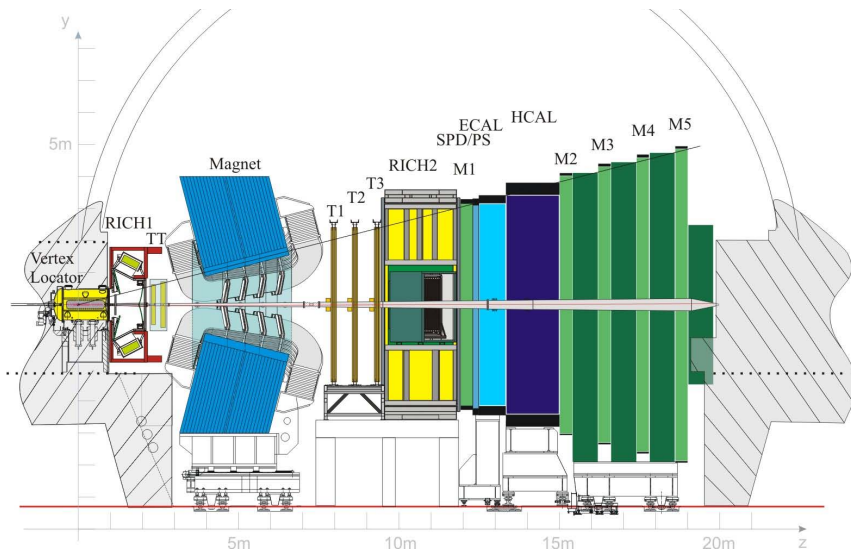
Fig. 3.1.: Schematic view of the LHCb detector [13]. The tracking system consists of VELO, TT and the Tracking Stations T1, T2, T3. An assignment of momenta for charged particles is done with the help of a dipole magnet. A particle identification is done via several calorimeters, PS/SPD, electromagnetic (ECAL) and hadronic (HCAL) calorimeter and the two RICH detectors. To identify muons the muon stations (M1- M5) are used.

and the fact that in high energy *pp* collisions $b\bar{b}$ pairs are predominantly produced in the same forward or backward direction the LHCb detector can measure 24% of the

produced $b\bar{b}$ pairs, see Fig. 2.5 [17]. The sub-detectors can be classified into two groups, track finding and particle identification and are described in the following, based on the informations from Refs. [13, 18].

3.1.1. Tracking

There are multiple tracking detectors at LHCb. The closest detector to the interacting point is the Vertex Locator (VELO). The Tracker Turicensis (TT) is placed in front of the dipole magnet and the Tracking Stations (T1, T2, T3) behind it. The dipole magnet provides an integrated field of 4 T m to bend charged tracks and hence to determine the momenta of charged particles.

Vertex Locator (VELO)
The VELO surrounds the interaction point at LHCb and provides precise measurements of track coordinates of the primary pp interaction as well as of the displaced c- and b-hadron decays. It is a silicon strip detector with modules arranged in a series along the beam axis, see Fig. 3.2. Each module provides a measurement of the r and ϕ coordinates
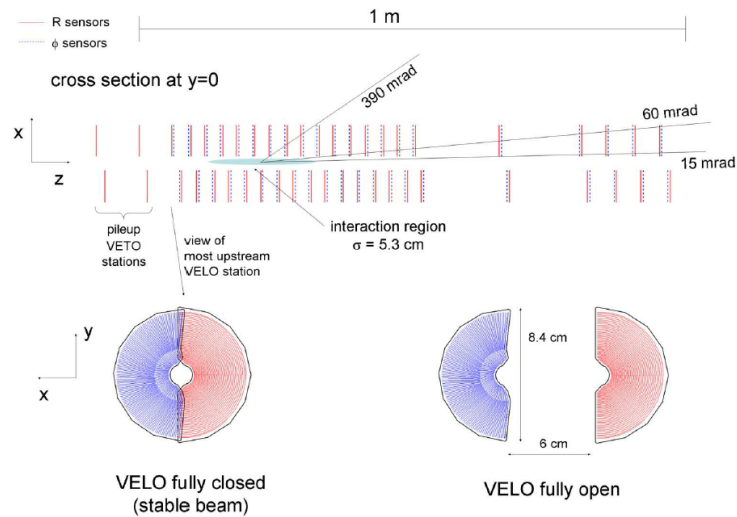
Fig. 3.2.: (top) Arrangement of the VELO modules along the beam axis. (bottom) Fully closed VELO, during stable beams and fully open VELO [13].

with a strip pitch of 38 to 102 μm. To be able to come as closely as possible to the interaction point the beam pipe is interrupted by a vacuum vessel containing the VELO detector. Its aperture is smaller than required by the LHC during injection. Hence, the VELO is designed as two halves, which can be moved in and out, with a minimum distance to the beam axis of 8 mm. The VELO reaches a single hit resolution of up to 4 μm and a hit efficiency of 99% [18].

To protect the most sensitive component of the LHCb detector, a Beam Conditions Monitor (BCM) [19] based on diamond sensors was installed. It continuously monitors the particle flux at two locations in close vicinity of the beam pipe. In case of abnormal beam conditions, the VELO modules are moved out and a beam dump triggered.

Tracker Turicencis (TT)

The TT consists of four layers of silicon micro-strip sensors with a pitch of about 200 µm. It serves mainly for the tracking of low energy particles. These particles suffer a strong bending in the magnetic field and are not crossing the following Tracking Stations T1 to T3 anymore. But also tracking of high energy particles is performed with this detector. Each station covers a plane of 150×130 cm². The four layers are arranged with a *x-u-v-x* geometry meaning that the first and the last layer having vertical strips and the middle ones tilted with a stereo angle of −5° and 5°, respectively. This arrangement enables a sensitivity in the *y*-direction.

Tracking Stations T1, T2, T3

All three Tracking Stations are built the same way and are split into two different detectors. The Inner Tracker (IT), which is silicon strip detector similar to the TT and the Outer Tracker (OT) which is a drift tube detector. Each station has four layers with a *x-u-v-x*

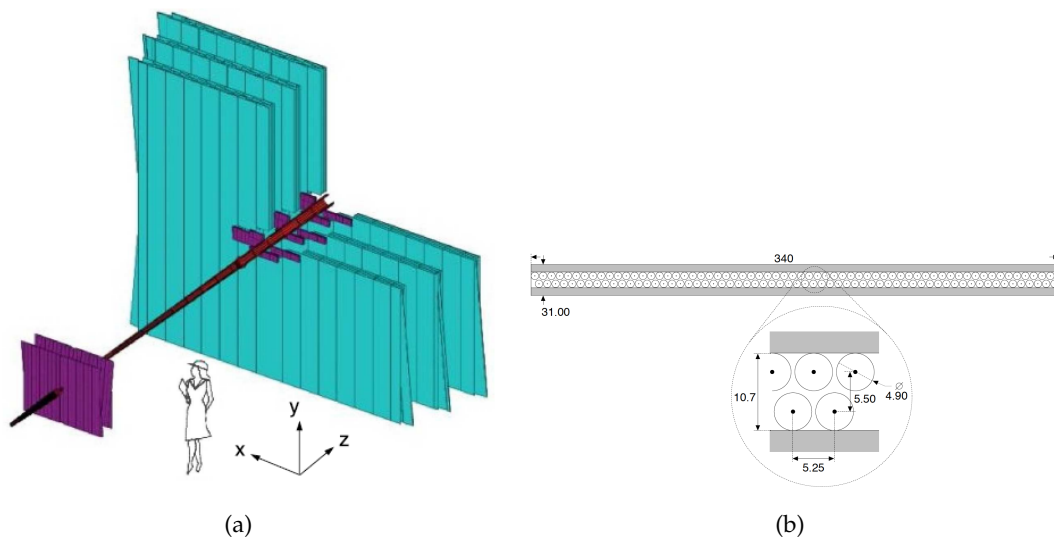(a)   (b)

Fig. 3.3.: (a) Tracking Stations T1, T2, T3 and the TT. The Outer Tracker is coloured cyan while the Inner Tracker and the Tracker Turicensis are coloured purple. A square got cut away on the upper right side to have a better visibility [13]. (b) Schematic view of the drift tubes of the Outer Tracker [13].

geometry and the IT mounted in the center of the OT, see Fig. 3.3. The IT is located close to the beam pipe and covers the region with a high track density. This silicon strip detector with a pitch of about 200 µm has a 120×40 cm² cross shape and covers an active area of 4 m². During Run I the hit efficiencies of the TT and IT were greater than 99.7% and the resolutions between 50 µm and 55 µm [18].

The OT consists of two staggered layers of drift tubes, which are flushed with a gas mixture of Argon (70%), CO_2 (28.5%) and O_2 (1.5%). The detector spans an area of about 6×5 m², where the outer boundary corresponds to the LHCb acceptance. The 200 gas-tight modules house the tubes with 4.9 mm diameter, which achieve drift times below 50 ns and a spatial resolution of about 200 µm [20]. For the current tracking system the momentum resolution, $\Delta p/p$, ranges from 0.4% at 5 GeV/c to 0.6% at 100 GeV/c. For $B \rightarrow J/\psi X$ decays an invariant mass resolution of 8 MeV have been achieved [18].

3.1.2. Particle identification

Particle identification is a basic requirement for the physics goals of the experiment. Hence it is essential to distinguish *e.g.* kaons from pions in *B*-hadron decays.

Ring Imaging Cherenkov detectors (RICH)
The two Ring Imaging Cherenkov detectors RICH1 and RICH2 are used for charged hadron identification. The upstream detector RICH1 is situated in front of the TT and covers the low momentum particles in a range from 1 to 60 GeV/c, while the downstream detector RICH2 covers the high momentum range up to 100 GeV/c and is located behind the Tracking Stations. RICH1 uses C_4F_{10} as a radiator and CF_4 is used in RICH2.

(a) RICH1 (side view)   (b) RICH2 (top view)
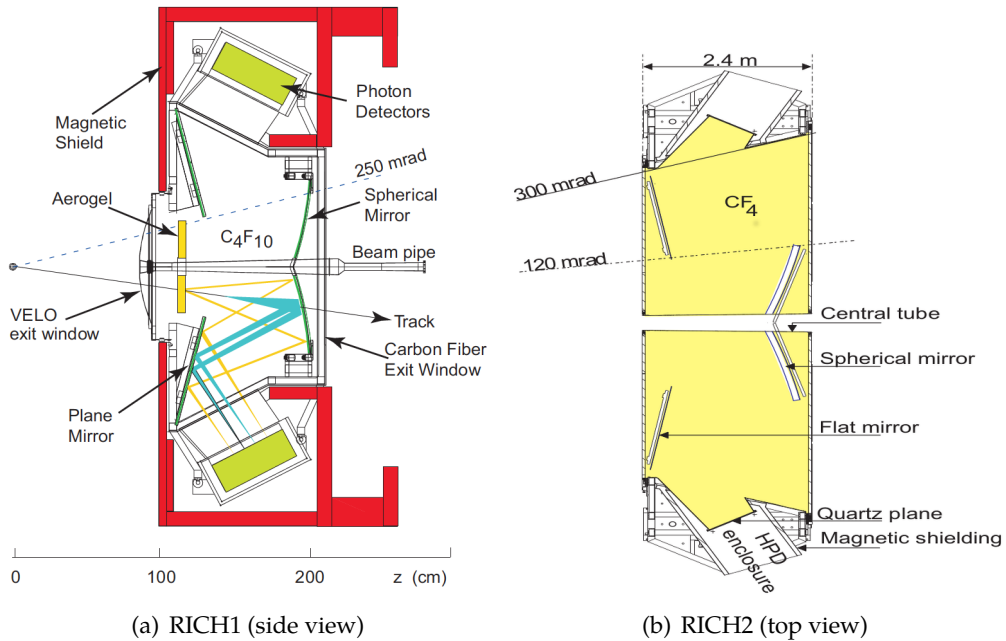
Fig. 3.4.: Schematic view of the two RICH detectors [13]. Crossing particles emit light due to the Cherenkov effect, which is transferred via mirrors to photon detectors.

Charged particles emit electromagnetic radiation passing through a dielectric medium at a speed greater than the speed of light in that medium. A combination of spherical and flat mirrors is used to collect the emitted light and transfer it to the so-called HPDs (Hybrid Photon Detectors). A special cylindrical shield permits the operation of the HPDs up to 50 mT in a range of 200 to 600 nm. The combination with the momentum information provided by the tracking system allows to corroborate a particle hypothesis. Figure 3.4 displays a schematic of the two RICH detectors.

Calorimeters
The calorimeter system performs several functions, such as selecting the transverse energy candidate for the first level trigger (L0) and providing the identification of electrons, photons and hadrons as well as the measurement of their energies and location. One of the two main components is the electromagnetic calorimeter (ECAL), which is placed

at 12.5 m distance to the interaction point. Its purpose is to identify electrons and photons. The energy of protons, neutrons and other long-lived hadrons is measured by the hadronic calorimeter (HCAL).

Both calorimeters are following the same principle: stacked layers of absorbers and scintillators. However, the ECAL consists of 4 mm thick scintillators with 2 mm thick lead absorbers and the HCAL uses 16 mm thick iron absorbers with 4 mm thick scintillators. Due to the absorber plates, crossing particles undergo bremsstrahlung and pair production, which creates light in the scintillator layers. This light is transmitted to photo-multipliers by wavelength shifting fibres.

The Scintillating Pad Detector (SPD) and the preshower detector (PS) are placed in front of the ECAL. They consist of layers of scintillators and serve for the identification of pions. Besides this they provide informations to the hardware trigger (L0).

Muon System (M1-M5)
Muon triggering and muon identification are fundamental requirements to the LHCb detector as muons occur in many final states of CP sensitive and rare decays. To stop muons, 80 cm thick layers of iron are staggered at the end of the detector in five stations M1-M5. In between, Multi Wire Proportional Chambers, filled with a gas mixture of Argon, carbon dioxide and CF_4, use the ionisation of the gas to detect the muons. An electric field accelerates the ions and electrons and the arising current is proportional to the energy of the muon. Only muons with a momentum greater than 6 GeV/c pass the whole detector. The muon system provides its information at the earliest level L0 and the high level HLT trigger.

3.2. The LHCb trigger system

The LHCb detector is designed for a low pile-up[1] to ensure good triggering and reconstruction with clean events. In contrast to the other three experiments at the LHC, the instantaneous luminosity at LHCb is reduced to $4 \cdot 10^{32}\,\mathrm{cm^{-2}\,s^{-1}}$. In order to run at two orders of magnitude below the LHC design value an active beam defocussing system at the interaction point is required, which allows to compensate also the partial beam loss with time[2]. This system enables to only partially overlap the two proton beams, which provides a constant luminosity within about 5% during a fill.

Nevertheless it is not possible to store all data. Hence a reduction of the data rate of 40 MHz to 12.5 kHz is required. A two stage trigger system (see Fig. 3.5) consisting of a hardware (L0) and a successive software trigger (HLT) was developed. The first stage trigger is fully synchronous with the 40 MHz bunch crossing rate of the LHC. In only 4 μs it has to make its decisions upon the informations of the calorimeters and muon chambers, and the corresponding transversal momenta to reduce the event rate to 1 MHz. In order to further reduce the event rate to 12.5 kHz the HLT trigger makes use of the whole data set and runs at two stages. The HLT1 aims for an reduction of a factor 30 by partially reconstructing the events chosen by the L0 trigger. With the already reduced data rate more time is available for this step. Afterwards the HLT2 trigger performs a full offline-like event selection. The final output rate is stored with 12.5 kHz and available to get processed and analysed.

---

[1]Average number of interactions per beam crossing.
[2]Lumininosity induced, impedance-induced losses (resistive wall effect) and electron-cloud bombardment.

LHCb 2015 Trigger Diagram

40 MHz bunch crossing rate

L0 Hardware Trigger : 1 MHz readout, high E_T/P_T signatures

450 kHz	400 kHz	150 kHz
$h^\pm$	$\mu/\mu\mu$	e/γ

Software High Level Trigger

Partial event reconstruction, select displaced tracks/vertices and dimuons

Buffer events to disk, perform online detector calibration and alignment

Full offline-like event selection, mixture of inclusive and exclusive triggers
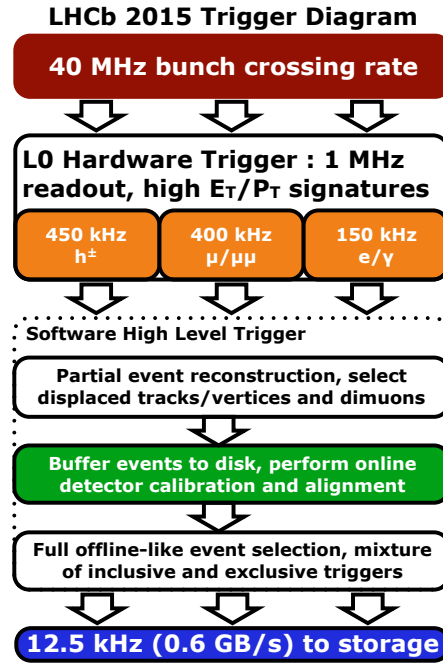
12.5 kHz (0.6 GB/s) to storage

Fig. 3.5.: LHCb trigger scheme in 2015. This first stage is implemented in hardware, while the following HLT software trigger uses the whole data set [21].

3.3. Data taking at LHCb

The LHCb Experiment has various advantages over the *B* factories with their e^-e^+ colliders. A higher cross-section, larger boost and the fact that the whole spectrum of *b* hadrons is produced, but also less attractive characteristics of the LHC environment like the increased background level, which comes along with hadronic collisions, result in a number of experimental compromises, such as the difficulty in reconstructing final states with neutral or missing particles or a reduced flavour tagging efficiency [22]. Despite these challenges the LHCb detector has collected the worlds largest sample of charm and beauty decays in Run I which enabled many key results establishing LHCb as the next generation flavour physics experiment [18].

Initially the LHCb experiment was meant to run at an instantaneous luminosity of $2 \cdot 10^{32}\,\text{cm}^{-2}\,\text{s}^{-1}$ corresponding to an average pileup of approx. 0.7, which are the two most important parameters for the detector operation. In 2011, the number of bunches in the LHC was increased to a maximum with a spacing of 50 ns. Hence, the pileup could be reduced while raising the instantaneous luminosity to twice the design value [18]. The protons collided with a centre-of-mass energy of 7 and 8 TeV in 2011 and 2012 (Run I) and at 13 TeV since 2015 (Run II). The trend of the recorded luminosity on LHCb over the years is shown in Fig. 3.6. In September 2017, LHCb crossed the threshold of 6 fb^{-1} recorded luminosity and therefore doubled the Run I integrated luminosity.

With the so collected data LHCb announced in July 2015 the observation of pentaquarks in the $\Lambda_b^0 \to J/\psi K^- p$ channel [24]. Pentaquarks are particles containing four quarks and one antiquark. The two states $P_c^+(4380)$ and $P_c^+(4450)$ show a combined significance of 15σ and the quark content of the so-called pentaquark-charmonium is $c\bar{c}uud$.
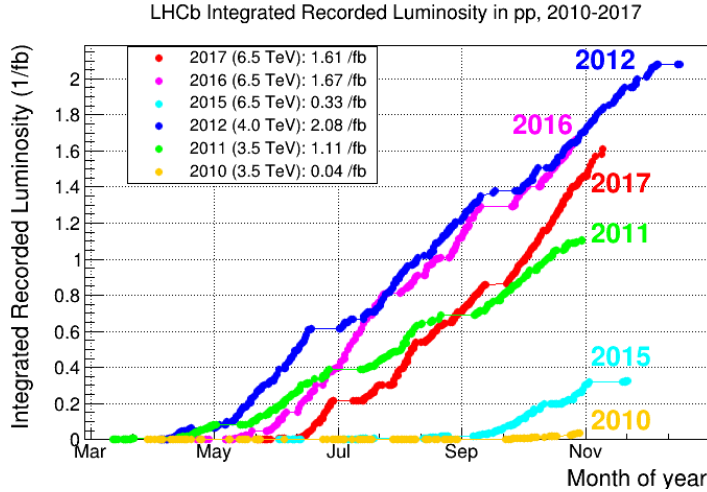
Fig. 3.6.: Recorded luminosity in LHCb from 2010 until 2017 [23].

The world's largest sample of exclusively reconstructed charm and beauty decays collected by LHCb enabled many key results in flavour physics. The measurement of the angle γ of the CKM triangle by the LHCb experiment already dominates the global average with the world's best precision [25]. Also in other measurements of flavour specific observables it is expected to reach the world best sensitivity after Run II, *e.g.* in the measurement of the CKM angle β [26].

Another great impact on the studies of New Physics effects made LHCb with the first evidence of the rare decay $B_s^0 \to \mu^+\mu^-$ [27] in 2013. This was followed by the observation of this decay and the first evidence for $B^0 \to \mu^+\mu^-$ in a combined analysis of LHCb and CMS data [28]. The decays $B_s^0 \to \mu^+\mu^-$ and $B^0 \to \mu^+\mu^-$ are highly suppressed in the Standard Model and can only occur via higher order topologies, so-called penguin diagrams due to missing direct flavour changing neutral currents. The results are compatible with the Standard Model. However, more data is necessary to enable high precision measurements of branching fractions, which could show possible deviations from the Standard Model. Furthermore, the even rarer decay $B^0 \to \mu^+\mu^-$ could be observed.

The data set is already increasing during Run II, as LHCb already doubled the Run I data set. However, an upgraded detector aims for a major increase of data by increasing the luminosity. Hence, LHCb will be able to lower the statistical and systematic uncertainties so that the sensitivity is increased substantially. Not only the decay $B^0 \to \mu^+\mu^-$ benefits from an upgraded detector and an enlarged data set. Also the charm-less decay $B_s^0 \to \phi\phi$ is forbidden at tree level. By the domination of penguin loop transitions it is highly sensitive to New Physics contributions. The time-dependent *CP* violation, which should be close to zero in the Standard Model, could show effects of New Physics [29]. A first measurement of the *CP* violating phase ϕ_s in $B_s^0 \to \phi\phi$ has already been published by LHCb. However, the statistical uncertainty of 0.12 rad, which can be achieved by the end of Run II in 2018 [30] can be further reduced to 0.026 rad with an enlarged data set of the upgraded LHCb detector. This uncertainty is close to the accuracy of the Standard Model prediction from theory [29].

3.4. The upgrade of the LHCb detector

The LHCb upgrade will enable the data collection of $5\,\text{fb}^{-1}$ integrated luminosity per year, which means a total of $50\,\text{fb}^{-1}$ integrated luminosity in 10 years. This is essential for reaching a higher sensitivity after Run I and Run II [29]. As already mentioned in the previous section, the instantaneous luminosity at LHCb is kept low by the so-called luminosity levelling. To reach the goal an increase of the instantaneous luminosity from $4 \cdot 10^{32}\,\text{cm}^{-2}\,\text{s}^{-1}$ to $2 \cdot 10^{33}\,\text{cm}^{-2}\,\text{s}^{-1}$ with an average pile up of about 5 is necessary [31]. As an increase of the instantaneous luminosity does not imply an increase of the amount of recorded data, an major upgrade of the trigger system is needed. The LHCb upgrade is foreseen for the Long Shutdown 2 of the LHC in 2019 and 2020. This upgrade affects multiple sub-detectors of LHCb, which will be explained in the following. An overview of the upgraded LHCb detector can be found in Fig. 3.7.
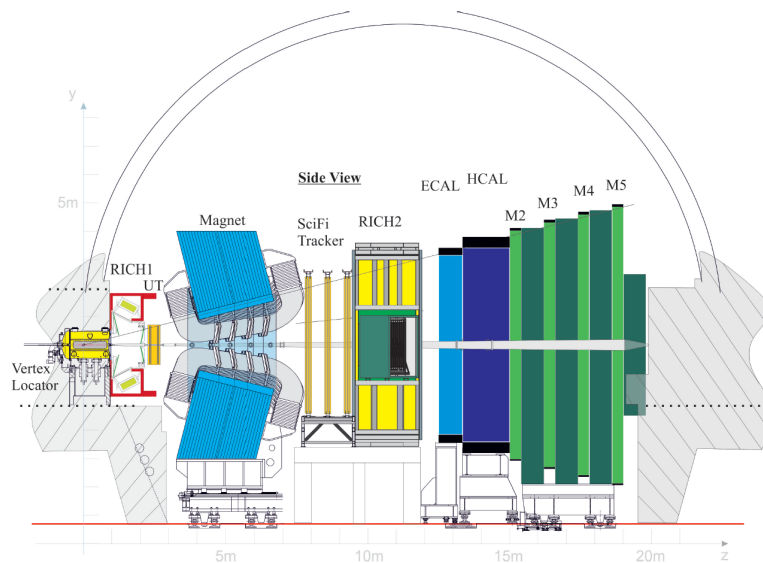

Fig. 3.7.: Schematic view of the upgraded LHCb detector [31]. The TT will be replaced by the Upstream Tracker UT and the SciFi Tracker will substitute the Tracking Stations T1, T2, T3. All other sub-detectors will also be modified.

LHCb Trigger Upgrade

The present L0 trigger is implemented in hardware. Trigger selections at this level are made with the 40 MHz beam crossing rate based on the deposited transverse momentum in the calorimeters and the muon stations. The performance of the L0 trigger varies according to the nature of the event. Decays with multiple muons in the final state the L0 efficiency is <90% with respect to offline selected events, as muons are not produced directly in the proton-proton collisions and therefore serve as powerful background discriminant. The same applies for decays with multiple electrons, but result in lower L0 efficiencies because of the greater background which impose tighter transverse energy requirements. Decays like $B_s^0 \to \phi\gamma$ require a high transverse energy photon in the offline analysis, which imposes the L0 efficiency to maintain at >90% [32]. For beauty decays with only one muon the L0 efficiency decreases to >70% [32], a fraction of which comes from triggering on hadronic decay products. Purely hadronic decays like for charm or

beauty meson decays lower the L0 efficiency to O(10%) and O(20%) [32], respectively. One reason for this is the worse energy resolution but largely because of much higher backgrounds which impose tighter transverse energy requirements to reduce the rate of triggered events to an acceptable level. This is already a substantial fraction of the *B* meson mass and any further increase would cut a substantial fraction of signal decays [29].

The L0 efficiency is strongly dependent on the instantaneous luminosity. Figure 3.8 shows the trigger yield as a function of the instantaneous luminosity. For channels involving muons the signal yield rises linearly, where the L0 is best able to discriminate between signal and background. For hadronic channels the signal yield saturates with increasing luminosity and limits the maximum instantaneous luminosity at which the detector can be usefully operated [29].
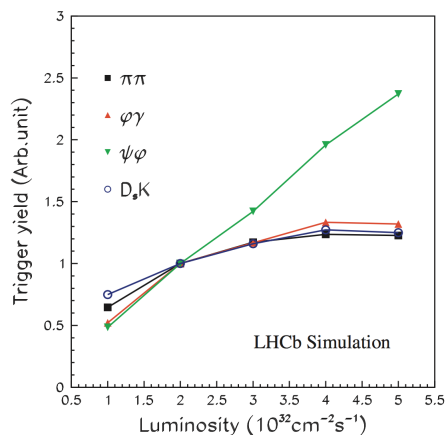
Fig. 3.8.: Efficiencies of the L0 trigger at a given luminosity for selected channels measured on simulated events [32].

Therefore a fully flexible software trigger running with the LHC clock at 40 MHz was proposed. It can use the full event information at each level of the trigger. This requires reading out the whole detector at 40 MHz and would increase the number of triggered hadronic decays up to a factor of seven [29]. Therefore, a complete replacement of the current FE electronics of all sub-detectors is mandatory.

Upgrade of Tracking detectors

Besides the replacement of the FE electronics, the higher event rate with more tracks per event demands higher granularities of all tracking detectors. The upgraded VELO will completely replace the current detector and have a similar module pattern. The new VELO detector will be a silicon detector based on hybrid pixel sensors. These 41 million square 55 μm pixels will have an integrated micro channel evaporative CO_2 cooling with a closest distance of 5.1 mm to the beam [33]. This geometry combines a new radiation hard readout electronics and a re-designed cooling system. The TT before the dipole magnet will be replaced by the Upstream Tracker (UT) for reason of radiation hardness and detector occupancy. While the geometry stays the same, the sensor granularity will be increased by using silicon micro-strips [31]. The Tracking Stations T1, T2 and T3 are

going to be replaced by the SciFi Tracker, a tracking detector based on a completely new technology. It is built from scintillating fibres with a silicon photomultiplier read out. This sub-detector is described in the following Chap. 4.

Upgrade of particle identification detectors

A change in the basic structure of the RICH detectors is not mandatory. As the HPDs have an enclosed readout electronics dedicated to the 1 MHz readout rate, all photon detectors need to be replaced. For this reason, multi-anode photomultiplier tubes with an external readout electronic come into operation. Furthermore, enhanced optics should enable an enlarged focal length and radius of the Cherenkov rings. This results in more addressed photo detectors, hence a better performance in face of a higher detector occupancy [34].

The first muon station M1, as well as the PS and SPD detector are going to be removed. The detectors gave input to the L0 trigger and are not needed anymore, due to the new trigger system. Also the FE electronics of the calorimeters will be replaced to suit the 40 MHz read out. Due to radiation damage it is considered to replace a few of the inner modules of the ECAL. The FE electronics of the muon chamber already fulfil a 40 MHz read out. Though, to decrease the detector occupancy, additional shielding around the beam pipe will be installed.

4. The Scintillating Fibre Tracker

Currently two different detector technologies are employed in the Tracking Stations T1-T3. Both detectors have demonstrated their excellent performances during Run I and Run II [20, 35, 36]. In the upgrade phase of the LHCb detector, a new technology will be installed - a detector made of scintillating fibres. This chapter describes the scintillating fibre tracker for the LHCb upgrade and depicts the requirements of the tracker upgrade. The information is mostly obtained from Ref. [31].

4.1. Requirements for a tracker upgrade

The tracking detectors upstream (UT) and downstream (SciFi Tracker) of the dipole magnet have to provide high precision momentum measurements for charged particles. With this information precise mass and lifetime resolutions of decaying particles can be determined. As described in the previous chapter the upgraded LHCb detector is planned to run with an increased instantaneous luminosity of $2 \cdot 10^{33}\,\mathrm{cm}^{-2}\,\mathrm{s}^{-1}$, $25\,\mathrm{ns}$ bunch crossing and an average number of proton-proton interactions per bunch crossing of about five. The current tracking system was designed to operate with an instantaneous luminosity of $2 \cdot 10^{32}\,\mathrm{cm}^{-2}\,\mathrm{s}^{-1}$ and assures that the occupancy in the hottest region is limited to 10%. However, improvements to the track reconstruction algorithms allowed data collection at an instantaneous luminosity of $5 \cdot 10^{32}\,\mathrm{cm}^{-2}\,\mathrm{s}^{-1}$ with an increased maximum occupancy of 25% and no loss in the track finding efficiency [31].

A high hit efficiency, good spatial resolution in the bending plane of the magnet and low material budget in the acceptance is highly required by the track reconstruction. Furthermore the LHCb upgrade demands to operate during the full lifetime of the upgraded LHCb detector and for the FE electronic to work at $40\,\mathrm{MHz}$. Summarized, the strongest requirements for an upgrade of the T-stations as listed in the LHCb Tracker Upgrade TDR [31] are:

- Hit detection efficiency as large as possible (about 99%) - the reconstructed noise cluster rate at any location of the detector has to be in addition well below (<10%) the signal rate at the same location.

- Spatial resolution below $100\,\mathrm{\mu m}$ in the bending plane of the magnet.

- Radiation length $X/X_0 \leq$1% per tracking layer to minimise multiple scattering and have that effect smaller than in the tracking system upstream of the magnet.

- FE electronics running with the LHC clock at $40\,\mathrm{MHz}$ - short recovery times should minimise inefficiencies due to dead-time.

- Operate with the required performance the full lifetime of the LHCb upgrade with an integrated luminosity of $50\,\mathrm{fb}^{-1}$.

Despite of that, it is shown in Ref. [29] that the detector occupancy of the OT becomes too high at higher luminosities. An operation at such luminosities would require either replacing some OT modules by shorter ones, or using a detector with higher granularity. Nevertheless, as mentioned previously, all read-out electronics of the IT and OT would need to be replaced to allow a triggerles read out of the complete LHCb events at 40 MHz. The evolution of this major tracking upgrade has gone through several stages. The Expression of Interest for an LHCb Upgrade [37] has been published in 2008, which describes the switch to an triggerless read out and a modification of the tracking stations. Different options for this have been described in the Letter of Intent for the LHCb Upgrade [29] and the LHCb Framework TDR [38]. First ideas of a fibre tracker for LHCb has been discussed and a possible implementation was to build a Central Tracker made of fibres. Another option was to extend the current IT in order to lower the occupancy of the OT. End of 2013 during the LHCb Upgrade SciFi Tracker: Technology Validation Review it was chosen to replace the tracking stations by a Scintillating Fibre Tracker (SciFi Tracker). This complete new detector technology will cover the full acceptance after the magnet.

Scintilliating fibres with a length of 2.4 m and a diameter of 250 µm will be the active material of this detector and will be stacked to fibre mats with 6 layers. These detector modules are going to be read out with Silicon Photomultipliers (SiPM). The overall conceptual design of the SciFi modules is similar to the one described in [39].

4.2. Layout of the LHCb SciFi Tracker

The SciFi Tracker will be located between the LHCb magnet and RICH2 and the space is constrained by the one currently used by the IT and OT. The SciFi Tracker will have as well three stations (T1, T2, T3) which are composed of four detection layers with a *x-u-v-x* geometry like shown in Fig. 4.1. Each detection layer will have a rectangular stepped hole in the centre to incorporate the beam pipe structure. The detection layers
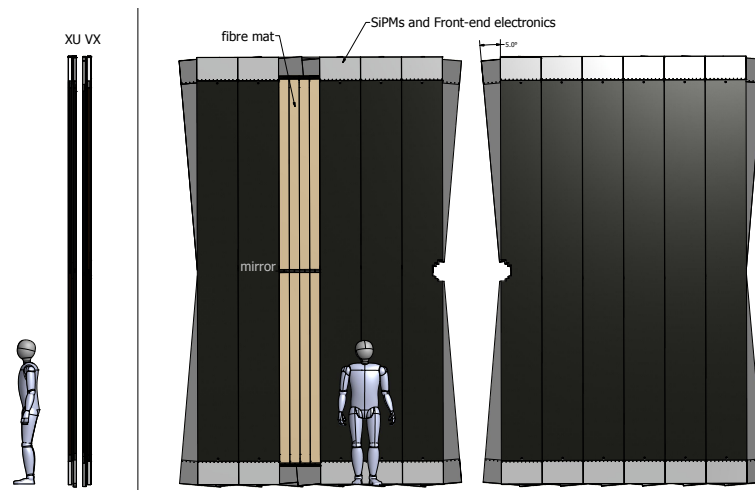

Fig. 4.1.: Schematic view of one station of the SciFi Tracker [31].

are separated into 10 to 12 modules per layer, which host the active material consisting of eight fibre mats.

The LHCb SciFi Tracker group has performed an extensive and comprehensive programme of research and development (R&D) to verify that this new detector technology is suitable for the conditions present after the LHCb upgrade. Even though the serial production of this detector has already started, there are still studies being performed to optimise the readout electronics, cluster finding algorithms, simulation of the detector, test beam campaigns, *etc.*. The preparation and execution of the serial production of the SciFi detector modules is of main importance in the LHCb SciFi Tracker group. Therefore several quality assurance procedures have been developed to ensure good quality of the detector modules.

In this context, studies performed during the serial production as well as R&D related studies on scintillating fibres and fibre mats play an important role and were carried out in the context of this thesis. The serial production of detector modules for the SciFi Tracker is being described in Chap. 5. Studies on single scintillating fibres and irradiation of these are presented in Chap. 6 and the quality assurance during the serial production discussed in Chap. 7.

4.2.1. Operating mode

The scintillation photons are guided through the fibres and their detection is realised by multichannel Silicon Photomultipliers (SiPM). These multichannel SiPMs are arrays of individual channels which are equivalent to a single SiPM. With an SiPM channel width of 250 μm, identical to the fibre diameter, the photon detection in a channel can be assigned to a spatial coordinate [31]. The read out of the SiPMs is based on a custom designed ASIC chip which integrates the signal over 25 ns.

As a typical particle hit results in photon detection in more than one channel, noise is getting reduced by applying thresholds in the electronics and forming clusters in neighboured channels, see Fig. 4.2. The actual hit position is furthermore calculated as the weighted mean over all channels inside this cluster. The most important characteristics of the SciFi Tracker are the hit detection efficiency and spatial resolution, which are dominated by the overall light yield of the photon detectors. The spatial resolution is provided by the width of SiPM channels and therefore nominal $^{250\,\mu m}/\sqrt{12} = 72\,\mu m$. However, the spatial resolution depends also on manufacturing tolerances of the fibre mats and modules. Providing a high signal to noise ratio is necessary to achieve the highest possible hit detection efficiency. In addition with the clustering procedure, a spatial resolution substantially better than 100 μm can be realized [31].

However, the hit efficiency depends on the number of photons reaching the fibre end and getting detected. Thus, a mirror is placed at one side of the fibre mat, so that photons emitted in the opposite direction of the SiPM have the chance to get detected as well.

Scintillating fibres

For the SciFi Tracker scintillating fibres with a round cross section of the type SCSF-78MJ from the company Kuraray [40] are used. They have been chosen for their fast decay constant of 2.8 ns and their high light yield. These multicladded blue emitting plastic fibres with a core based on polystyrene and two claddings with descending refractive indices enable light guiding along the fibre axis via total reflection. More details and studies on these single fibres can be found in Chap. 6. As stated before the fibres are
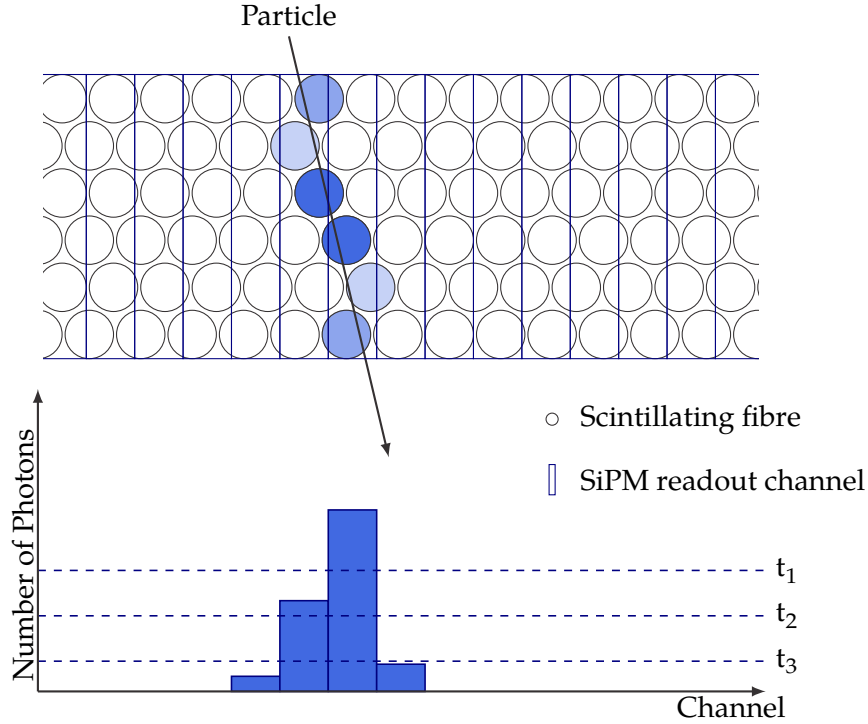
Fig. 4.2.: SciFi clustering procedure. A crossing particle typically creates photons in more than one channel. The signal gets discriminated by three different thresholds (t_1, t_2, t_3). Channels which exceed the seed threshold t_2 are selected. If the sum of neighbouring channels above the neighbour threshold t_3 is higher than the sum threshold t_1 these channels are forming a cluster. The actual hit position is calculated as the weighted mean of all channels inside this cluster.

mirrored at the height of the beam pipe, to increase the light yield at the SiPM side. This extends the maximum photon travel time inside the fibre. With an effective travel time of $6\,\mathrm{ns\,m^{-1}}$, the average time for a photon to traverse $5\,\mathrm{m}$ is $30\,\mathrm{ns}$.

The fibre transparency and therefore the light guiding procedure is decreased by the radiation environment in the LHCb cavern. In Fig. 4.3, the integrated ionising dose after an integrated luminosity of $50\,\mathrm{fb^{-1}}$ is displayed. It peaks close to the beam pipe at $35\,\mathrm{kGy}$ [31] for T1 and decreases steeper than exponential to the lower and upper edge of the detector acceptance. From results seen in irradiation measurements performed by the LHCb SciFi group, the total expected loss of signal near the beam pipe is expected to be about 35% [41]. The typical light yield of an unirradiated SciFi module at the mirror is about 16-20 photoelectrons (p.e.). The best performing modules will be selected to be placed in the central region of the SciFi tracker, where the dose is the highest. Nevertheless after 10 years of operation in the most irradiated region at the mirror, a light yield of about 12 photoelectrons is expected. For this reason six layers of fibres have been chosen to be the best solution of having a high light yield without exploiting the material budget. More details on radiation damage of scintillating fibres are further described in Chap. 6.
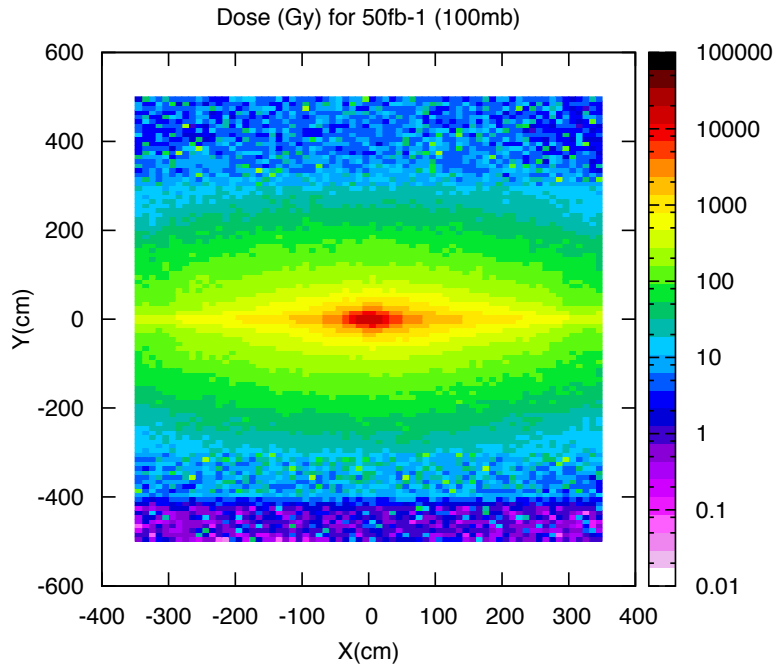
X(cm)

Dose (Gy) for 50fb-1 (100mb)

Fig. 4.3.: Expected dose distribution in Gy at the position of T1 after an integrated luminosity of $50\,\text{fb}^{-1}$ [31].

Silicon Photomultipliers

Silicon Photomultipliers by Hamamatsu[1] are chosen to be used in the SciFi Tracker. SiPMs are solid state photon detection devices with a high ability to detect single photons. With its small size and high granularity, the features are most suitable for a high resolution fibre tracker such as the SciFi tracker.

SiPMs are composed of Avalanche Photodiodes (APD), operating in Geiger-mode. A photo-diode is a semiconductor diode which can generate an electrical current by incident light at a p-n junction by means of the photoelectric effect. An incoming photon creates an electron-hole pair and the charge carriers are drifting into oppositely charged zones. However, these can only be separated if the energy of the photon corresponds to the distance between the conduction and valence bands. If a reverse voltage above the breakdown voltage is applied, the photo-electron is accelerated and thus can separate further charge carriers resulting in an avalanche. Operating in Geiger-mode the avalanche can be stopped via a quench resistor, which is serially connected to the diode. The induced current causes a voltage drop at the resistor which results in a voltage drop of the diode below its breakdown voltage. It is possible to reach gains of 10^5 to 10^7 with the applied over voltage such that the signal current is independent of the number of incoming photons [42].

One pixel of the SiPM matches with a photo-diode in Geiger-mode. These pixels are arranged in matrices representing a SiPM channel. With such a geometry, it is possible to determine the amount of light as the number of fired pixels is proportional to the

---

[1]Hamamatsu Photonics K.K., 325-6, Sunayama-cho, Naka-ku, Hamamatsu City, Shizuoka Pref., 430-8587, Japan

number of photons and a single photon sensitivity is reached. The disposed SiPM arrays (Fig. 4.4) have 128 channels with a pitch of 250 µm and the height of a 6 layer fibre mat with 1.625 mm. Each channel contains 104 pixels with a size of 57.5×62.5 µm^2 [43].
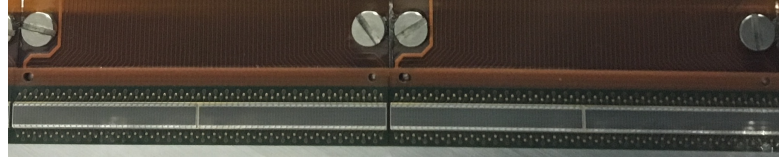

Fig. 4.4.: Photograph of two 512-channel SiPM consisiting of two dyes with 128 channel each, conntected to a flex cable.

The noise of the SiPMs can be distinguished between three sources: thermal noise, pixel cross-talk and after pulsing. Thermal noise creates random avalanches and therefore the same signal as a single entering photon. The rate of such random avalanches or dark noise is strongly correlated to the irradiation of the devices. As shown in Fig. 4.3, the integrated ionising dose in the SiPMs ($y=\pm250$ cm) will be 40 Gy after 50 fb^{-1}. The rise in the dark noise is the only radiation damage observed. But the dark noise can be reduced by lowering the temperature. Therefore the SiPMs will be operated at −40 °C. Each firing pixel can also induce an avalanche in a neighbouring pixel, the so-called pixel cross-talk. After pulsing is a certain probability that a firing pixel can, after some time, fire again. The average noise rate per channel is expressed as Dark Count Rate (DCR). As stated before this noise will be reduced by applying thresholds in the electronics and forming clusters of firing SiPM channels, see Fig. 4.2.

The photon detection efficiency (PDE) is a key parameter for the photo-detector, as it directly influences the light yield of the fibre module, which has to be maximised. It is defined as the number of detected photons divided by the number of incoming photons. This number combines two effects: the quantum efficiency, which is the probability that an incident photon produces a charge carrier (electron or hole) capable of triggering an avalanche in the depletion region and the geometric efficiency, which incorporates dead zones, where no active material causes inefficiencies. The emission spectrum of the SCSF-78MJ scintillating fibre is well suited before and after irradiation for the chosen SiPM photon-detectors from Hamamatsu as their spectral PDE between 450-500 nm matches the fibre emission spectrum, see Fig. 4.5.

Electronics

The specific electronics for the LHCb SciFi Tracker are separated in front end and back end. As the front end electronics are directly situated at the detector as part of the module, the back end electronics will be placed outside the LHCb cavern in the counting house. The FE boards interface on the one side directly to the SiPMs and to the experiments data-acquisition and control system on the other side. The FE electronics provide a digitisation of the SiPM signals and perform the clustering. On the back end side these data are processed.

As shown in Fig. 4.6 on the FE board a custom designed ASIC called the low-Power ASIC for the sCIntillating FIbres traCker (PACIFIC) is situated along with an FPGA (Field Programmable Gate Array) responsible for the clustering algorithm. The signal of each SiPM is amplified, shaped and integrated over the 25 ns LHC bunch crossing rate in the PACIFIC chip. Afterwards a fast clustering algorithm is executed on the FPGA to reduce
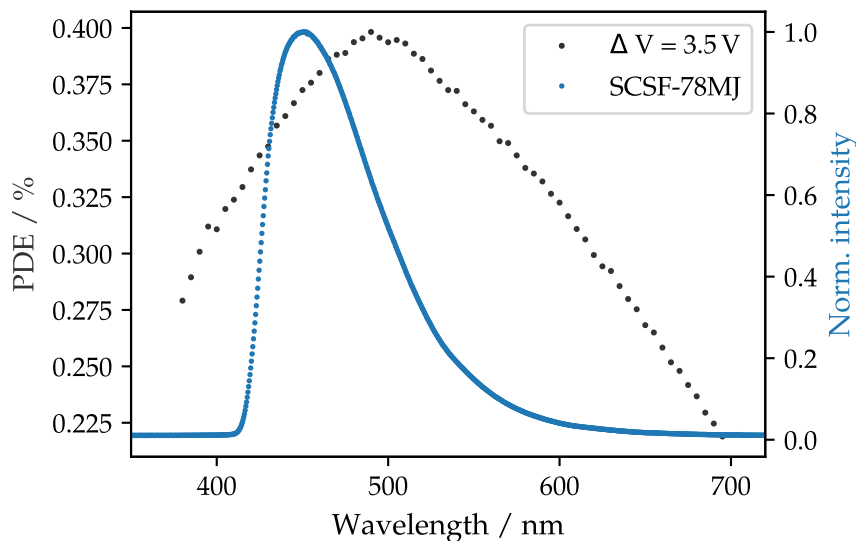
Fig. 4.5.: Average PDE of a Hamamatsu SiPM at ΔV=3.5 V. The emission spectra of the SCSF-78MJ Kuraray fibre is overlaid. The data of the PDE are taken from [43].

the data volume. These formed clusters are transferred to the back end electronics by a GBT (GigaBit Transceiver), subsequently. Each PACIFIC is assigned to one SiPM dye (64
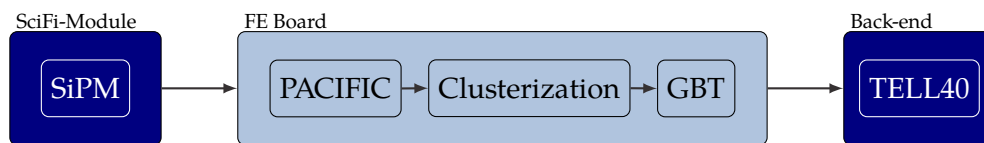

Fig. 4.6.: Scheme of readout electronics. The signal of one SiPM gets digitised, shaped and integrated via the PACIFIC ASIC. Afterwards clusters are formed via a fast algorithm on Field Programmable Gate Arrays and transferred to the back end electronics with a GigaBit Transceiver.

channels) and will have the same granularity. It uses two interleaved gated integrators to avoid dead time. Hence, the goal is to process all photons of a particle hit, but the output is also dependent on the arrival time of the photon inside the SiPM. As already mentioned before, the maximum travel time for a photon inside the scintillating fibre can be 30 ns, therefore photons can also arrive outside the 25 ns integration window and will be assigned to the next bunch crossing [31].

To distinguish signal from noise a fast clustering algorithm is executed on FPGAs. It also serves as zero suppression and hence reduces the required bandwidth after the ASIC. The typical signal created by a particle crossing a fibre mat is dispersed over several fibres and therefore a few SiPM channels, see Fig. 4.2. The mean position of this cluster is the best estimate of the hit position. The cluster algorithm provides three different thresholds. Each signal exceeding the *seed threshold* (e.g. 2.5 p.e.[2]) is directly accepted. In addition one neighbouring channel on the left and on the right is accepted if their signal is above the *neighbour threshold* (e.g. 1.5 p.e.). The cluster is finally accepted if the total signal height inside the cluster exceeds the *sum threshold* (e.g. 4.5 p.e.) [43].

---

[2]It is very unlikely that noise could reach that signal height.

4.2.2. Detector modules

The module geometry technology has been chosen such that the requirements addressed in Sec. 4.1 can be achieved. Single scintillating fibres with a diameter of 250 μm are glued to a matrix with 6 layers to produce a sufficient signal amplitude and hit resolution. Low occupancy is provided by the small spacing of the fibre matrix and the narrow SiPM channels. A support structure composed of a carbon fibre, honeycomb sandwich structure ensures a light and stable detector. With cooled photo-detectors noise and false clusters are being reduced.

A SciFi Tracker module consists of 2×4 fibre mats. Hence, four mats are arranged next to each other while two are sitting one upon the other. At the height of the beam pipe the fibre mats have a mirrored end, to increase the light yield on the other side, where the photo-detectors are located. The SiPMs are situated in a so-called Read Out Box, where their cooling is realised and the FE electronics is housed. A typical SciFi module is 5 m tall with a width of 0.52 m.

Fibre Mats

The main components of the SciFi Tracker are scintillating fibres arranged in six-layer fibre mats (see Fig. 4.7). A length of a fibre mat is about 2.4 m with a width of about 13.5 cm. To ensure a spatial resolution below 100 μm the positioning of the single scintillating fibres need to be precisely parallel. The fibre pitch within a layer is defined to be higher than their diameter to ensure a reliable fibre positioning during the production of fibre mats and to account for possible deviations from the nominal fibre diameter. For this reason the fibres are wound on a threaded wheel with a pitch of 275 μm. The fibre is wound on the wheel with controlled and monitored tension to allow for a reliable positioning without harming the fibre. The fibre of the first layer is guided by the grooves in the wheel and fixed and cut at the end. Glue is applied on top to bound the different layers together. The fibre on the successive layers are guided by the layers below and are therefore shifted by half the horizontal pitch with respect to the lower layer. After curing of the glue the fibre mat can be cut perpendicular to the fibre direction and taken off the wheel to be flattened.

Fig. 4.7.: Cross section of a fibre mat.

Special shaped holes inside the winding wheel get filled with glue during the winding of the first layer, see Fig. 4.8. These pin holes are positioned along the wheel surface and follow the pitch of the fibres. They lead to the forming of so called alignment pins on one side of the mat, which can then be used to align the whole mat with respect to the fibre direction. The implementation of this into a serial production is explained in more detail in Chap. 5.

The fibre mat itself is a very fragile object and therefore needs an additional protection for handling and shipping. Thus, the fibre mats are getting laminated from both sides with a 25 μm kapton foil. This foil is wider than the fibre mat width and has slots for the
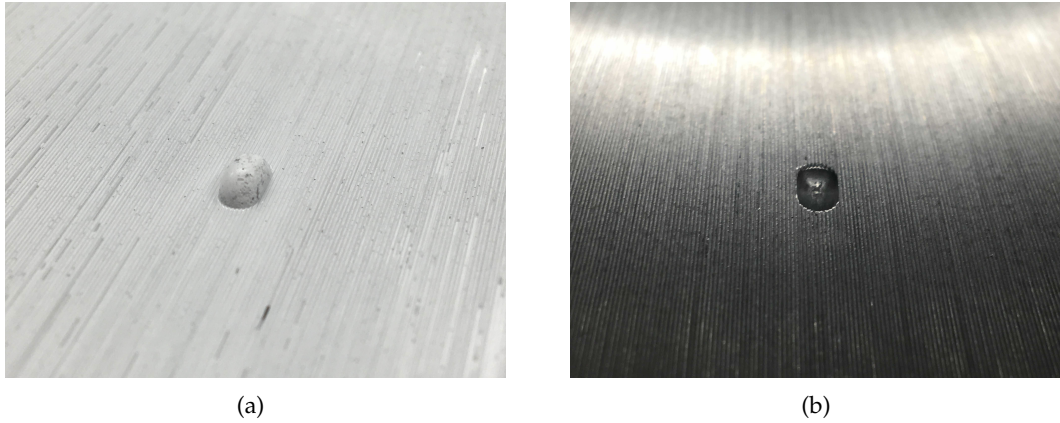
(a)   (b)

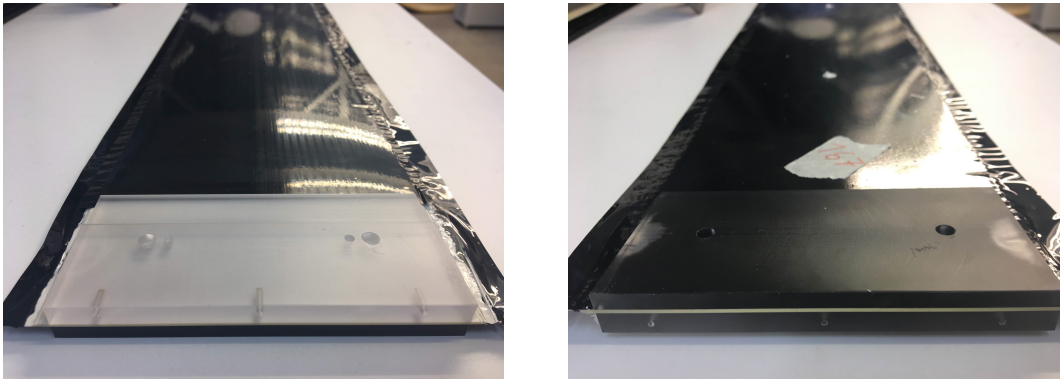Fig. 4.8.: (a) Pin shape on a fibre mat and (b) pin hole in the winding wheel.

Fig. 4.9.: Laminated fibre mat with end pieces from both sides.

pins. As a result the fibre mat surface and also the edges are protected. Small plastic end pieces are glued to both ends of the fibre mat (Fig. 4.9). They serve as a support structure for the SiPM mounting and the mirror glueing. Supported by the end pieces, the fibre mat can be cut to the correct length and get the needed optical quality. Afterwards the mirror is attached to one end, for which a aluminized Mylar foil is used with which reflectivities of up to 80% [31] were reached. Also the fibre mats need to be cut to the correct width. This cut needs to be precisely parallel to the fibres to not scratch fibres by accident inside the SiPM acceptance. To reach this accurate rotating saw blades are used. More details on the fibre mat production and the realisation in a serial production can be found in Chap. 5. Furthermore, quality assurance procedures are described in Chap. 7.

Support structure

The material of the panels has been chosen to provide good stiffness while having a low material budget to limit the number of multiple scattering. To ensure a high resolution and reliable tracking the module needs to have a solid positioning and to be stable in time. First, the fibres inside the module have to be positioned reliably. The position of the SiPMs will be aligned with precision holes inside the SiPM end piece on the fibre mat. In addition a slight misalignment can be corrected in software.

A sandwich structure of honeycomb and carbon fibre will produce a robust and also light tight tracking module, see Fig. 4.10. The rigidity of the carbon fibre reinforced polymer (CFRP) layer will give the requested rigidity to the light honeycomb structure. The fibre mats will be centred between two of such half-panels [44]. In addition on each end of the 5 m panels the honeycomb is replaced by so-called end plugs made of aluminium. They serve as a connection to the read out box and the so called C-frames, which are described in the next sub-section, and are placed outside of the LHCb acceptance. The material budget of a single SciFi module and their fraction of the respective radiation length is listed in Tab. 4.1.
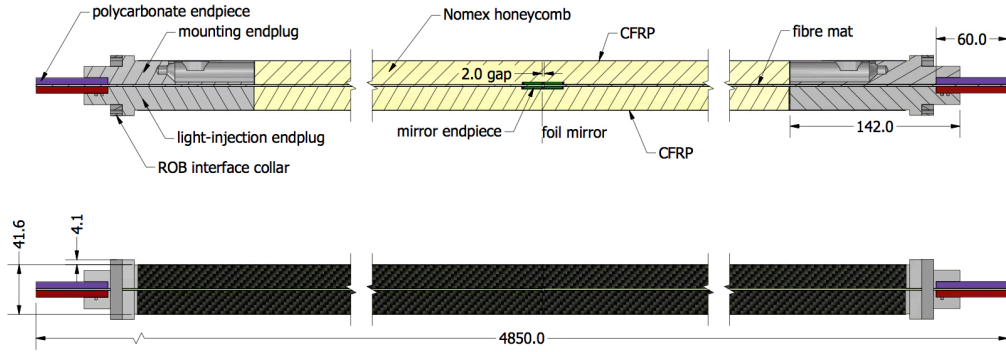
Fig. 4.10.: Cross section of a SciFi Tracker module. The fibre mat is centred between a honeycomb [44].

Tab. 4.1.: Material budget for a single SciFi module. Data taken from [44, 45].

Material	Thickness / µm	Layers	X_0 / cm	X/X_0 / %
Nomex Core	20 000	2	1310	0.305
CF skin	200	2	23.3	0.172
Panel glue	75	4	36.1	0.083
Fibre mat	1350	1	33.2	0.407
Lamination foil	25	2	28.6	0.053
Total	42 100			1.02

The full SciFi Tracker is divided into 12 detector planes. Each plane consists of 10-12 modules of which two modules are modified to fit around the beam pipe, with a rectangular shape cut out [46]. For a full detector module, eight fibre mats have to be precisely positioned between the two half-panels. For this purpose, a full size (5 m×0.53 m) template was machined from a single plate of aluminium at a very high precision. With this, a precise alignment of the fibre mats inside the module and the reproducibility is guaranteed. As stated before, the fibre mats come along with alignment pins on one side. The template has the corresponding groove so that the fibre alignment from the winding is transferred to the final detector module and the C-frame.

Read out Box

At each end of the module the fibre mats need to be connected to SiPMs. As motivated in the SiPM section the photo detectors need to be cooled to −40 °C to reduce the dark

count rate. Furthermore these SiPMs are connected to the FE electronics via flex cables. This small volume with plenty of interfaces at the end of the detector module is called Read-Out-Box (ROB), see Fig. 4.11(a). There are several requirements that the ROB has to fulfil: light tightness with a proper thermal insulation and being moisture isolated, having the interior cold enough while the outer surface needs to stay above the dew point to prevent condensation and frost build-up on the inner part (Fig. 4.11(b)) [31]. Based on these requirements the ROB consists of two parts: the cold box, which houses the SiPMs with their cooling bars and is flushed with Nitrogen, and the warm volume of the ROB, which holds the FE electronics.

(a) (b)
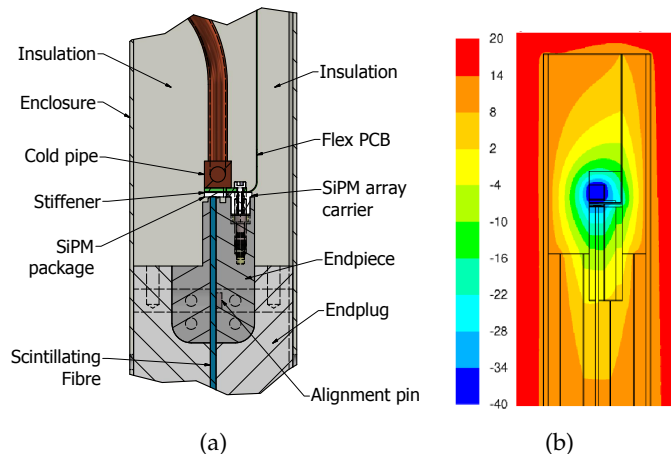
Fig. 4.11.: (a) Schematic view of the cross section of the cold volume of the Read Out Box. It is situated at both ends of a SciFi detector module, the FE electronics are sitting above and are separated by insulation material. (b) Thermal simulation of the Read Out Box. While the SiPMs are getting cooled to −40 °C, the FE electronics and also the SciFi module stay warm [31].

The SiPM arrays are being cooled with the help of a pipe, which holds a liquid cooling agent and gets pressed against their back by springs. To prevent mechanical stress due to thermal expansion of the material, the cooling pipe design is split in segments which are connected via bellows. With this approach it can be ensured that the temperature gradient along one SiPM dye stays below 1 K [31]. This is an important criterion as the temperature of the SiPM directly influences the over voltage and therefore parameters like gain and pixel cross-talk. As cooling liquid Novec™-649 was chosen [31], as it is more environment friendly than the C_6F_{14} which is widely used at the LHC.

Infrastructure

The single SciFi detector modules will be carried by so-called C-frames. Each C-frame will hold two detector layers, so that the whole detector will be carried by 6×2 C-frames. The mechanical infrastructure is mounted on rails, so that it is possible to move the detector halves away from the beam pipe, *e.g.* for maintenance. The C-Frames need to provide all the mechanical and electrical infrastructure necessary to operate the SciFi detector, this includes *e.g.* Novec™ and water cooling, as well as trays for the FE electronics cables and the SiPM biases and the Nitrogen system, see Fig. 4.12.
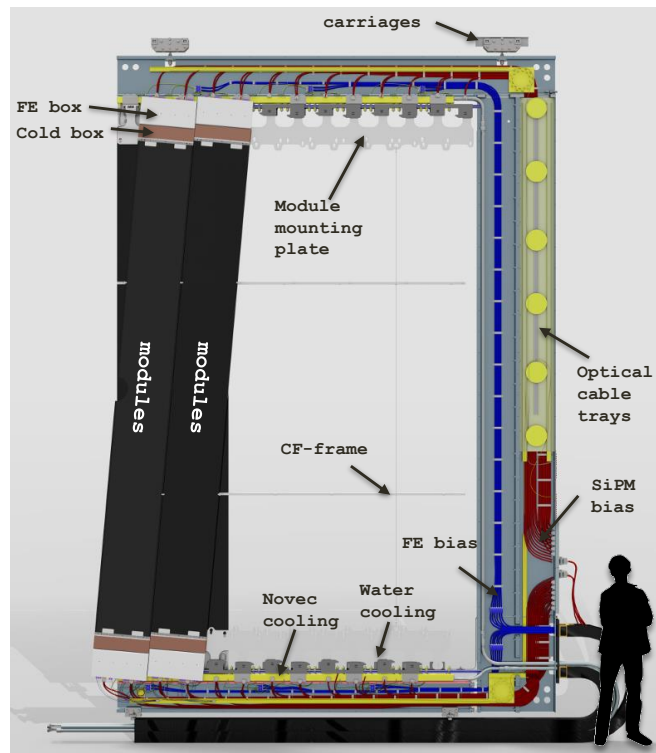
Fig. 4.12.: Twelve of such C-Frame halves will be installed to carry the SciFi tracker modules and to equip the SciFi Tracker with all needed infrastructure to operate [47].

4.3. Performance studies of SciFi Tracker prototypes

To determine the performance of the tracking detector with respect to the requirements, measurements in laboratories or within test beam campaigns are performed. For dedicated measurements, which cannot be realised in a laboratory environment, simulations are done.

Test Beam Campaigns

Amongst others, in May and November 2015 two test beam campaigns at the SPS at CERN were performed to test fibre mats for their light yield, attenuation length, single hit efficiency and position resolution. With the results a *Test Beam Report* [48] was composed, from which the following results are taken.

The detectors under test were single scintillating fibre mats, which have been mounted on the same support structures as the SciFi module design. The six-layer fibre mat matches the design, which was chosen to go to serial production. In addition an eight-layer fibre mat with an increased fibre pitch has been tested. Both fibre mats have been wound at TU Dortmund with a prototype of the serial production winding machine (see Chap. 5). The final read out electronics (PACIFIC) had not been available at that time, so that the SiPMs got read out with SPIROC electronics. Three thresholds are part of the 2-bit non-linear PACIFIC signal digitisation for the final SciFi Tracker electronics. With the available SPIROC electronics, it was possible to simulate this threshold digitisation in the collected data and calculate the cluster barycentre as the PACIFIC would allow for.

To determine spatial resolution and single hit efficiency, telescopes are used. They are placed before and/or after the detector under test, to define where a particle crossed the experimental setup. In these test beam campaigns, an AMS silicon ladder telescope [49] and/or the VELO TimePix telescope [50] were used, to define reconstructed particle tracks with a resolution much better than the fibre modules. In addition a scintillating fibre telescope [51] was developed based on the same technology as the LHCb SciFi Tracker.

Figure 4.13 shows the collected charge distribution at three different positions along the fibre module. There are multiple effects to the width of this distribution *e.g.* fluctuations of the path length of a crossing particle through the fibre core or lost photons along the fibre length. At the mirror position, the mean light yield was determined to be 16.31 ± 0.38 p.e.. This is the same position at which produced fibre mats during the serial production are getting tested for their light yield (see Chap. 5 and Chap. 7). As the hit position is calculated with the mean over the channels in a cluster, the spatial resolution gets better with increased light yield. The measured spatial resolution at the mirror position is (74.07 ± 0.58) µm for a charge weighting and (78.78 ± 0.61) µm for a PACIFIC-like weighting.

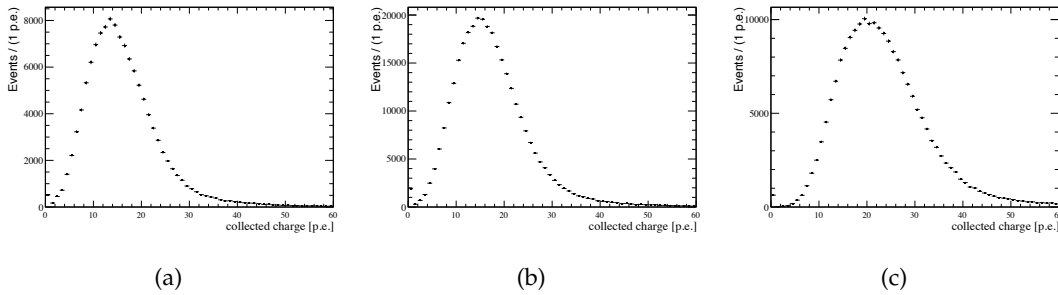| (a) | (b) | (c) |

Fig. 4.13.: Collected charge distributions for three different positions along the fibre module: (a) at the mirror, (b) at the centre of the module, (c) 50 cm from the SiPM [48].

The hit efficiency is be determined by counting the particle tracks passing through the detector under test and creating a cluster. An external telescope is then used as reference to look for matching tracks in the fibre module. The fluctuation of number of photons detected cause an efficiency below 100% as these events stay below the thresholds. As shown in Fig. 4.14, the single hit efficiency for the standard LHCb threshold (2.5 p.e. seed) is 98.75 ± 0.05% at the mirror position.

More details on these studies and results can be found in the corresponding technical note [48].

Simulation of the LHCb SciFi Tracker

To evaluate the performance and also the robustness of the SciFi Tracker, simulations are essential. Different studies on all components (fibres, SiPMs, electronics, cooling) in specialised smaller simulations are done by the LHCb SciFi group. But also effective models are used to simulate the SciFi Tracker as a whole detector, *e.g.* for tracking performance studies. In addition, it is mandatory to predict the performance of the SciFi Tracker over its whole lifetime and being affected by irradiation.
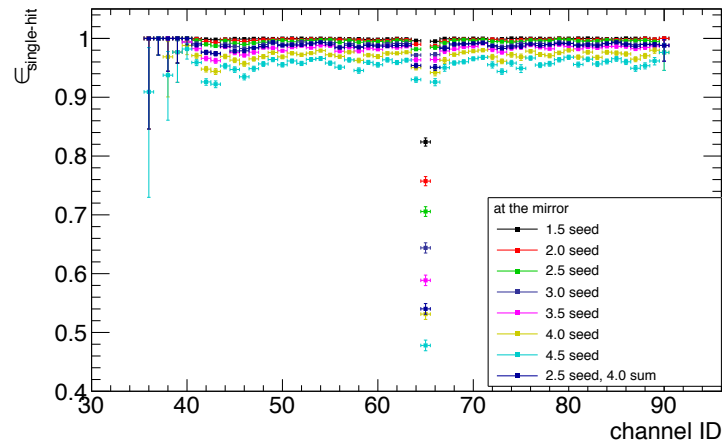
Fig. 4.14.: Single hit efficiency at the mirror position along the SiPM array and different seed thresholds (in p.e.) for the clustering algorithm. The dip around channel 65 corresponds to the gap between the two SiPM dyes [48].

4.4. Schedule for the SciFi Tracker

The LHCb SciFi Tracker is currently in the production phase. The production started beginning of 2016 with the first delivery of fibres. Shortly afterwards, the serial production of the fibre mats started in April 2016 in combination with the module production. More details on the serial production of the SciFi Tracker can be found in Chap. 5. In Tab. 4.2, the main milestones for the LHCb SciFi Tracker project, like *Engineering Design Reviews* (EDR), *Production Readiness Reviews* (PRR) and the production ranges, are listed.

Tab. 4.2.: Milestones for the production and installation of the LHCb SciFi Tracker [52].

Component	Start	End
Modules		
EDR		Q3 2015
Fibre delivery	Q1 2016	Q1 2018
PRR Fibre Mats	Q2 2016	Q2 2017
Fibre Mat Production	Q2 2016	Q1 2018
PRR Modules		Q2 2016
Module Production	Q2 2016	Q2 2018
SiPMs		
EDR		Q3 2016
Delivery	Q3 2016	Q4 2017
100% tested		Q2 2018
Cold Box & ROB		
EDR		Q3 2016
Production & integration	Q4 2016	Q4 2018
Loaded ROB fully tested		Q4 2018
Electronics		
EDR		Q2 2016
PRR PACIFIC		Q3 2017
First PACIFIC chips available		Q2 2018
PRR boards		Q3 2017
Board production	Q3 2017	Q4 2018
Frames		
EDR		Q1 2018
Assembly zone available		Q3 2017
Frame production	Q2 2018	Q2 2019
Installation		
Module installation	Q2 2018	Q2 2019
IT & OT removal		Q2 2019
SciFi installation	Q3 2019	Q3 2020

5. Serial production for the SciFi Tracker

The LHCb SciFi Tracker consists of three stations each containing four detector layers arranged in the *x-u-v-x* geometry. One detector layer will be equipped with 10-12 modules. As one module is carrying 8 fibre mats, about 1200 fibre mats have to be produced in total. The serial production of these fibre mats needs to ensure a fast and reliable processing of the fragile scintillating fibres to achieve the requirements presented in Sec. 4.1. The following chapter describes how the serial production of the detector modules, especially of the scintillating fibre mats, is organised and what steps are needed to build such a detector module. The complete serial production is a major project to which contributions were made during the course of this thesis.

5.1. Tasks & workflow

The serial production of the fibre mats started in April 2016 shortly followed by the production of the modules in July 2016. Fibre mats and modules are being produced in specialised Winding and Module Centres. The delivery of the fibres from the manufacturer is done via CERN, where also the testing of the fibre is carried out, detailed in Sec. 5.2.1. The task sharing is sketched in Fig. 5.1 and further described in the following section. Fibre mats are wound, finalized and characterised in the Winding Centre before getting shipped to the Module Centre. There, the longitudinal side cuts are performed and then the mats are assembled to a full size detector module, apart from the ROB and electronics. There are four winding centres (TU Dortmund, RWTH Aachen, EPFL
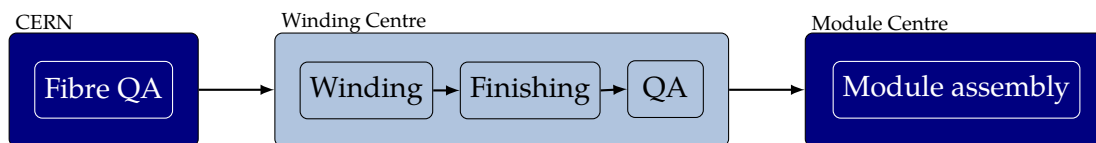

Fig. 5.1.: Task sharing between fibre mat winding centres and module assembly centres. The testing of the single scintillating fibres is done centrally at CERN.

in Lausanne and Kurchatov Institute in Moscow) and two Module Centres (University Heidelberg and NIKHEF in Amsterdam). To guarantee that the same procedures and the same tooling is used in every centre, an common *Engineering Design Review Report* [44] contains all nessecary information. In addition quality assurance procedures along with a scheme to assess the performance and geometry of a fibre mat were developed. Further information on the quality assurance for the fibre mat production is given in Chap. 7.

5.2. Production of fibre mats

The necessary steps to produce a fibre mat are listed in Fig. 5.2 and are further described in the following section. Quality assurance is applied throughout the whole production process, to identify possible defects as fast as possible. In addition, quality criteria have

Fig. 5.2.: Necessary steps to produce a fibre mat. These steps are done in the Winding Centres, before the fibre mats get shipped to the Module Centres, where the side cuts are performed before assembling the detector module.

been developed to allow a comparison between different mats, especially between mats from different Winding Centres. During this thesis, dedicated studies on the quality of produced fibre mats have been made as well as several quality procedures have been developed and implemented in the running serial production, which are shown in Chap. 7 along with the grade assignment scheme.

5.2.1. Fibre quality

Driven by the main requirements on the SciFi Tracker (Sec. 4.1) specifications for the scintillating fibres have been composed, which can be found in Ref. [53]. Beside requirements on the scintillation material, which needs to assure a short decay time, high intrinsic light yield per absorbed energy and low specific density and nuclear charge number, the scintillating fibre needs to fulfil different geometric specifications *e.g.* the statistical diameter variation shall not exceed 3.3 μm. An important property of such fibres is the attenuation length which shall exceed 350 cm, prior to irradiation. More than 10 000 km of fibres are delivered to CERN from May 2016 to January 2018. The delivery was done periodically in batches of 100 km and 300 km. Before distributing the fibre spools, with 12.5 km scintillating fibres each, to the Winding Centres they have to be carefully tested. Hereby, attenuation length, light yield, resistance to X-ray irradiation and the diameter profile are measured. To measure the diameter of the scintillating fibre in a sufficient

way a machine has been developed and positioned at CERN [54]. In order to make the winding process as smoothly as possible, the single fibres get freed of bumps, either by shrinking them with a hot cone or, if they exceed a diameter of 350 µm, by cutting them and reinforce the scintillating fibre ends [55].

5.2.2. Fibre mat winding

To produce fibre mats from those scintillating fibres a threaded wheel with a diameter of around 82 cm is used. A machine has been developed for the serial production based on a prototype in Dortmund [56]. This serial winding machine is shown in Fig. 5.3. To ensure high quality and all safety features during operation an external company has been charged with the construction of such a machine[1]. Based on the experience in Dortmund and Aachen, this machine has been developed in close cooperation between the institutes and the company, where contribution have been made in the scope of this thesis. The threaded winding wheel is made from aluminium and has a pitch of
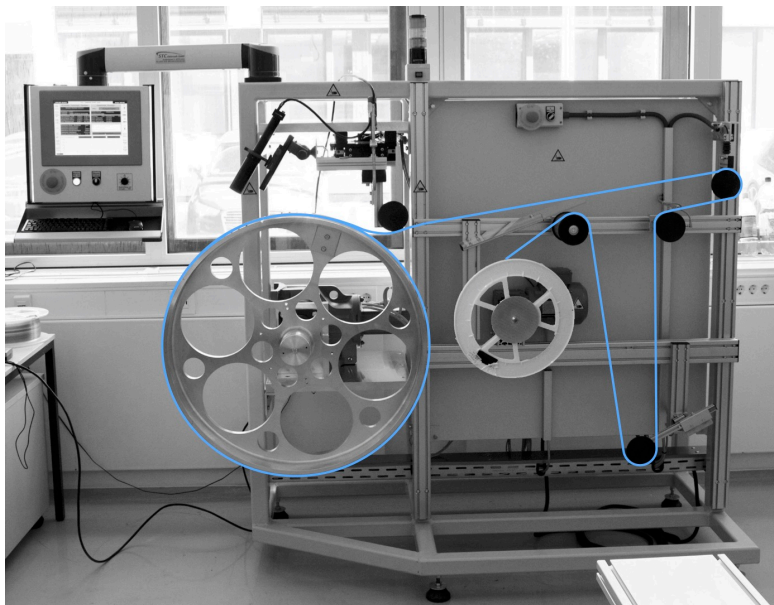
Fig. 5.3.: Serial production winding machine. The path of the scintillating fibre is indicated in blue.

275 µm. The main function of the winding machine is to place the scintillating fibres on the turning winding wheel, which positions the fibres of the first layer. A feeding spool provides the tested scintillating fibre and with the help of several smaller spools the fibre gets guided to the winding wheel. The tension on the fibre is controlled by a dancer roller arrangement. This corresponding force is fixed to be 50 cN, as the resulting tension enables a reliable fibre winding while not damaging the fibre and is measured by a load cell. In addition the position of the dancer roller arrangement is used to control the speed of the feeding spool delivering the fibre. The correct position of the fibre across the width of the winding wheel is controlled by a linear slide carrying a small guiding spool. This linear slide is moving during the winding procedure such that it corresponds to the pitch of the winding wheel. The machine was designed in

---

[1]STC Elektronic GmbH, Krellenhäuser 3, 07973 Greiz, `http://www.stc-forum.com`

a well-thought-out way, *e.g.* the scintillating fibre can be easily placed on the guiding spools and also the exchange of a winding wheel can be done simply and within a few minutes. The corresponding software part provides adaptability, *e.g.* different modes for different steps during the production are foreseen but also parameters can be changed, like the speed of the winding wheel or the absolute position of the last guiding spool with respect to the thread on the wheel.

The positioning of the scintillating fibres of the first layer is provided by the grooves in the threaded winding wheel. The scintillating fibre is fixed to one side of the winding wheel with a screw and during the first turns of the wheel, its speed is low to ensure a good positioning. A thin layer of TiO_2 loaded epoxy directly applied on the winding wheel serves as a thin protection layer. The winding wheel has pin holes along its circumference with a distance of around 245 mm, which are following the direction of the fibres. These holes are also filled with glue during the winding of the first layer. The pins have rectangular edges parallel to the fibres and sloping ones in the direction of the fibres. After the glue is cured, they stick to the fibre mats and serve as alignment pins during the module production, see Sec. 5.3. At the end of winding a layer, the scintillating fibre is again fixed to the winding wheel with the help of a screw and epoxy is applied on top. The thin and homogeneous film should not affect the fibre positioning. For the following layer, fibres from the layer below serve as guidance such that each successive layer is shifted by half the horizontal pitch with respect to the previous layer. After finishing six layers of winding, an additional layer of glue is applied on top. In order to give the fibre mat an additional protection it is laminated from both sides with a thin 25 μm Kapton foil. The first lamination foil is applied directly after the winding to protect the mat surface.

After finishing the winding and glueing the first lamination foil, the glue needs to cure. The whole curing procedure takes 36 hours, while for the first 12 hours the wheel should slowly rotate to prevent a build-up of glue drops. After the curing time, the fibre mat can be taken off the wheel to be flatten. To do so, the mat is cut perpendicular to the fibres at a dedicated spot along the circumference. Due to the tension during the winding, the mat directly shrinks about 1 cm. This behaviour leads to the pins design, such that the shrinking pulls the pins off the hole instead of shearing them off. After the mat is taken off, a cleaning of the wheel is mandatory to free the grooves of remaining glue and dust and to prepare the wheel for the next winding.

5.2.3. Finishing of fibre mats

After winding the mat has to go through several steps to get finished before it is send to the Module Centre, see also Fig. 5.2.

Tempering & 2nd Lamination

In the early phase of the serial production, a bending of the fibre mat transversal to the fibre direction has been observed. This potential bending of up to a few mm brings along difficulties during the module production, especially if the bending is larger than the height of the alignment pins. To reduce this effect, the fibre mat is heated up to 40 °C for 8 hours with a flat aluminium jig, which is floated with water. This so-called tempering procedure ensures to have a flat mat in the end. After the tempering, the fibre mat get its second lamination foil on the pin side. For this, the foil has dedicated slightly oversized holes for the pins.

End Piece Glueing

A sensitive step during the finishing of the fibre mats is the glueing of the so-called end pieces. These are small plastic pieces, which hold the fibre mat in between, serving as a support during the optical cut and holding the SiPMs or the mirror respectively. The mirror and the SiPM end pieces are glued with respect to each other on both sides of the fibre mat and therefore define the fibre mat length. The nominal fibre mat length is $2424.0 \, ^{+0.5}_{-0.0}$ mm [44]. To account for possible length variations due to the temperature, a high precision end piece glueing jig is flushed by water, to hold the fibre mat at the reference temperature. An additional observation which has been made during the early phase of the serial production was the shrinking of the fibre mat after cutting it off the wheel. In addition to the instant shrinking of the fibre mat, a longer lasting shrinking component has been noticed. Dedicated studies have been performed, which are also a part of this thesis (see Sec. 7.2). It has been agreed to wait at least four weeks after the unforming of the fibre mat, to ensure, that the mat does not shrink anymore and therefore the end pieces stay at the same distance to each other.

Furthermore the end piece glueing is a delicate step as the amount of glue used and the pressure with which the end pieces are pressed onto the fibre mat highly influence the mat geometry and therefore its quality, see Chap. 7. With the help of a torque wrench and additional support in the middle of the mat width it is guaranted that the fibre mat stays straight in between the end pieces. This technique prevents too much glue below the end pieces, but the excessing glue needs to be removed, as the sharp edges of the end pieces are needed during the module production.

Optical Cut

After the fibre mats are equipped by end pieces, they are cut transversal to their final length. For this purpose, a precise diamond milling on both fibre mat ends is done. This provides a smooth flat surface against which at the one side the SiPM window is pressed, so that the majority of light can be detected. On the other side, a mirror is applied to reflect photons and guiding them to the SiPM end. For the cutting procedure the fibre mat is aligned with respect to its end pieces. After a pre-cut using a saw blade, which cuts away the excess length, the optical cut is performed using a diamond head. Hereby a slow advance speed of 25 mm/ min with a drive of 800 rpm^2 is applied.

Mirror Glueing

A sufficient light yield at the SiPM side is achieved by glueing a mirror at the opposite fibre mat end. For this purpose a small gluing jig has been constructed, which presses the mirror against the mirror end piece until the glue is harden. With the help of Kapton tape and the same epoxy glue used for the winding with a shorter curing time, the aluminized Mylar mirror foil is glued to the whole width and height of the end piece.

5.3. Module production

The Winding Centres ship their produced mats to the Module Centres, where they are used to build full-size SciFi Tracker modules. Before the fibre mats can be used for the module production, a longitudinal cut to the correct width is needed. This is done in the Module Centres to protect the fragile edges of the fibre mats during the transport to

---

^{2}Revolutions per minute.

the Module Centres. With a precision of more than 150 µm, this cut is done by means of two parallel circular saws. This way a minimal loss of acceptance at the boundary of two neighbouring fibre mats can be assured.

The module assembly is done with the help of a high precision full size template, which is machined from a single aluminium plate. Corresponding grooves in the template to the pins on the fibre mat assure a precise alignment with an intrinsically guaranteed reproducibility (see Fig. 5.4(a)). After the template is prepared (cleaning and applying

(a)

(b)
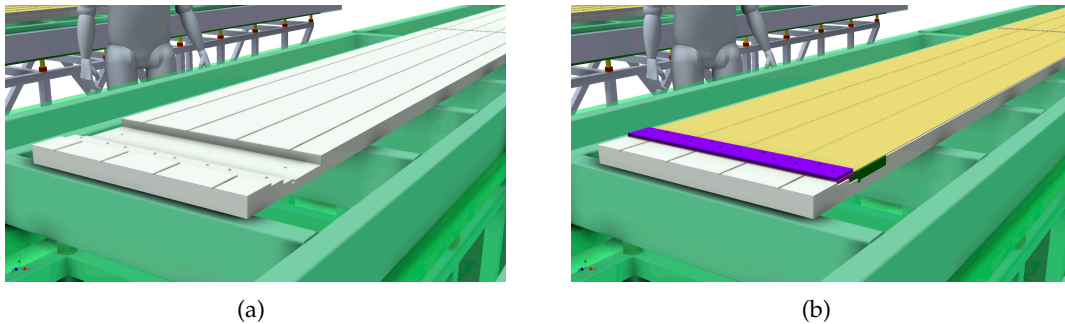
Fig. 5.4.: (a) High precision aluminium template for the module assembly. Grooves along its length provide as alignment of the fibre mats by means of their pins. (b) 8 fibre mats placed in the module template and ready to get the first half-panel glued. [57]

anti-stick agent), a dry assembly of the module is foreseen. This is done to ensure that all components for the given module are correct and *e.g.* no geometrical anomalies interfere the assembly process. However, the end plugs (including the light injection system) and eight fibre mats are placed precisely in the template as shown in Fig. 5.4(b). In a next step glue is applied on the surface of the fibre mats and the end plugs. The thin layer of glue on the end plugs will bond to the carbon fibre skins of the half-panel, where the honeycomb is cut out, while the glue on the fibre mats will form a bond with every honeycomb cell. A construction of a frame with vaccum foil and a vaccum pump removes the air and therefore apply pressure. Under this conditions, the glue will cure for eight hours. Afterwards, the bonded half module needs to be unformed from the template and to be turned over onto a flat aluminium template to glue the second half-panel in a similar way. The only difference is that the honeycomb has to be cut out carefully where the fibre mat pins are sitting. To finish the module, it needs to cleaned and the sidewalls closed to provide light-tightness. At this stage, before getting connected to the ROB box, the fibre mat ends still stick to the outside and are exposed to light, see Fig. 5.5.
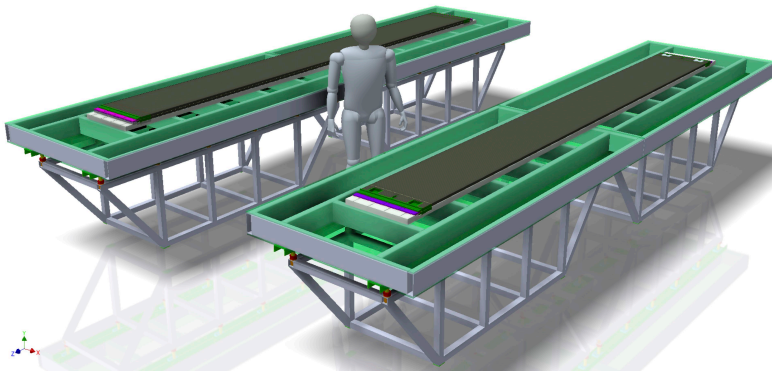
Fig. 5.5.: Two fully assembled modules on the module assembly table [57]. The fibre ends (pink) are still sticking out until the ROB box is connected.

6. Scintillating fibre studies

This chapter describes the general principle of scintillating fibres with their light production and light guidance. Studies on the light guidance and radiation effects are necessary to verify the viability of this detector technology under the LHCb upgrade conditions. Within the scope of this thesis several studies have been performed on single scintillating fibres. To perform measurements on these very fragile fibres an automated setup has been developed to guarantee a reliable and reproducible measurement. This thesis shows measurements on the attenuation of the light travelling along the fibre. This attenuation can be dependent on different effects *e.g.* on the exit angle of the photon or other environmental influences. In addition an irradiation study has been carried out to measure the radiation damage over time.

First of all, an overview over scintillating fibres is given including their properties and functionality. Afterwards, the *xy*-table setup is being introduced and analysis methods are decribed. Furthermore, light guidance studies are presented, where amongst other things the effects of water and heat to scintillating fibres were analysed. At the end of the chapter, the performed in situ irradiation study in the LHCb cavern is presented.

6.1. Overview

As mentioned previously, for the LHCb SciFi Tracker, scintillating fibres with a round cross-section and a diameter of 250 µm are used. These fibres are of the SCSF-78MJ type from Kuraray [40] and consist of a core and two claddings (see Fig. 6.1). The claddings account for about 12% of the total diameter. The scintillation light of the fibres is created in the core. As the core is optically denser than the cladding, a total reflection is possible at the interfaces and the light can be transported to the ends of the fibre. According to Snell's law of refraction the following relation holds for the maximum angle Θ_T of the total reflection:

$$\sin \Theta_T = \frac{n_{\text{cladding}}}{n_{\text{core}}}. \tag{6.1}$$

The fibre core consists mostly of polystyrene, and two additional dopants are added to ensure a sufficient scintillation [58]. The inner cladding is made from polymethacrylate and the outer cladding from fluorinated polymer. The properties of these materials are listed in Tab. 6.1.

Tab. 6.1.: Materials of the scintillating fibre and their properties [40].

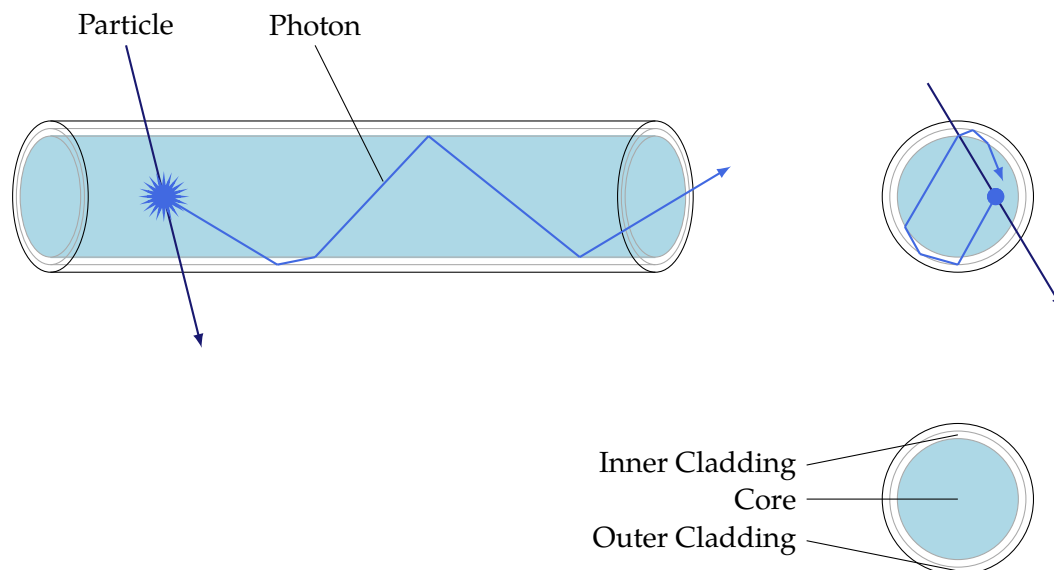|	Material	Refractive index	Density / $\frac{\text{g}}{\text{cm}^3}$
Core	Polystyrene	1.59	1.05
Inner cladding	Polymethacrylate	1.49	1.19
Outer cladding	Fluorinated polymer	1.42	1.43

Fig. 6.1.: Scheme of a multi-cladded scintillating fibre. Photons (blue line) which are created by a traversing particle, are guided to the fibre end by total reflection.

Scintillation Mechanism

If an ionising particle crosses a plastic scintillator, some of its energy is absorbed and, as a result, scintillation light emitted [59]. On a molecular basis, organic scintillators contain one or more benzene rings. For this the conjugated double bonds of the unsaturated carbon atoms in a benzene ring are particularly important. Electrons of these aromatics are not bound to any particular atom and form therefore molecular π orbitals. Prior to excitation, they are located in the singlet ground state. If an ionizing particle traverses the fibre core, these π-electrons may get excited once or multiple times. However, these excitations are a combination of electronic and vibratory excitations. This state decays non radiatively, via vibrational phonons, with a lifetime of 1 to 8 ns, depending on the scintillator, in the lowest electronically excited state [59]. Normally, this state would decay to vibrational sub-levels by emission of photons. However, in case of pure polystyrene, this process is slightly delayed so that the base material is usually mixed with a small amount of a second substance (around 1 %) [60, 61]. This is excited by the primary scintillation and then decays much faster into the ground state. The resulting scintillation light has a too low wavelength to be reabsorbed. Possible, but strongly suppressed, triplet excitations decay much slower and thus add a delayed component to the scintillation light.

Due to the fact that the emission spectrum of the base polystyrene and the absorption spectrum of the dopant have a good overlap and the concentration is high enough, which means shorter distances between the molecules can be realised, the energy can be transferred via radiation-less dipole-dipole interactions, the so-called Förster transfer [62]. For these scintillating fibres p-Terphenyl is used as first dopant. However, concentrations necessary to provide an efficient energy transfer include a too high self-absorption wherefore a second dopant is used. This second dopant absorbs the scintillation light of the first dopant and emits in the transparent region of polystyrene. It acts as wavelength

shifter as the lower concentrations do not enable a direct energy transfer. In this case tetraphenyl-butadiene (TPB) serves as wavelength shifter and furthermore adapts the wavelength to the sensitivity of the SiPM [31].
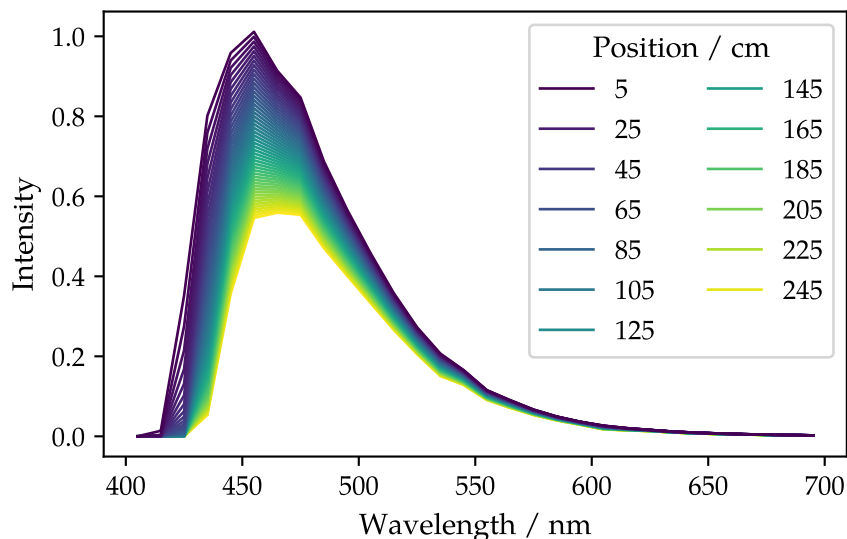

Fig. 6.2.: Spectrum of a scintillating fibre for different distances to the detector. In the range from 5 to 245 cm the distances were varied in 5 cm steps from blue to yellow. The spectrum was measured with help of a Hamamatsu Mini-spectrometer[1].

The spectrum of a scintillating fibre is shown in Fig. 6.2 for different distances of the excitation position with respect to the detector. From the closest measured distance (blue) until the largest (yellow), measurements at equidistant steps were performed. The maximum of the emitting light is around 450 nm whereas the maximum shifts to larger wavelengths with increasing distance to the spectrometer. The self-absorption of the wavelength shifter causes a higher absorption at lower wavelengths.

Light Guidance

As stated previously Fig. 6.2 shows the spectrum of the scintillating fibre for different distances of the excitation location from the detector. The most significant effect is that the intensity decreases with increasing distance to the detector. This holds especially for the short wavelength range, so that the intensity maximum shifts with increasing distance to longer wavelengths. Since there are various losses during the light guidance, *e.g.* by absorption or Rayleigh scattering, an exponential decrease of the light intensity I_0 along the travelling distance x is observed:

$$I(x) = I_0 \cdot \exp\left(-a_0 x\right), \tag{6.2}$$

where a_0 describes the attenuation factor and I_0 the intensity of the created scintillation light.

The wavelength dependent attenuation coefficient is shown in Fig. 6.3. Photons travelling through the fibre can get lost for various reasons. This photon loss affects the light guidance in the scintillating fibre and can be divided in two groups: absorption and

---

[1]Hamamatsu Mini-spectromenter TM Series - C10082CA/C10083CA series.

scattering, including losses at the boundaries. However, for polystyrene the absorption below 450 nm is dominated by electronic transitions and above by Rayleigh scattering. In addition the second dopant causes that wavelength shifted photons below 450 nm are re-absorbed. The attenuation factors described in Fig. 6.3, are due to the chemical
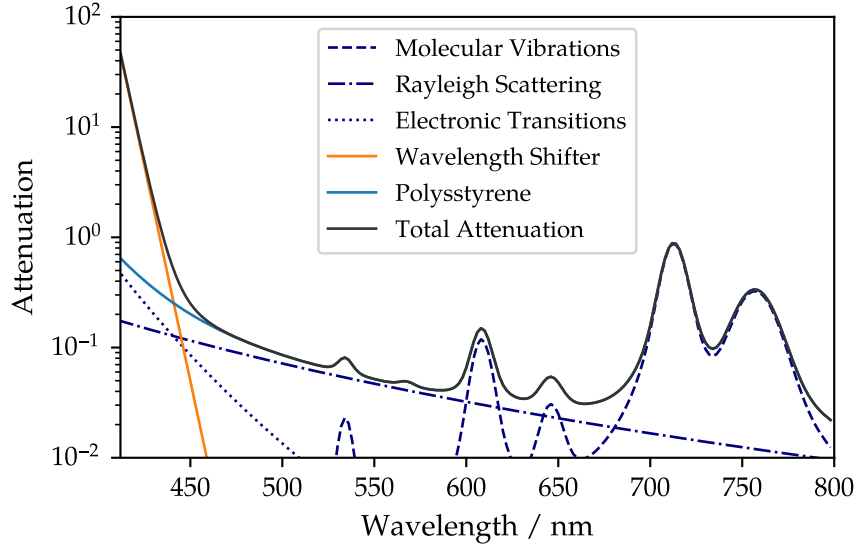
Fig. 6.3.: Relevant attenuation coefficients for the scintillating fibre. The attenuation in pure polystyrene is affected by Rayleigh scattering, molecular vibrations and electronic transition. For the scintillating fibres, the re-absorption of the wavelength shifter for shorter wavelengths needs to taken into account. Data taken from Ref. [63].

composition of the scintillating fibres. Additive attenuation can be caused by imperfect fibres as the photons can be scattered at dust particles or due to fluctuations of the core diameter. But also absorption due to foreign matter, like water, causes additional attenuation of the scintillating light. All of these sources for attenuation are strongly dependent on the path length and behave additive. Only the loss of photons at the boundaries (core-cladding and cladding-cladding) does not scale with the path length. Here, the number of reflections is important.

The wavelength shifter emits light isotropically, but only photons, that have the corresponding angle defined in Eq. (6.1) are guided along the fibre axis. The photons can take different paths along the fibre axis. In contrast to photons emitted from the fibre axis, photons emitted skew with respect to the fibre axis follow a helix path. For these photons, the trapping efficiency increases as light emitted perpendicular to this plane is excepted within a polar angle of $\leq 90°$. These photons are travelling through the fibre on helical trajectories and are reflected multiple times. Due to the higher number of reflections and the greater path length through the fibre, they are attenuated more. The path length L for a photon is given by

$$L = \frac{x}{\cos \theta} ,$$

(6.3)

where x represents the length of the fibre, which has been travelled through and θ is the angle of the photon inside the fibre with respect to the fibre axis. The relation between θ and the photon exit angle θ_{exit} is given by Snell's law:

$$\theta = \arcsin\left(\frac{n_{\text{air}}}{n_{\text{core}} \cdot \sin\theta_{\text{exit}}}\right). \tag{6.4}$$

The number of reflections N can be determined according to [64]

$$N = \frac{x \cdot \tan\theta}{2\sqrt{R^2 - r_{\text{min}}^2}}, \tag{6.5}$$

where r_{min} is the closest distance of a photon to the fibre axis.

Different studies of the attenuation in fibres have been performed in the scope of this thesis, *e.g.* the effect of water absorbed in fibres as well as the angular dependency of the attenuation length. These studies are detailed in Sec. 6.3.

Radiation Damage

In addition to the intrinsic attenuation, the fibre transparency and therefore the light guidance is reduced by irradiation. As previously mentioned, the dose close to the beam pipe peaks at 35 kGy for T1 and decreases steeper than exponentially to the lower and upper edge of the detector acceptance (see Fig. 4.3 on page 23). The main cause for the degradation of the scintillating fibres is an optical change of the base material leading to a transmission loss. Free radicals, like Benzyl, cyclohexadienyl and possibly other related, form absorption and scattering centres, which result in an increasing attenuation [65]. Radiation damage results in a reduction of the attenuation length so that the viability of the fibre under radiation is strongly dependent on its length. In addition, the basic scintillation process could be harmed by the radiation environment, though it is not expected for the used scintillating fibre and the LHCb upgrade environment [31].

Forming and annealing of radicals is strongly dependent on the environment. As the availability of oxygen influences the radiation damage by forming absorption centres during annealing [66], the irradiation effects may differ between high dose rate and low dose rate irradiations. At high dose rate irradiations oxygen is consumed faster as it could propagate into the fibre, while at low dose irradiations oxygen is continuously available [67]. In addition, the type of particle used for the irradiation may influence the annealing of absorption centres.

As the understanding of the irradiation damage for scintillating fibres is still incomplete, multiple irradiation campaigns have been performed by the LHCb SciFi group, in different conditions but using the same fibre type. Also in the scope of this thesis an in-situ irradiation in the LHCb cavern has been performed, see Sec. 6.4. The results of the irradiation campaigns are presented in Fig. 6.4. High dose rate irradiations were performed mainly at beam lines, like the CERN PS. To test if the radiation damage is also dependent on the dose rate, low dose irradiations like an in situ irradiation (see Ref. [56]) have been performed. To have the wavelength dependent additional attenuation due to the irradiation, these measurements were performed with a spectrometer. More information on these campaigns can be found in [31] and [56]. With the help of these measurements radiation damage models can be developed. Another approach is to simulate different irradiation damage models and compare them with the measurements. A single fibre simulation has been developed in a thesis written in the Dortmund SciFi
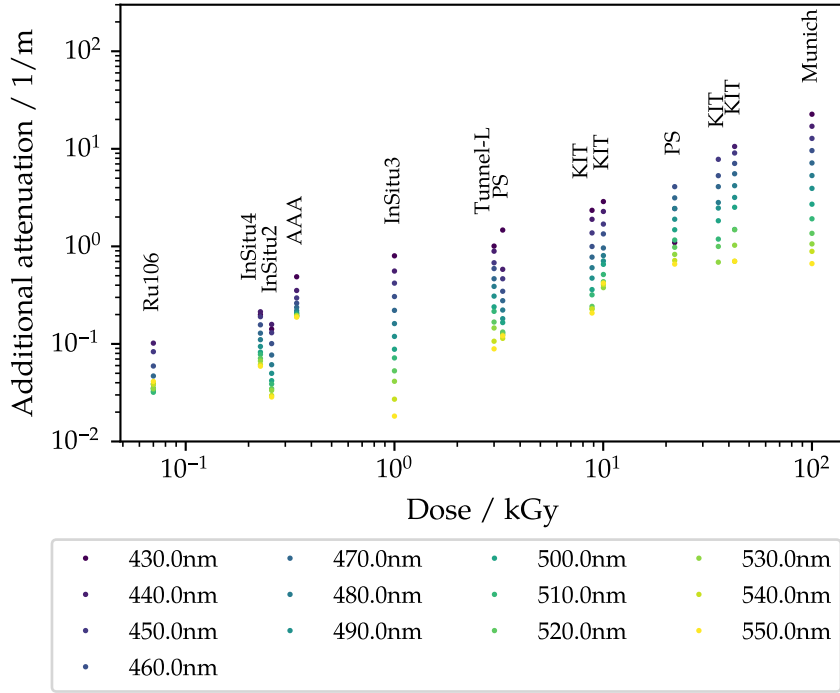
Fig. 6.4.: Irradiation campaigns done by the LHCb SciFi group. Additional attenuation for different wavelengths as a function of the applied dose. Data taken from [31, 56].

group [63]. Different radiation damage models and the comparison between these irradiation campaigns are presented in [56]. It can be assumed that the radiation induced attenuation just adds up to the intrinsic induced attenuation:

$$I(x) = I_0 \cdot \exp\left(-(a_0 + D \cdot a_D)x\right), \tag{6.6}$$

where a_0 represents the intrinsic induced attenuation factor, a_D the radiation induced attenuation and D the dose. Two different radiation models have been examined in Ref. [56], which describe in which way the dose influence the radiation induced attenuation:

$$a_{D,\mathrm{pow}} \cdot D = 0.4 \cdot D^{0.8}, \tag{6.7}$$

$$a_{D,\mathrm{lin}} \cdot D = 0.38 \cdot D, \tag{6.8}$$

where the attenuation a_D is given in $\mathrm{m}^{-1}\,\mathrm{kGy}^{-1}$ and the dose D in kGy. The power-law model described all given data points the best. Assuming that the reduced relative damage for large doses is caused by the higher dose rate, a linear model has been developed to describe low dose rate data and have a good description for the real detector operation.

Mechanical Properties

All the previous describes properties like the light yield and the light guidance with their attenuation are of major importance for the performance of the LHCb SciFi Tracker. But also mechanical parameters need to be studied, which influence the production of the fibre mats. There are two properties which have the most impact on the fibre mat

production. First, the variation of the fibre diameter influences the fibre positioning during the fibre mat winding. The production of the scintillating fibre itself is a delicate process as a drawing speed ensures the diameter of the out coming fibre via a real time measurement of the actual fibre diameter. The nominal diameter of the fibre is 250 μm, but due to the regulation process fluctuations are possible [31]. However, these fluctuations are small and within 1 μm. In addition larger variations more than 400 μm [44] have been observed. With a fibre pitch of 275 μm during the fibre mat winding, it is clear that such thick spots, which are just a few centimeters long, harm the fibre positioning immensely. A heating and smoothing procedure of the fibre has been developed [55], to remove these thick spots, so-called bumps. More details can be found in Chap. 5. Another crucial mechanical property is the elasticity of the scintillating fibre. During winding of fibre mats a certain tension on the fibre is needed. The standard value for the force resulting in the needed tension is 50 cN. Studies have shown, that such a tension on a 2.8 m long fibre leads to an expansion of around 1 cm [56]. The contraction of the fibre mat after cutting it perpendicular to the fibres to flatten the mat has also been observed to be in that range. But also after cutting the fibre mat off the winding wheel, the mat still continues shrinking. This effect has been observed during the early phase of the serial production of fibre mats and dedicated studies have been performed in this thesis, which are further described in Chap. 7.

6.2. The xy-table setup

Attenuation measurements are used to determine the quality and behaviour of scintillating fibres under different conditions. This is done by exciting the fibre at different positions and measuring the amount of light reaching the fibre end. The measurement of the attenuation does not require an excitation with ionizing particles, hence usually an UV-LED is used for this purpose. It does not trigger the scintillation process but excites the wavelength shifter inside the fibre core. The amount of light can be measured with a simple photo detector, counting the arriving photons, or using a spectrometer to measure also the wavelength dependency. A reliable excitation with a good reproducibility is achieved by a dedicated setup, which has been developed in context of this thesis. A setup containing two axes each equipped with a linear slide powered by a stepping motor as shown in Fig. 6.5, has been found to be the best option. The motor is able to perform micro steps and allows a precise positioning of the linear slide. The x-axis provides a traverse distance of 2.5 m and its slide is carrying the y-axis. This y-axis allows a traverse distance of about 25 cm. Parallel to the x-axis *e.g.* scintillating fibres can be placed and adjusted. One side of the fibre is connected to a spectrometer collecting the arriving photons. The whole setup is operated with the help of a PC. A dedicated program has been developed to assure the combination of talking to the two motors of the x- and y-axis respectively as well as performing measurements with the spectrometer. For the excitation of the scintillating fibre, two different options can be used, based on one or multiple UV-LEDs mounted on the slide of the y-axis. These LEDs are connected via a programmable current source to the PC, such that switching the LED for a measurement can be done automatically.

The first possibility to excite the fibre is realised by the setup shown in Fig. 6.5. Mostly fibre mats are being measured in this measurement mode. A single UV-LED is mounted on the y-axis and can be moved along and across the fibre mat. However, the light
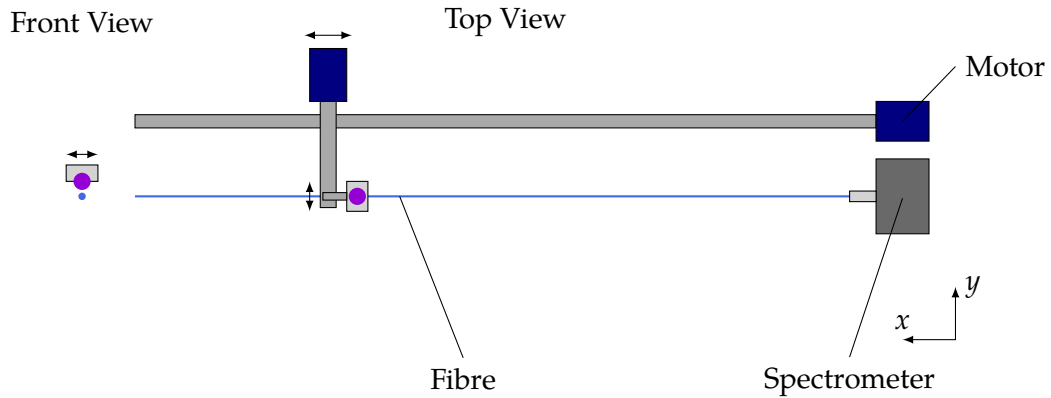
Fig. 6.5.: Sketch of the xy-table. This setup can be used to measure the attenuation length of a scintillating fibre and/or narrow fibre mats. An UV-LED is mounted on the y-axis of the table moving along and across the fibre and measuring the light output with the help of a spectrometer. All devices are connected to a PC and are being operated by a single program.

output is dependent on the positioning of the LED, which is shown in Fig. 6.6. The LED will move at each x-position across the fibre mat to determine the maximum light yield with a spectrometer measurement. This accounts for the systematics that a fibre mat cannot be aligned totally parallel to the x-axis. The second possibility is only based on the x-axis and is illustrated in Fig. 6.7. This measurement mode is only possible for single scintillating fibres. A small housing containing four LEDs assures a proper excitation of the fibre from each side as the fibre is guided via a small hole through this housing. However, this option requires a constant position in y for the housing and as well a well adjusted scintillating fibre.

The spectrometer performs a dark count measurement at each x-position. For the light measurement it is possible to either perform one light measurement with a fixed current for the LED or three light measurements with three different currents to aim for higher statistics at lower and higher wavelengths of the fibre spectrum. Also other parameters, such as the integration time of the spectrometer or of how many measurements shall be averaged, can be set. A graphical user interface version has been created, which allows to enter the parameters of the xy- and spectrometer measurement with which the xy-measurement is being performed automatically. Parameters for the xy-table are for example the distance between the measurements and number of of these on each axis. A screen shot of the interface is shown in Fig. 6.8.

6.3. Light guidance studies

The dedicated setup, described in the previous section, allow a reliable excitation with a good reproducibility and is used for several measurements on single scintillating fibres and narrow fibre mats during this thesis. As explained previously, the light guidance in a fibre is affected by several factors, such as absorption and scattering, but also affected by impurities of the base material. In the following, the analysis procedures for single fibres and fibre mats are explained shortly.
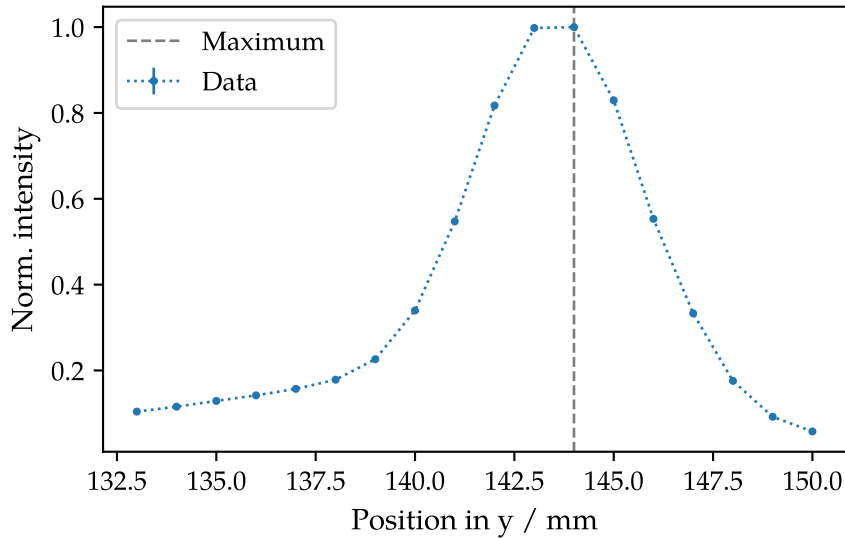
Fig. 6.6.: Intensity at the end of a scintillating fibre mat for different positions across the fibre mat width. The maximum is determined at a position of around 144 mm.

The attenuation for single scintillating fibres is determined via a fit of a single exponential function, according to Eq. (6.2), to the intensities ≥1 m, as shown in Fig. 6.9. This procedure has been agreed on in the LHCb SciFi group along with the fibre manufacturer to ensure a good comparison between different measurements in different labs. In addition, it only accounts for photons travelling along the fibre axis, as photons following a helix path are already attenuated due to their longer track length and a higher number of reflections at the boundaries (core-cladding and cladding-cladding).

For fibre mats, the analysis procedure is slightly different. Due to their width and properties, it is not possible to homogeneously excite the mat at each position. The main source of the different level of excitation is caused by glue on top of the fibre mats. Attenuation measurements on fibre mats are performed with the setup shown in Fig. 6.5. A single UV-LED is mounted on the *y*-axis, which is moving across the width of the fibre mat. The intensity trend for crossing the mat width, see Fig. 6.6, is attenuated along the mat length on the *x*-axis, like shown in Fig. 6.10. At each *x* position, the maximum in *y* is determined and used for the attenuation analysis. It is clearly visible that the maximum is shifted to higher *y* positions between 132 mm and 144 mm for higher *x* distances, which means the mat was not aligned perfectly but with a slope of about 1 cm along the fibre mat length.

In Fig. 6.10 is it already visible, that the maximum intensity does not drop evenly, it even rises in between some measurement points. This is a result of the different excitation strengths, which is caused by glue on top of the fibre mat or an incorrect positioning of the LED above the mat. For this reason, the light output at each position is determined from both directions. This means the spectrometer is connected to both fibre mat ends (*A* and *B*) successively and the measurement repeated ensuring that the same mat position is being excited. Plotting the both intensity against the *x*-position of the fibre mat yield the result shown in Fig. 6.11. The fluctuations are clearly visible and would lead to a too high or too low attenuation coefficient. Therefore a correction is applied, which takes into account, that physically the attenuation should be equal between the two *x* positions. If
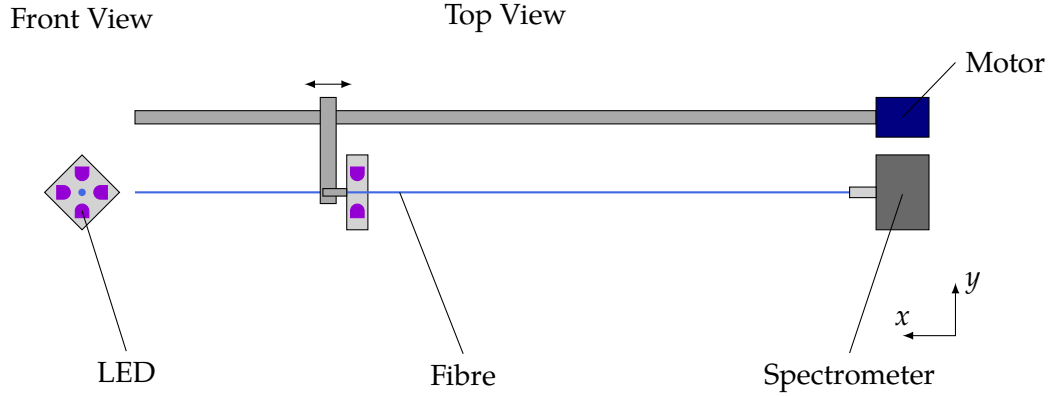
Fig. 6.7.: Setup to measure the attenuation of a single scintillating fibre: the LED housing contains 4 LEDs surrounding the fibre and exciting it. With the help of the *x*-axis, the position along the fibre axis can be changed.
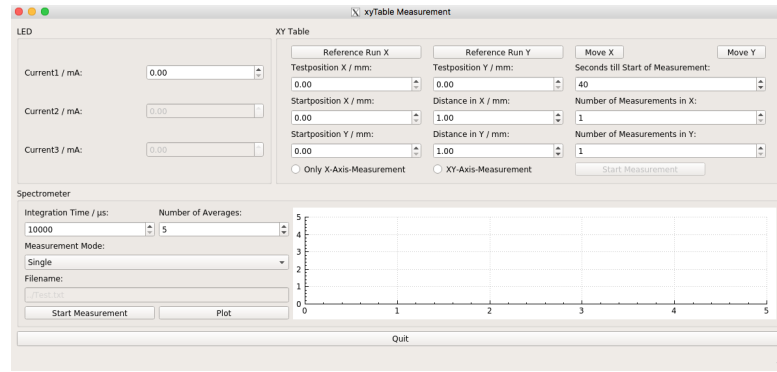
Fig. 6.8.: Screen shot of the graphical user interface of the program operating the *xy*-table measurements. It is easy to use, as just the parameters of the measurement for the axis and the spectrometer have to be entered. Afterwards everything is done automatically.

a certain *x* position the excitation strength is too low, it will happen from both directions. By multiplying with a correction factor c_i these deviations are compensated. With the help of this assumption, the correction factors c_i can be calculated, as follows:

$$c_{i+1} = c_i \cdot \sqrt{\frac{A_i \cdot B_i}{A_{i+1} \cdot B_{i+1}}}, \tag{6.9}$$

where A_i and B_i represent the measured intensities at the particular *x* positions and fibre mat end. The relation needs an initial value, which is set to $c_0 = 1$. As already mentioned, the spectrum of the fibre mat is shifted to larger wavelengths with increasing excitation distance to the detector. To account for this effect, only the intensities at the peak wavelengths are used to calculate the correction factors. Applying the correction factors to the previously shown intensity trend by multiplying them with the intensities results in a trend shown in Fig. 6.12. A clear smoothing of the data points is visible, such that the attenuation factor is determined more precisely.
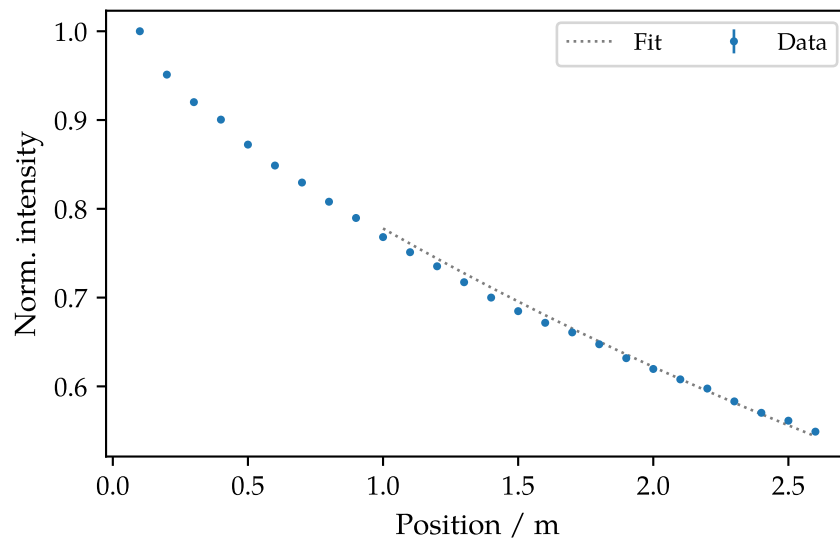
Fig. 6.9.: Intensity at the fibre end for different excitation positions. The attenuation factor is determined with a single exponential function fitted to the intensities ≥1 m (grey dotted line).
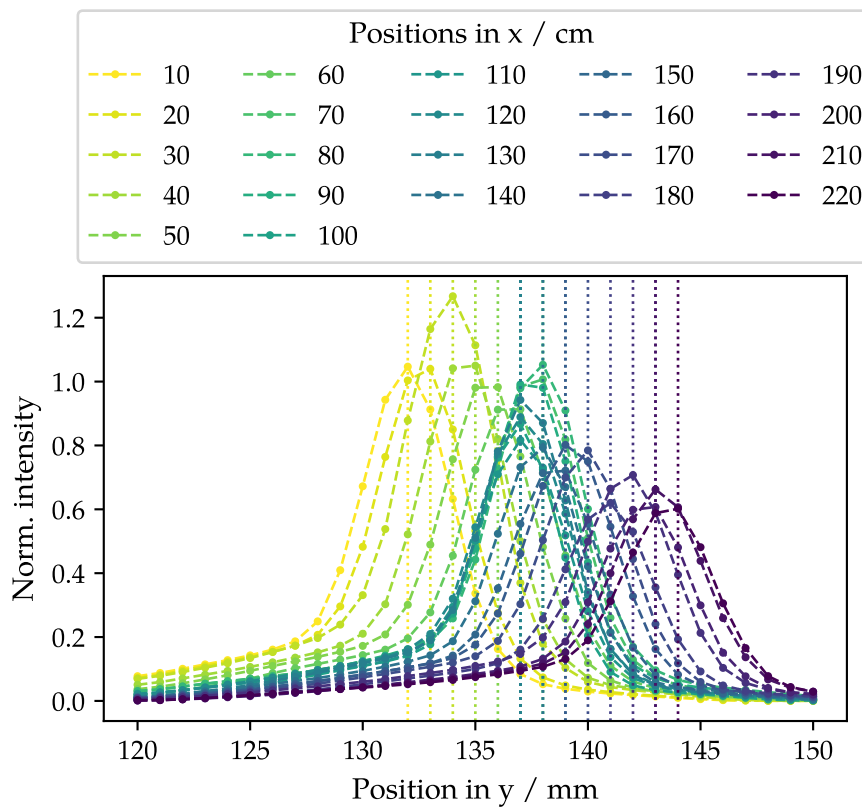
Fig. 6.10.: Intensity profile across a fibre mat width for different positions along the mat length. The maximum y position at each x position is determined.
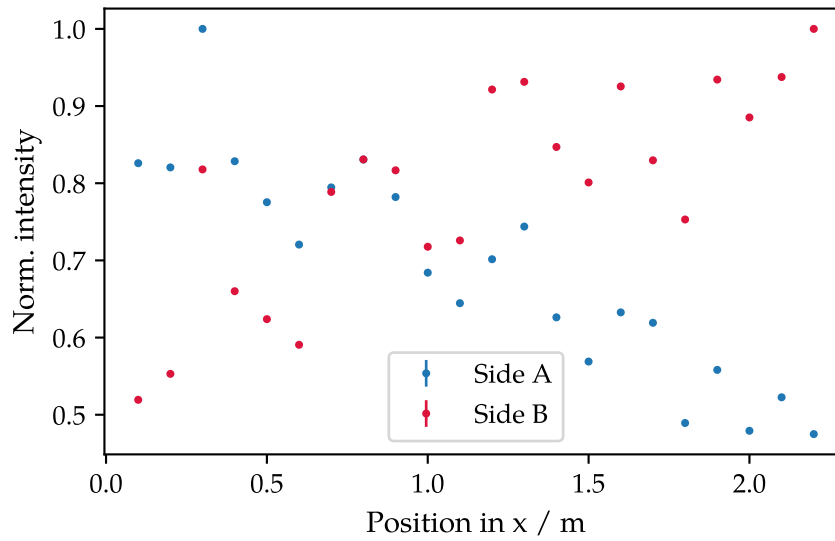
Fig. 6.11.: Intensity trend measured at both fibre mat ends, *A* and *B*, respectively. The data points show a fluctuation due to an inhomogeneous excitation, which can lead to a too high or too low determined attenuation factor.
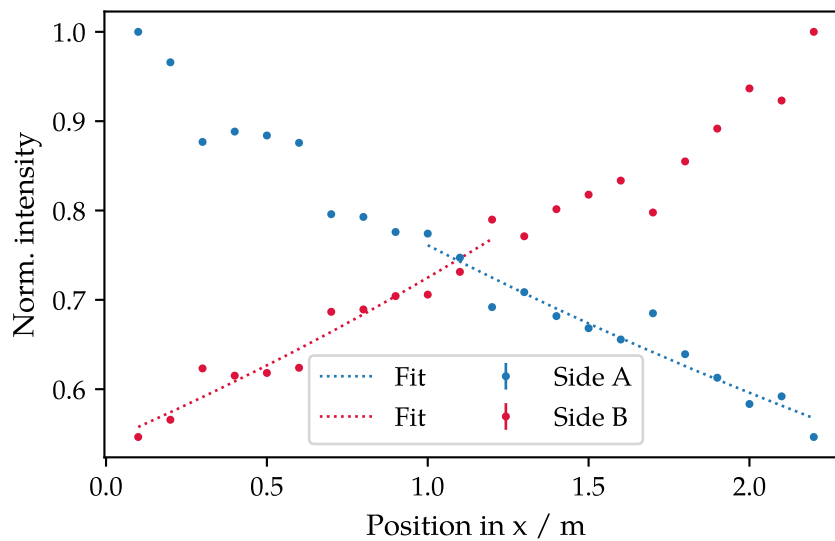
Fig. 6.12.: Intensity trend measured at both fibre mat ends, *A* and *B*, respectively. The intensity at each position is corrected according to Eq. (6.9), which results in a smoothing and therefore a more precise determination of the attenuation factor.

6.3.1. Angular dependencies of the attenuation length

In contrast to the real SciFi Tracker, single fibre measurements are performed in air, which enables total reflection at the outer boundary of the fibre as the refractive index of air (=1) is smaller than the refractive index of the outer fibre cladding (=1.42). Therefore, a large increase in light yield is expected for large angles, so that it is necessary to know if and how the intensity and the attenuation length is dependent on the exit angle of the photons.

A measurement setup has been constructed allowing to rotate the spectrometer around the fibre end [68, 69]. With an enhanced fibre holder this setup has been integrated into the *xy*-table setup (Fig. 6.13), such that a semi-automatic measurement is possible. The
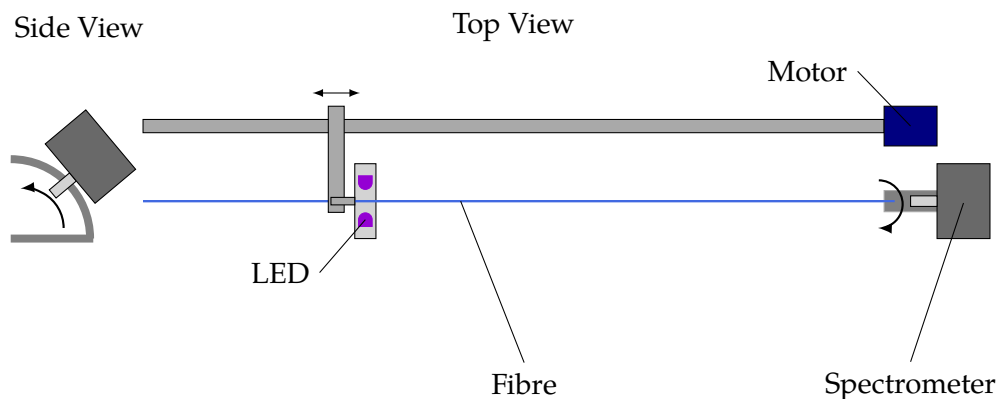
Fig. 6.13.: Setup for angular dependent measurements based on the *xy*-table. The LED housing contains four LEDs surrounding the fibre and exciting it properly. The Spectrometer is hold by an half arc, such that the vertical angle can be changed by mounting the spectrometer to a different height while the horizontal angle is changed with rotation.

spectrometer is placed at a distance of 6 cm with respect to the fibre end, a compromise between intensity and angle resolution. Horizontal angles can be changed by rotating the arm, which allows a range from −90° to 90°. In vertical direction the spectrometer can be mounted at different heights from 0° to 80°. At each angular position, an automatic attenuation measurement is performed, followed by a manual change of the angular position.

Figure 6.14 shows the normalised intensity for an excitation in a distance of 10 cm from the fibre end as a function of the vertical and horizontal angle. The maximum does not accord with the centre[2], but is determined to be at (0°,10°), which means the fibre centre was not perfectly aligned with the centre of the setup. Nevertheless, the expected radial symmetry is clearly visible. The angle under which most photons are exiting the fibre can be determined by integrating the intensity over the solid angle. The results are shown in Fig. 6.15 for different excitation distances. Photons exit the fibre end at most with an angle of between 30° and 40°, but the maximum shifts with increasing distance to the point of excitation to lower angles. Higher angles have a smaller contribution to the total intensity with growing distance to the photo detector. The obtained maxima are shown in Fig. 6.16 as a function of the excitation distance. With a maximum at nearly 35°, the trend drops quickly to 33.5° at a distance of 240 cm. As this shift is very low, it can be neglected.
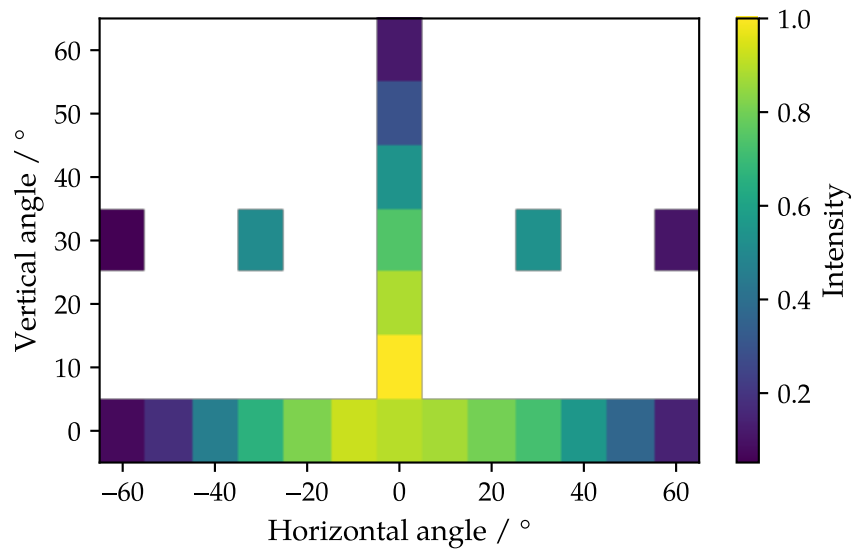
---

[2]Horizontal and vertical angle is 0°.

Fig. 6.14.: Normalised intensity for an excitation in a distance of 10 cm as a function of vertical and horizontal angles. Assuming a symmetry only dedicated angles were measured. Due to a non-perfect alignment of the fibre centre, the maximum is shifted to a vertical angle of 10°.
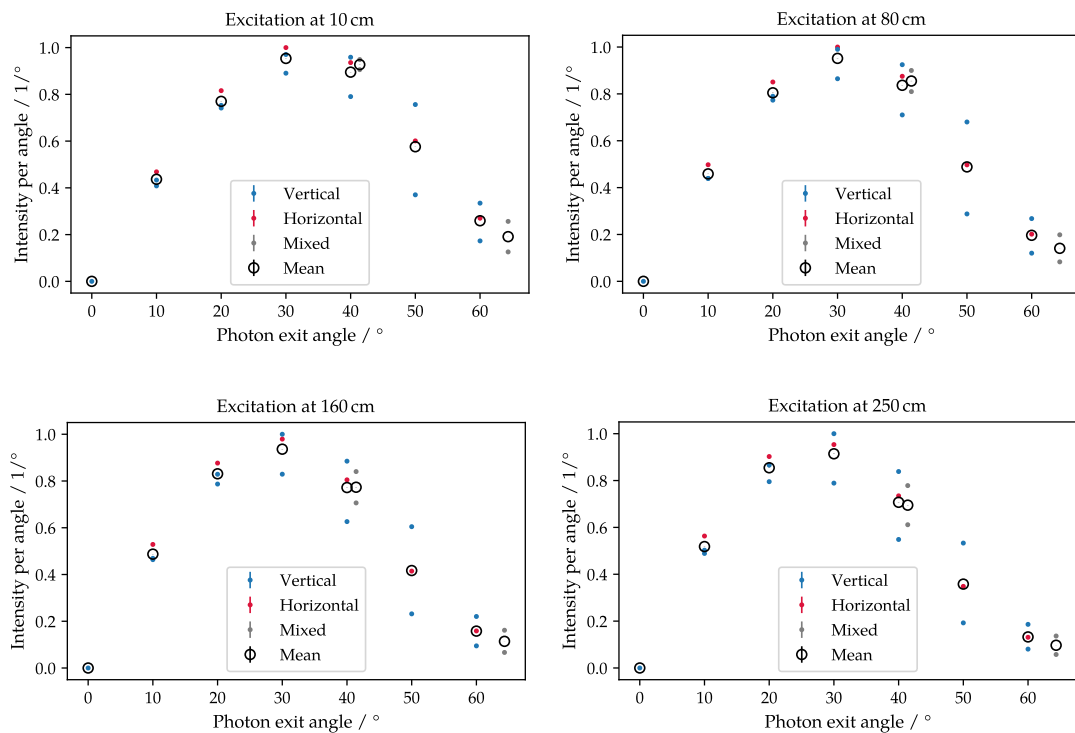

Fig. 6.15.: Normalised intensity as a function of the photon exit angle for different excitation distances. The mean is shifting to higher angles, while suppressing contributions with larger angles with increasing distance.
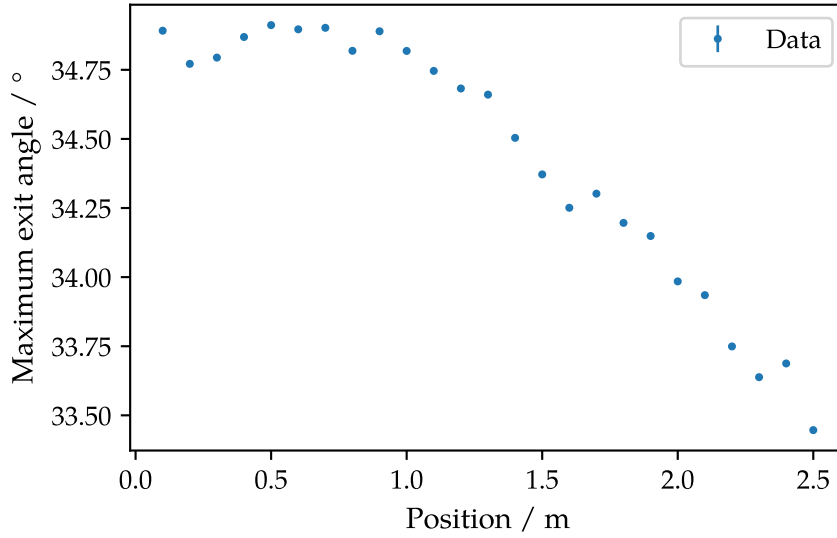
Fig. 6.16.: Maximum exit angle of photons as a function of the excitation distance. The maximum in decreasing with higher excitation distances.

Photons leaving the fibre with a large angle undergo many reflections inside the fibre as photons leaving under a small angle with respect to the fibre axis. The path length L and number of reflections scale different with the angle, see Eq. (6.5) and Eq. (6.3). Therefore, the attenuation at higher angles is influenced by reflection losses at the cladding boundaries. Figure 6.17 shows measured attenuation factors as a function of the horizontal and vertical angle. The attenuation is increasing with the angle, which can be also seen in Fig. 6.18, where the attenuation as a function of the photon exit angle and the wavelength dependency is shown. The uncertainties contain both: statistical uncertainties and uncertainties obtained from the fit. It is clearly visible that the attenuation is increasing with higher photon exit angles. This behaviour is similar for the different wavelengths of the fibre spectrum.

As previously mentioned, the attenuation for higher angles is dominated by reflection losses due to the increased number of reflections. Assuming that the attenuations just add up the total attenuation is given by:

$$a_{\mathrm{tot}}(\theta) = a_{\mathrm{core,\,0°}} \cdot c_{\mathrm{path}}(\theta) + a_{\mathrm{refl.}}(\theta), \tag{6.10}$$

where $a_{\mathrm{refl.}}$ equals zero for 0° and c_{path} is the correction for different path lengths with different angles and can be calculated according to Eq. (6.3). Therefore, $a_{\mathrm{core,\,0°}}$ can be assigned to the total attenuation factor for 0°. Figure 6.19 shows the reflection loss factor $a_{\mathrm{refl.}}$ as a function of the photon exit angle for different wavelengths. The uncertainties contain both: statistical uncertainties and uncertainties obtained from the fit A strong dependence is visible: with higher angles the reflection loss factor is increasing. In addition, a rising spread in the wavelength dependency is apparent. For lower photon exit angles, the different wavelengths have similar reflection loss factors as for higher angles the absolute differences are larger. Nevertheless, an analogue trend of the reflection loss factor with the angle as for the total attenuation factor is obtained. But for most angles (<40°), the reflection loss factor is smaller than the attenuation inside the core.
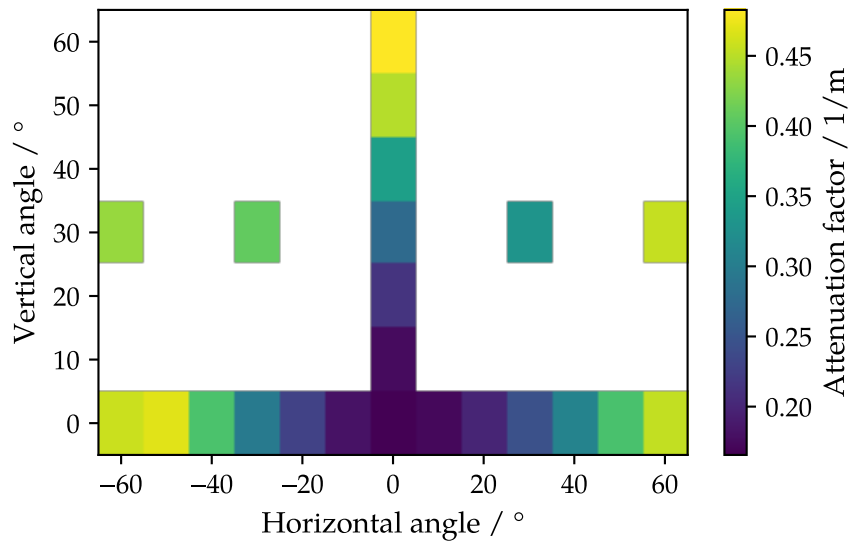
Fig. 6.17.: Attenuation factors as a function of the horizontal and vertical angle. Photons leaving the fibre under an increased angle, undergo much more reflections and their attenuation is dominated by reflection losses at the cladding boundaries.
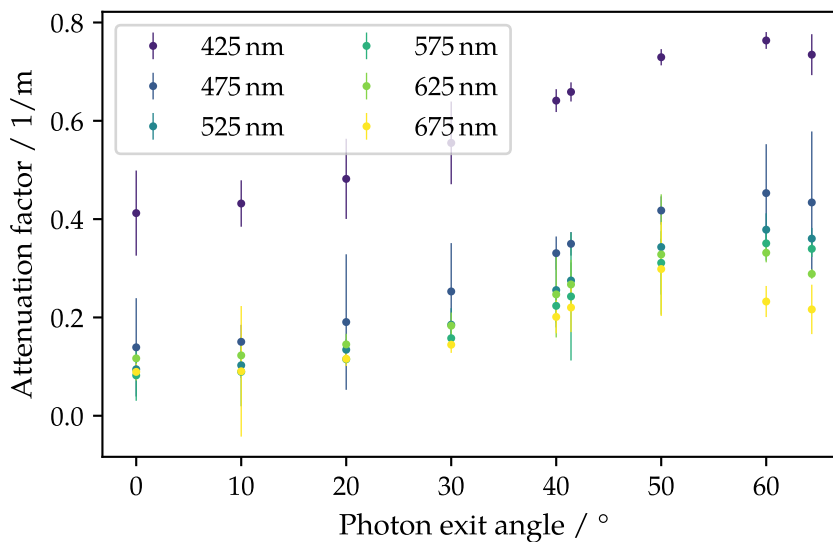

Fig. 6.18.: Attenuation factor as a function of the photon exit angle for different wavelengths. The attenuation is increasing with the angle but seems to saturate at an angle of 60°.
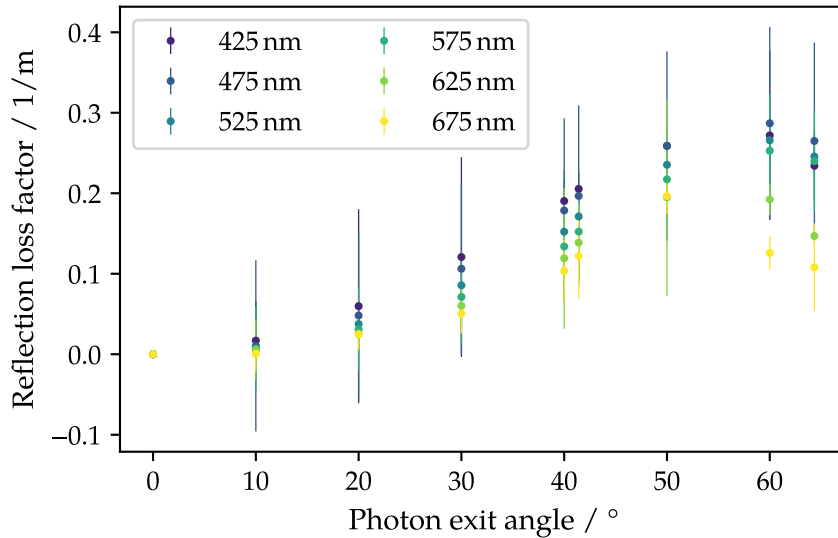
Fig. 6.19.: Reflection loss factor as a function of the photon exit angle and the wavelength. With increasing angle, the reflection loss factor is rising, as higher photon exit angle require a higher number of reflections. Also a larger spread for the wavelength dependency is visible for higher angles.

The performed measurements were performed in a semi-automatic way and therefore have the potential for systematic errors, like adjusting the horizontal angle by rotation or centering the fibre in the rotation spot. A master thesis [70] is currently under preparation, to build a more enhanced setup, to reduce those uncertainties. It enables an automatic angle adjustment and therefore finer grained binning of the angles and higher accuracy. Also other systematic uncertainties like the temperature of the spectrometer and the used UV-LED are being studied. With the working full automatic setup a larger number of datasets can be acquired, leading to a statistically more precise analysis.

6.3.2. Impact of winding fibres to a wheel

During the production of fibre mats (see Sec. 5.2.2) the single scintillating fibres get wound on a grooved wheel with a circumference of about 80 cm. A feeding spool is providing the scintillating fibre, which is then guided by several spools with about 15 cm circumference to the winding wheel. As the fibre mat winding is a delicate process and the fibre is not protected, it needs to be assured that no damage is applied. For example, residuals of glue on the winding wheel or the small diameter of the guiding spools could lead to a potential damage of the fibre cladding and as a result lower the attenuation length of the fibre.

Therefore, a test has been performed where fibres from the same target spool are wound on the winding wheel several times. Three fibre batches have been created, which was wound on the winding wheel one time, five and ten times, respectively. Hereby one time means, that the fibre was wound back and forth once. Each batch was measured with regard to their attenuation factors on the *xy*-table. The determined attenuation factors can be obtained from the histograms in Fig. 6.20. It is clearly visible that winding the fibres ten times leads to an increase of the attenuation factor, while the batches which
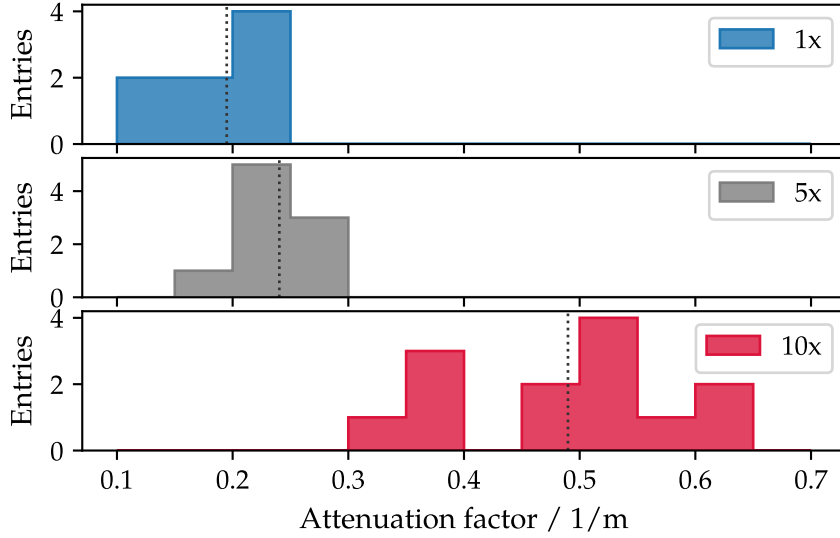
Fig. 6.20.: Measured attenuation factors for batches of fibres. The fibres got wound on a winding wheel once (upper most), five (middle) and ten times (lower).

got wound once and five times are comparable within their uncertainties. The mean attenuation factors were determined to be

$$a_{1x} = (0.19 \pm 0.04) \, \frac{1}{m},$$

$$a_{5x} = (0.24 \pm 0.03) \, \frac{1}{m},$$

$$a_{10x} = (0.49 \pm 0.10) \, \frac{1}{m},$$

where the given uncertainties represent the standard deviation of the distribution. Assuming a basic attenuation of $0.2 \, \frac{1}{m}$, the additional attenuation due to ten times back and forth winding can be determined to be $0.3 \, \frac{1}{m}$. This gives an additional attenuation due to winding the fibre once of $^{0.3}/_{20} \frac{1}{m} = 0.015 \, \frac{1}{m}$. The loss in light yield for a 2.5 m long fibre can be determined accordingly to be

$$1 - \exp\left(-2.5 \, \text{m} \cdot 0.015 \, \text{m}^{-1}\right) = 0.04,$$

which means, that the light yield of the fibres after winding is decreased by 4%. However these are just theoretical considerations and the results for winding just once show attenuations in a low range. Nevertheless multiple rewinds *e.g.* due to errors in the fibre matrix, see Fig. 7.1, should be avoided. Although only a small fraction of the fibre would be affected.

6.3.3. Effect of watering and heating fibres

The length of a fibre mat is very sensitive to temperature and humidity changes (see Sec. 7.2). To test, if their performance is being harmed, single fibres were exposed to water and their attenuation measured. As reference, the fibre batch was also measured before exposure. The fibres were kept in a water vessel for one hour to ensure that the

humidity is diffused into the scintillating fibre. The measurement on the wet fibre was performed as fast as possible to oppress drying effects. The distribution of the reference attenuation factors and of the wet fibres are shown in Fig. 6.21. The water can also
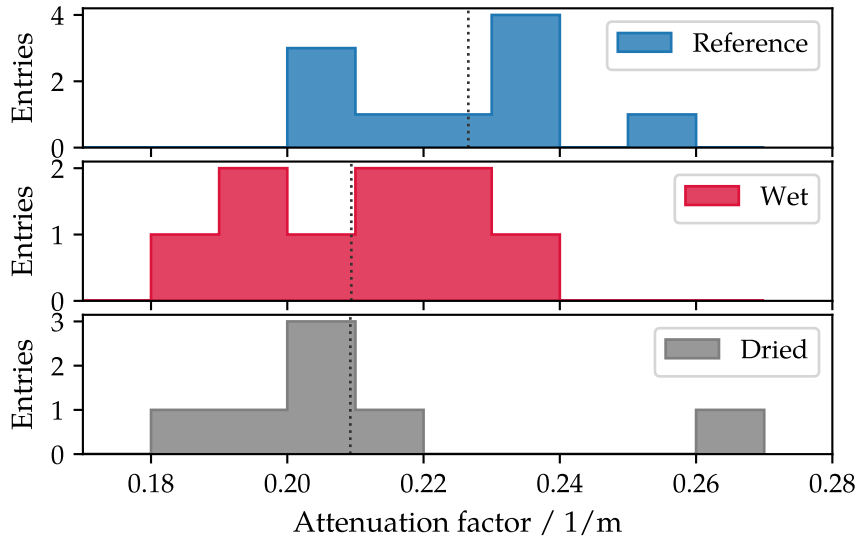
Fig. 6.21.: Histogram of measured attenuation factors for fibres which got watered and dried afterwards.

serve as an addition cladding and due to its lower refractive index allows a better light guidance. Therefore, the measured attenuation factor of the wet fibres seem to be slightly decreased. The same fibres were measured after they dried for one week. With this measurement the effect of the diffusion of the water off the fibre is determined. The mean of the particular measured distribution is determined to be

$$a_{\text{ref}} = (0.23 \pm 0.02) \, \frac{1}{\text{m}}$$

$$a_{\text{wet}} = (0.20 \pm 0.03) \, \frac{1}{\text{m}}$$

$$a_{\text{dried}} = (0.21 \pm 0.02) \, \frac{1}{\text{m}},$$

where the given uncertainties represent the standard deviation of the distribution. Within their uncertainties, the measured attenuation factors under the three conditions are compatible. In addition, a fibre mat was moistened and the change in length measured. The performance of the fibre mat afterwards was not decreased and also the length change was within expectations. Summarising, no impact of water to the attenuation of the fibres could be observed.

In addition, the impact of different temperatures to the fibre performance was studied. The normal procedure during the serial production is to heat up the fibre mats to reduce transversal bending, see Chap. 5. It was found that heating the mat to 40 °C results in a flat mat without damaging the fibres and their performance. For this study, a narrow fibre mat was used to measure the impact of the glue. The mat was heated up in 10 °C steps and afterwards attenuation and light yield measured. For the attenuation measurement the *xy*-table (Fig. 6.5) was used and for the light yield measurement a

dedicated setup for the serial production of fibre mats was used (see Fig. 7.34). The fibre mat was coiled and heated up in a standard lab oven. During these measurements it was found, that the epoxy glue is very sensitive to heat and softens very easily. Thus the fibre mat was flattened very fast after removing it from the oven, it was not possible to get rid of deformations completely, as shown in Fig. 6.22.
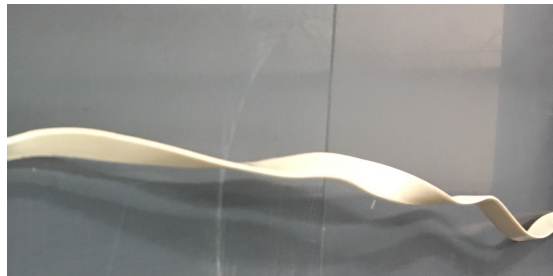

Fig. 6.22.: A fibre mat which got heated up to different temperatures. Due to the temperature the epoxy glue in between the fibres gets soft and deformations can occur.

However, due to these deformations, it was not possible to measure the attenuation and with high precision for all temperatures. Therefore, only light yield measurement results are presented here. The light yield trend as a function of the temperature is shown in Fig. 6.23. The error bars represent the statistical uncertainties. It is visible that the light
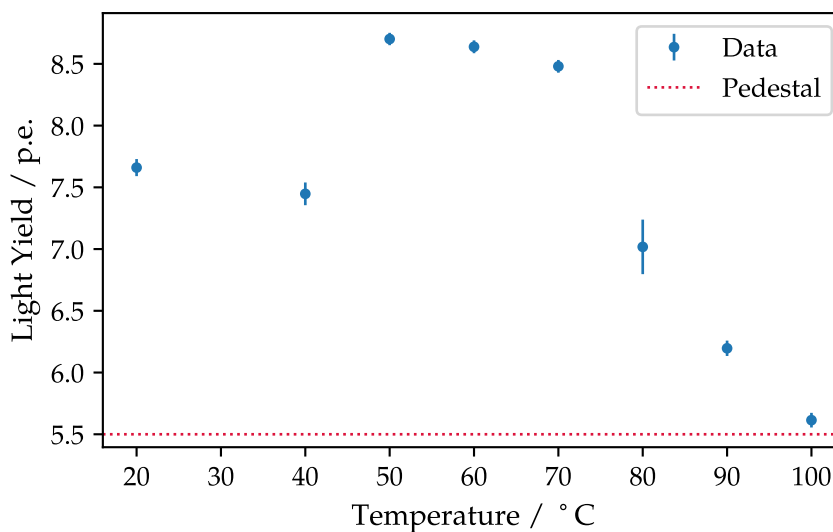
Fig. 6.23.: Measured light yield for a narrow fibre mat, which got heated up to different temperatures.

yield is not reduced up to 80 °C and even improves with temperature between 50 °C and 70 °C. Heating the fibre mat up to 100 °C did not show any signal higher than the noise cluster rate (pedestal)[3]. In addition heating up to 40 °C does not impact the performance of the fibre. Therefore, the tempering procedure is not critical.

---

[3]Due to the clustering procedure, the noise represents the sum threshold.

6.4. In situ irradiation in the LHCb cavern

The LHCb SciFi Tracker will be harmed by radiation damage mainly in the central region of the detector. As most tracks are passing close to the beam pipe, this part suffers most. The amount of light reaching the SiPMs is an essential parameter for the performance of the tracker. Hence, several irradiation campaigns have been performed by the LHCb SciFi group with the goal to determine the increase in attenuation for the different doses. In the course of this thesis an additional in situ irradiation has been performed, of which the results will be described in the following. Reaching high doses on fibres is simple by irradiating them at beam lines, but at the cost of a high dose rate. As described before, the radiation damage is also strongly dependent on the dose rate, therefore low dose rate irradiations are quite interesting as the environment for the SciFi tracker in the LHCb cavern will be dominated by low dose rates. So far mid to high dose (at high dose rates [31]) and low dose (at low dose rates [56]) measurements have been performed. The here presented irradiation campaign aims for a low dose rate but for a higher total dose. In addition, a damage trend over time is studied.

6.4.1. Setup

A narrow fibre mat with about 1.5 cm width and 6 layers of fibres, has been installed in the LHCb cavern for an in situ irradiation, which enables a comparable dose rate like later on for the SciFi tracker. The 2.5 m long fibre module has been installed at the shielding wall towards the LHC tunnel, which is situated near the VELO. The exact position of the module at the shielding wall is shown in Fig. 6.24 and was chosen to be as close as possible to the beam pipe and enabling a module length as long as possible. A setup containing two SiPMs enables a measurement of the time dependent trend of the radiation damage. During runs of the LHC with collisions taking place at LHCb in the VELO, the created particles cause radiation damage to the fibres and in addition excite the fibre mat, which can be measured by the first SiPM connected to the fibre mat. As shown in Fig. 6.24, the SiPMs are located as far as possible from the beam pipe. However, the SiPMs are irradiated and, as mentioned in Chap. 4, show a rise in the dark count rate. Therefore it was chosen to use SiPMs, which can be cooled by a Peltier element in order to lower the dark count rate. To determine the dark count rate, a second SiPM is necessary, as the first one will always measure the combination of the signal created by particles exciting the fibre mat and the dark counts of the SiPM itself. The second SiPM was placed directly next to the first SiPM, such that they are irradiated in the same way. The used SiPMs are from Hamamatsu (S13362-1350DG) with an active surface of 1×1 mm. The fibre mat has been glued to a support consisting of Rohacell® structural foam[4] and carbon fibre. A aluminium support is attached to the Rohacell® which holds the two SiPMs and serves as mounting point for the installation at the shielding wall (see Fig. A.1 and Fig. A.2 in the appendix).

The dosimetry measurement has been done with the help of five alanine sticks, which got positioned along the fibre mat length. Alanine is a simple amino-acid which radiation effect is monotonically linearly dependent on the absorbed dose. The quantity proportional to an absorbed dose is number of radicals. The number of radicals can be measured with the help of electron paramagnetic resonance (EPR) as it is proportional to double integral of the EPR signal. In dosimetry practice an amplitude of the highest
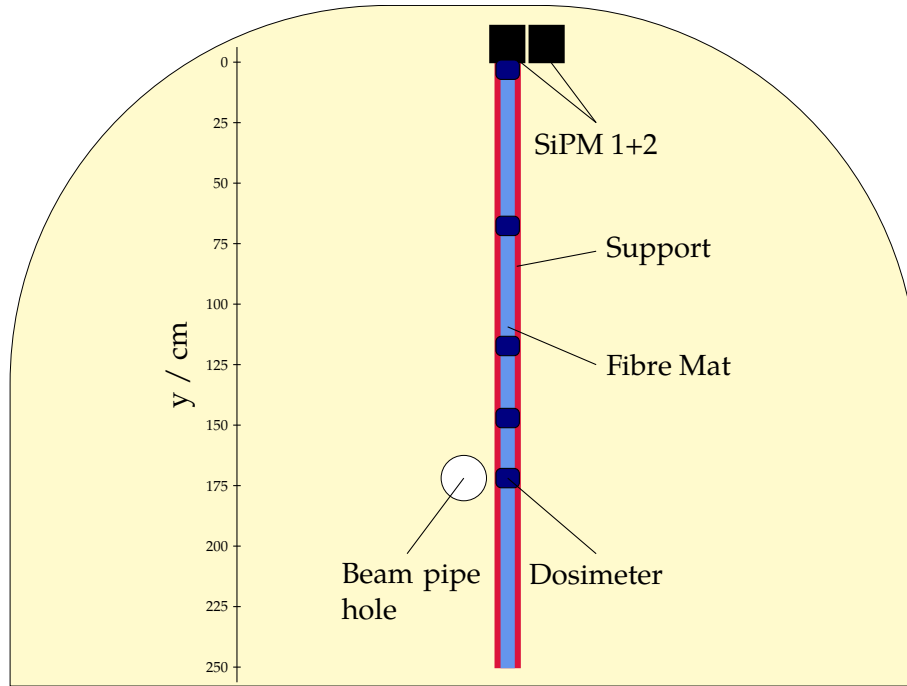
---

[4] http://www.rohacell.com/product/rohacell/en/

Fig. 6.24.: Setup in the LHCb cavern. The fibre module is installed at the shielding wall to the tunnel, close to the VELO. The position was chosen to be as close as possible to the beam pipe with the fibre module as long as possible. The distance to the centre of the beam pipe amounts to 11 cm. Two SiPMs are read out every 30 s, one serving as reference while the other is connected to the fibre mat.

line of EPR signal is used as dosimetry signal. In Fig. 6.25 a FLUKA simulation [71] of the dose distribution at the shielding wall [72] is shown, which shows a steep rise in the dose around the beam pipe. Therefore, the positions for the dosimeters d_i have been chosen to be

$$d_1 : 5 \, \text{cm},$$
$$d_2 : 70 \, \text{cm},$$
$$d_3 : 120 \, \text{cm},$$
$$d_4 : 150 \, \text{cm},$$
$$d_5 : 175 \, \text{cm},$$

under the assumption of a symmetric dose profile around the beam pipe.

The whole setup was installed during the third Technical Stop (TS) in November 2016 and stayed until December 2017. The dosimeters were read out three times: first, during the EYETS (Extended Year End Technical Stop) beginning of 2017 to have the possibility to distinguish between the ion runs at the end of 2016 and the upcoming protons runs in 2017. In addition they were read out during TS2 in September 2017 and at the end of the irradiation in December 2017.

During the whole irradiation, the setup shown in Fig. 6.26 enables measurements of the signals of both SiPMs. The measurement setup is composed of a SourceMeter providing both SiPMs with the correct bias voltage and an additional power supply powering the Peltier elements of the SiPMs. A measurement of the temperature of the SiPMs is carried
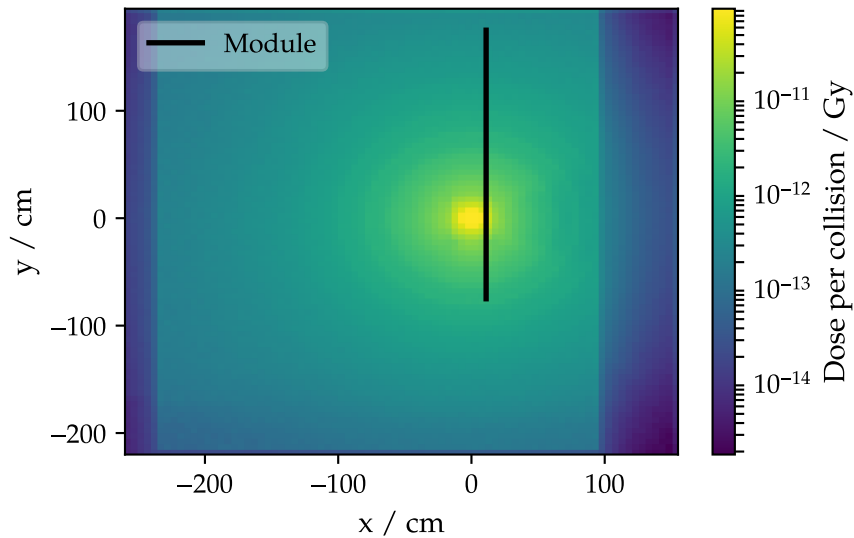
Fig. 6.25.: Radiation environment of the shielding wall inside the LHCb cavern determined by FLUKA simulations. The position of the irradiated module is shown in black.

out by a thermistor and a multimeter. All measurement devices are placed in the counting house outside the LHCb cavern and are connected via GPIB (General Purpose Interface Bus, a short range digital communication 8-bit parallel interface bus specification) to a server PC. A software has been developed to control device and measurement settings, perform test sequences and save the acquired data. In the course of the irradiation, every 30 s the signal of both SiPMs and their temperature have been measured and saved to disk. As mentioned before, the SiPMs were cooled by Peltier elements. A stable temperature was reached with the help of a small control circuit, which measured the actual temperature and adapted the voltage according to the target temperature.

6.4.2. Dosimetry and integrated luminosity

The dose measurements are shown Fig. 6.27. The uncertainties were assumed to be 10% [72]. A fit along the total module length has been performed assuming that the dose profile is symmetrically around the beam pipe. The dose peaks around 175 cm, at the position of the beam pipe (see also Fig. 6.24), and decreases exponentially in both directions. The trend is the same over time, but the dose increases clearly. After the irradiation of about 380 days inside the LHCb cavern, the final dose peaks at (6.3 ± 0.6) kGy. Taking the dose profile into account gives an average dose over the whole module length of (1.7 ± 0.2) kGy.

The collected dose should be proportional to the delivered luminosity in the LHCb detector. The corresponding integrated luminosity over the irradiation time is shown in Fig. 6.28. Time ranges with no collisions inside the LHCb detector occur as horizontal lines. In the beginning of the irradiation, ion runs were performed, where not much luminosity had been collected compared to the proton runs. But the applied dose is clearly visible in the first measurement of the dosimeters. After the total irradiation, the applied dose matches with an integrated luminosity of $1989 \, \text{pb}^{-1}$. With the help of the
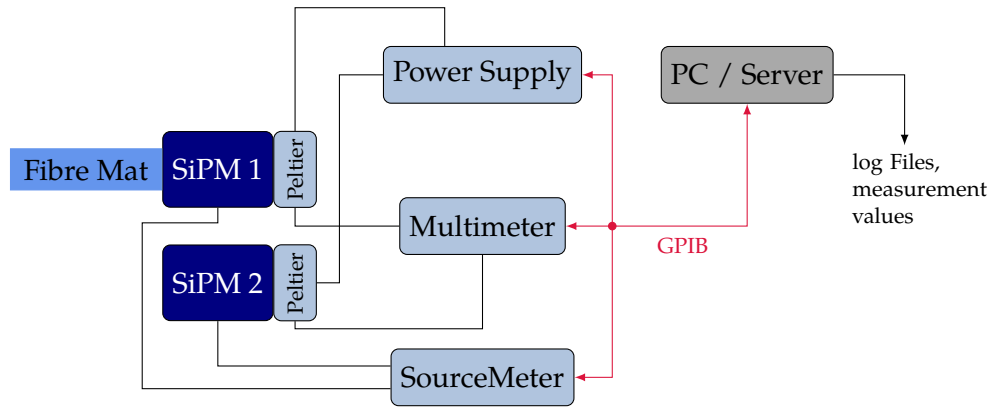
Fig. 6.26.: Measurement setup for the in situ irradiation. The SiPMs are cooled by Peltier elements and powered by a SourceMeter. In addition, a thermistor connected to a multimeter measures the temperature of the SiPMs. All devices are connected via GPIB and controlled by a PC, which saves all log files and measurement values. The fibre mat is indicated facing one SiPM. SiPMs and fibre module were placed in the LHCb cavern at the shielding wall (Fig. 6.24), while all electronic devices were placed in the counting house outside the cavern.

luminosity trend and the three dose measurements, a dose trend over time is determined. Figure 6.29 shows the dose trend over time and depending on the position along the fibre module.

Before starting the irradiation campaign, the radiation map of the shielding wall (see Fig. 6.25), which is created by Fluka simulations [71], was used to determine which dose can be expected. In Fig. 6.30 the calculated dose profile in comparison with the measured one is presented. Both are matching well.

6.4.3. Signal over time

Before starting the irradiation campaign simple calculations have been done to determine the loss of signal at the SiPMs due to the irradiation to see, if it is a measurable effect. For this, the intrinsically and radiation induced attenuation have been calculated. The intrinsic attenuation has been calculated according to Fig. 6.3 and for the radiation induced attenuation the power law model Eq. (6.7) has been used. The excitation is not at specific positions but proportional to the dose profile, such that the signal at the end of the fibre mat sums up over all positions. With the Fluka simulated dose distribution a signal loss of about 20% was calculated, see Fig. 6.31. This calculation takes only simple assumptions into account, like the radiation induced attenuation and the intrinsic attenuation. For example in the intrinsic induced attenuation, no photon loss at the boundaries was taken into account.

Figure 6.32 shows the measured current trend of both SiPMs. The reference SiPM only measures dark counts, which increase over the time due to irradiation. In addition, the current at the SiPM connected to the fibre module is shown. The baseline follows the one of the reference SiPM, but in addition peaks are visible, which refer to signal coming from the fibre mat. The cleaned signal is the difference of these two trends. Furthermore, the fibre mat only creates signal when the LHC is running and collisions are taking place inside the LHCb detector, where not always the same instantaneous luminosity is present. Therefore the measured signal at the SiPM needs to be normalized accordingly.
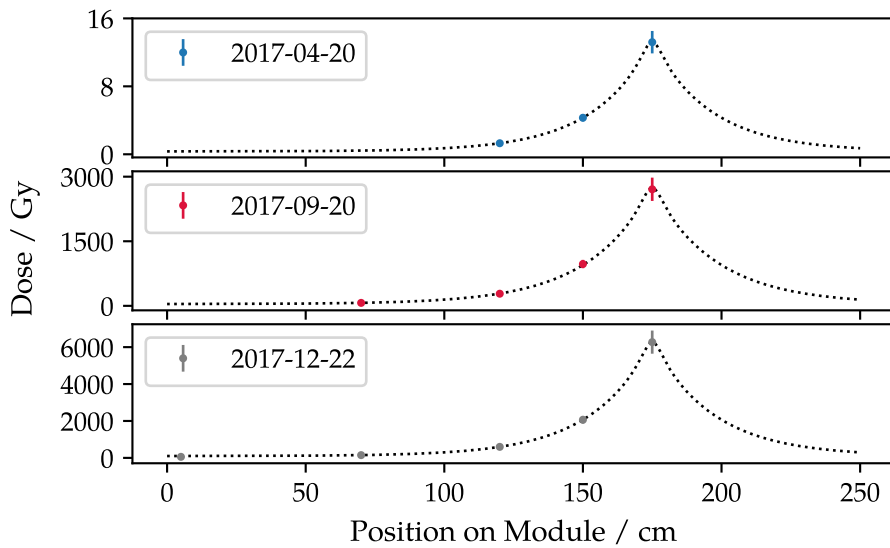
Fig. 6.27.: Measured doses at three different times. The dose distribution was fitted over the whole module length. The lowest plot shows the final applied dose and peaks at 175 cm with (6.3 ± 0.6) kGy. Not all dosimeters could be measured at all dates, or showed a measurable dose.
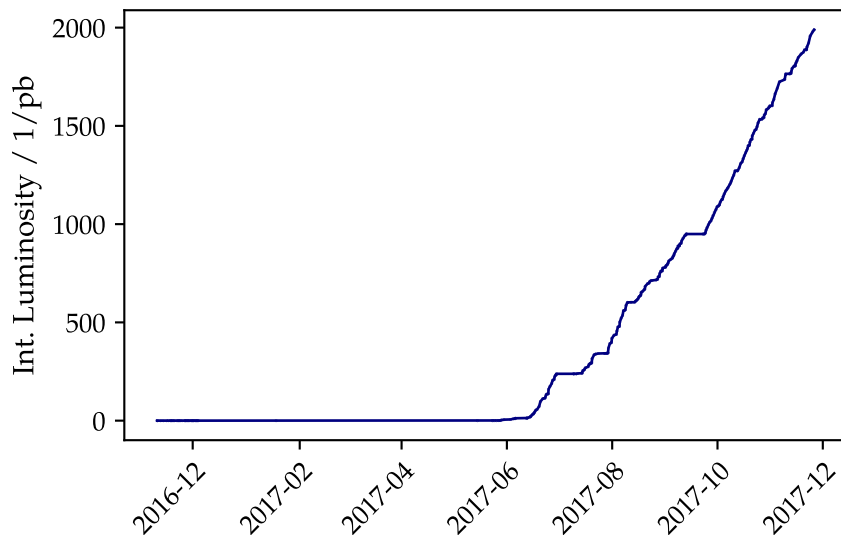

Fig. 6.28.: Integrated luminosity during the in situ irradiation inside the LHCb cavern. In total the applied dose corresponds to an integrated luminosity of 1989 pb^{-1}. At the beginning of the irradiation (end of 2016), only ion runs were performed, where not much luminosity had been collected, but the applied dose is clearly visible in Fig. 6.27.
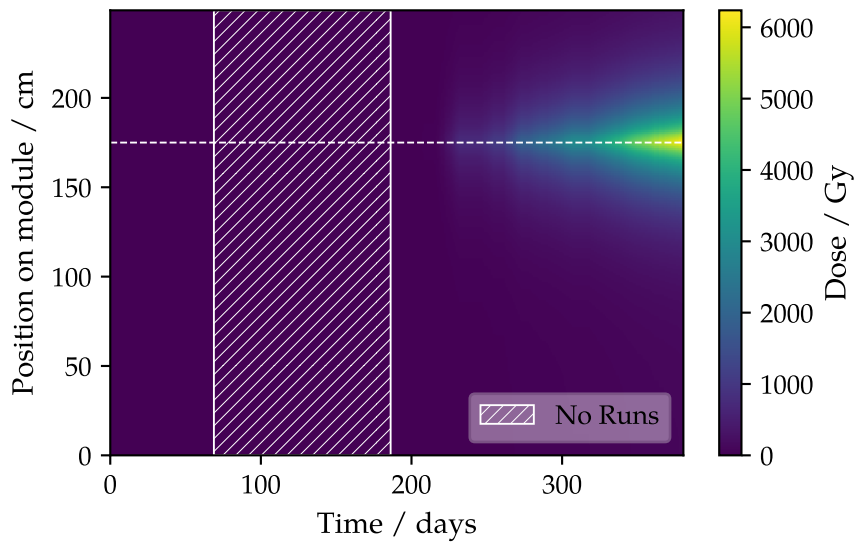
Fig. 6.29.: Applied dose as function of the time and module position. The most irradiated position at 175 cm is marked with a white dashed line. Also the time frame where the LHC was not operating is hatched.
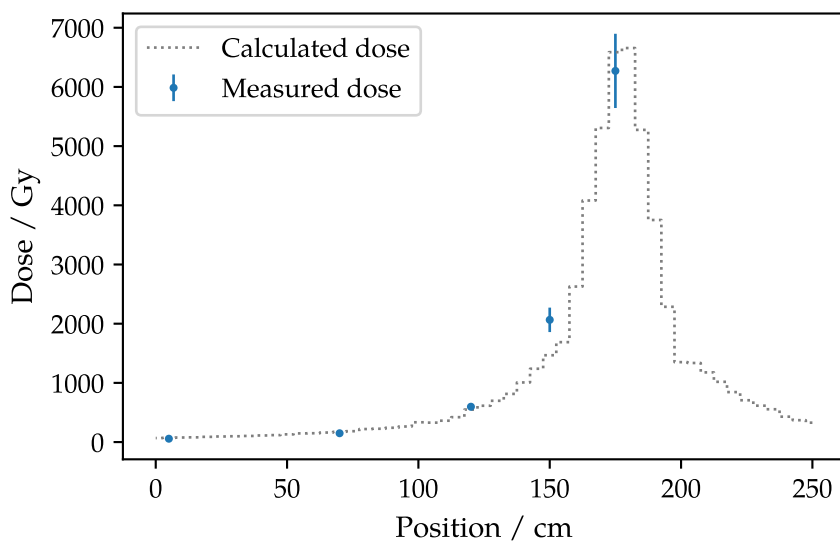
Fig. 6.30.: With FLUKA [71] simulated dose distribution after the collected integrated luminosity of 1989 pb^{-1} and the corresponding measured dose.
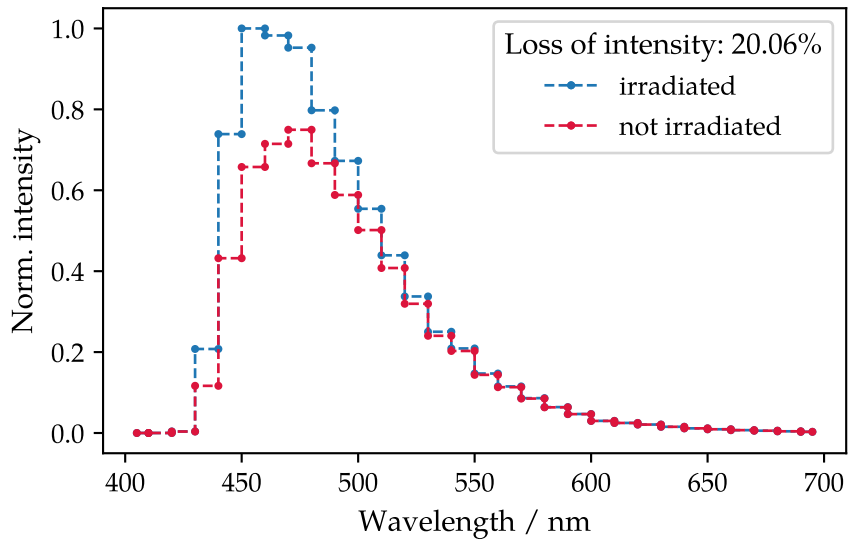
Fig. 6.31.: Signal at the SiPMs as a function of the wavelength for the irradiated and non-irradiated case. This signal loss due to irradiation has been determined taking a simple model, based on intrinsically and radiation induced attenuation, into account.
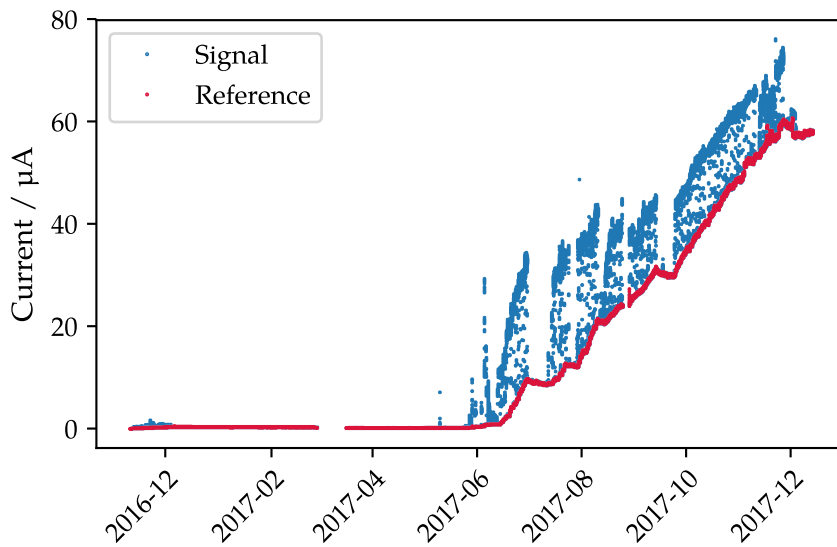
Fig. 6.32.: Recorded current at both SiPMs inside the LHCb cavern. The red curve shows the reference SiPM which only measures dark counts. A visible rise in dark current due to irradiation is visible. The blue trend corresponds to the SiPM connected to the fibre mat and measures its signal.

All data is split into these runs, so that a strong correlation between the cleaned up signal and the instantaneous luminosity is visible, see Fig. 6.33. In addition some deviations
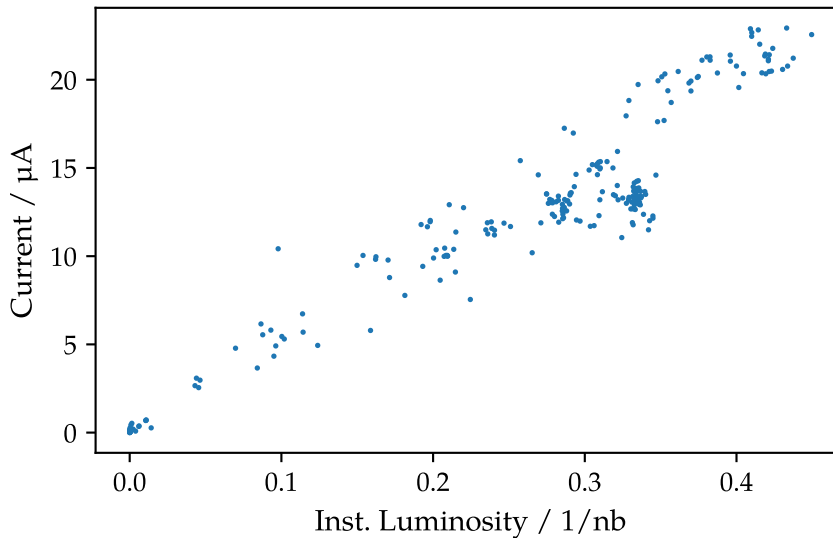
Fig. 6.33.: Measured signal of the fibre mat as a function of the predominating instantaneous luminosity. The current is already cleaned of dark counts. A strong correlation is visible, as more luminosity result in a higher measured current at the SiPM.

from a straight line are visible with refer to the radiation damage of the SiPMs, as the dark counts rise with irradiation.

The normalized signal as a function of the time is displayed in Fig. 6.34. During the ion runs a higher signal has been measured which means, that the excitation strength of the ions inside the fibre mat is stronger, than the one of the protons. As the most damage occurred during the proton runs, the signal trend of this time period as a function of time is shown in Fig. 6.35. In the beginning, a fast drop to kind of a baseline, which decrease is visible. The decrease of the normalized signal refer to the radiation damage of the fibre mat. In addition, annealing effects after longer stops of the LHC (technical stops, machine development, ...) have been observed. After a period with no collision inside the LHCb detector, the normalized signal is increased, but then it drops fast to the original baseline, when collisions take place. In total a decrease of the signal of 40% could be measured.

6.4.4. Attenuation measurements

An attenuation measurement of the fibre module before installation was planned, but could not be realised as the TS 3 was preferred in time. In total four narrow fibre mats have been produced under the same conditions and with fibres from the same spool. One of them was installed in the LHCb cavern, while three stayed at the institute as reference. These three fibre mats have been measured with the *xy*-table for their attenuation. In addition, a dedicated setup, introduced in Sec. 7.4, was used to measure the light yield. The light yield measurement prior to irradiation could not be performed, as the light yield test stand was not available yet.
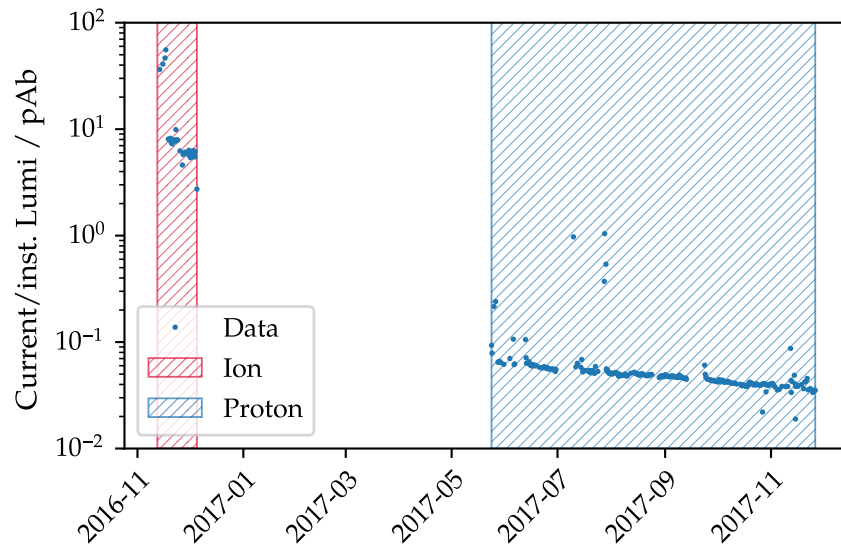
Fig. 6.34.: Normalized signal at the SiPM as a function of time. A clear decrease is visible. Times where ion runs were taking place are hatched red, while proton runs are hatched blue.
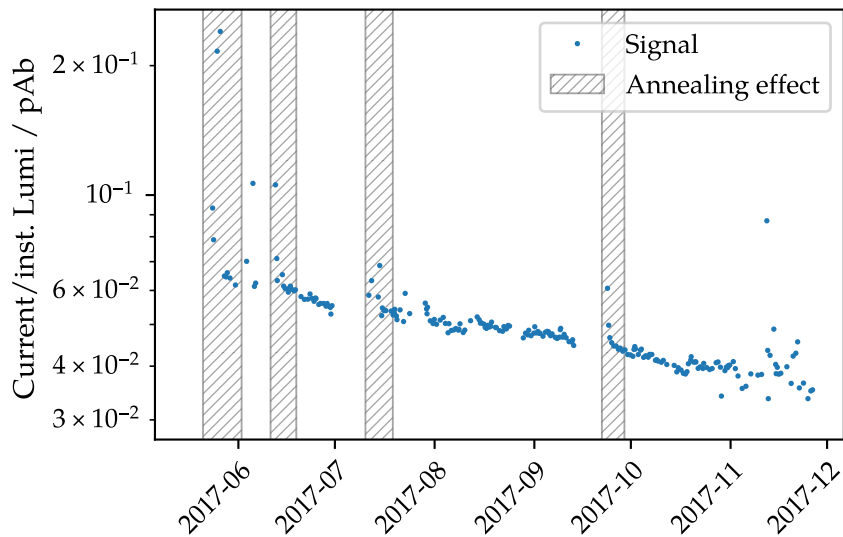

Fig. 6.35.: Normalized signal at the SiPM as a function of time, for the time frame, where only proton runs have taken place inside the LHCb detector. Annealing effects after time frames with no collisions inside LHCb are visible (hatched regions).
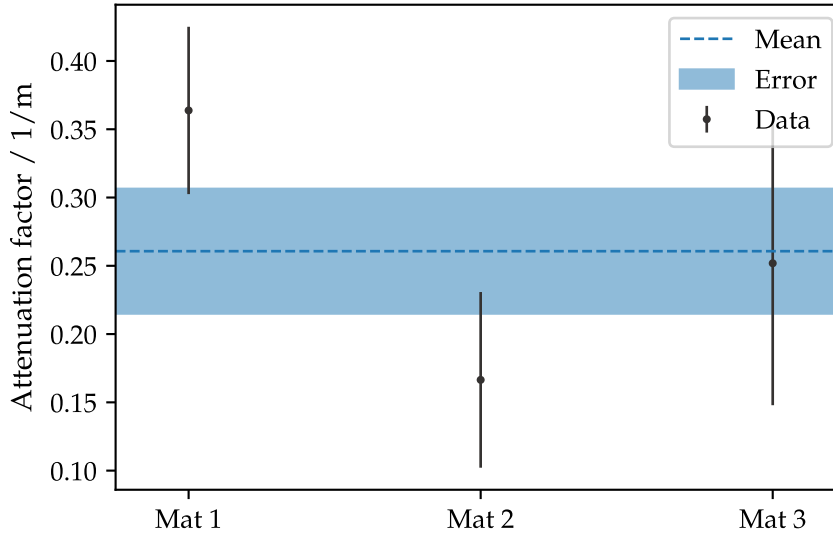
Fig. 6.36.: Measured attenuation factors for three reference mats. The average of the measurements is indicated with the blue dotted line and the standard deviation hatched blue.

The measured attenuation factors and their mean is shown in Fig. 6.36. The attenuation factor a_0 prior to irradiation has been determined to be

$$a_0 = (0.26 \pm 0.05)\,\text{m}^{-1}, \tag{6.11}$$

where the uncertainty represents the standard deviation of the three measured mats. The light yield measurement is displayed in Fig. 6.37. For the light yield measurement the three fibre mats have been excited with an ^{90}Sr in a distance of about 2.3 m and read out by SiPMs. All three mats were measured at the same time, with four SiPM arrays which have in total 512 channels. Only channels with fibres in front were taken into account (hatched regions in Fig. 6.37). Statistical uncertainties have been reduced by collecting a huge number of events. The mean light yield has been measured to be:

$$\text{LY}_{\text{ref}} = 10.23 \pm 0.48\text{p.e.,}$$

where the uncertainty represents the standard deviation of the light yield distribution of the three measured mats.

In December 2017 the in situ fibre module has been removed and measured in Dortmund. Due to the light tight wrapping of the fibre mat it was not possible to use UV-LEDs to measure the light output and the corresponding attenuation. Instead a ^{90}Sr source has been used to trigger the scintillation. Unfortunately the intensity of the corresponding light output is too low to get measured by the spectrometer. Therefore, a SiPM was used, and no wavelength dependency has been measured. The measured intensity trend is displayed in Fig. 6.38.

In the SciFi tracker simulation the radiation damage is by default calculated by the power law model Eq. (6.7), which is based on former irradiation campaigns. In order to compare this measurement with these previous irradiation campaigns, a single fibre simulation [63] has been used. The measured dose profile was fed into the simulation and the radiation induced attenuation simulated based on the linear Eq. (6.8) and power
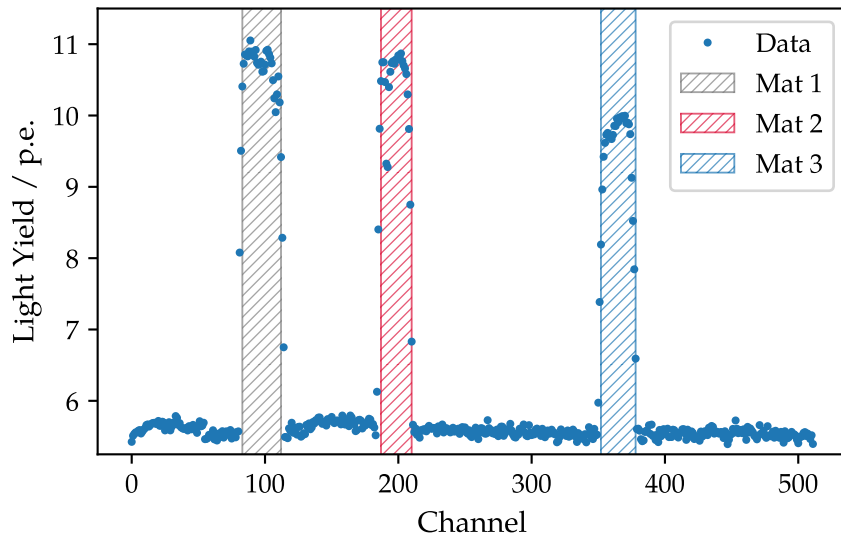
Fig. 6.37.: Measured light yields for three reference mats. The corresponding channel for each mat is indicated with the hatched region.
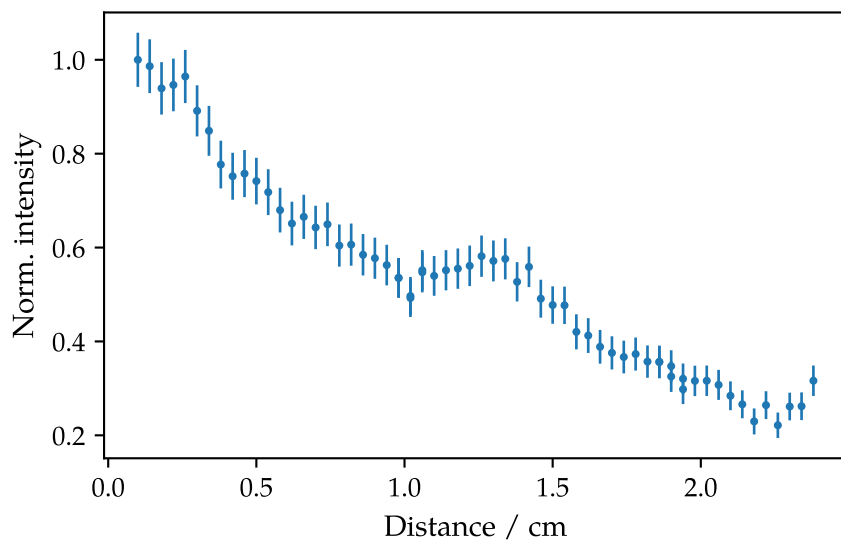

Fig. 6.38.: Measured intensity trend of the in situ irradiated fibre mat. The measurement was performed with a SiPM and a ^{90}Sr source.

law Eq. (6.7) model, respectively. In addition a non irradiated single fibre has been simulated. The simulated intensity trends are shown in Fig. 6.39. The two simulated
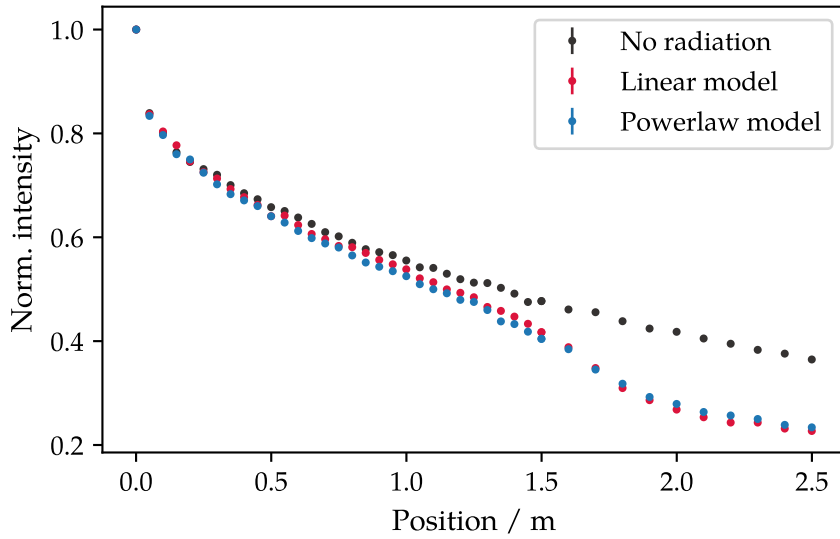

Fig. 6.39.: Simulation results for irradiated and non irradiated single fibres based on the measured dose profile. The radiation induced attenuation was determined with the linear and power law model.

models do not differ much, as the applied dose on the fibre module is in a range, where both models match each other.

The simulated intensity trend for the non irradiated fibre has been fitted with a single exponential function to the intensities ≥ 1 m, see Fig. 6.40. For the irradiated fibres the model in Eq. (6.6) has been used, where a_0 was fixed to be the value without irradiation. The dose has been integrated according to the given dose profile and was fed into the fit linearly and with a power of 0.8, respectively. The corresponding fits and intensity trends are shown in Fig. 6.41 and Fig. 6.42, respectively. The fits match the intensity trends very well. In addition the attenuation without irradiation is indicated, which vary significantly. The intensity loss I_{loss} for both models were determined to be

$$I_{\text{loss, sim, lin}} = 39 \pm 3\%,$$
$$I_{\text{loss, sim, pow}} = 37 \pm 3\%.$$

The fit results are listed in Tab. 6.2.

Figure 6.43 shows the comparison of the simulated and measured intensity trend of the in situ irradiated fibre module. For the intensities measured after around 1.3 m the trends are matching well. In addition the measured intensity trend has been fitted with the linear and power law model. The attenuation prior to irradiation a_0 has been obtained of the reference measurements (Eq. (6.11)). The attenuation fit based on a linear dependency on the dose is shown in Fig. 6.44 and for the power law model in Fig. 6.45. The results of both fits are listed in Tab. 6.2. In addition in both plots the attenuation prior to irradiation is indicated. The measured intensity trend varies clearly from the attenuation prior to irradiation. Nevertheless both fits show small deviations from the measured intensities around 1.2 m, where the intensity is rising. In addition the intensity
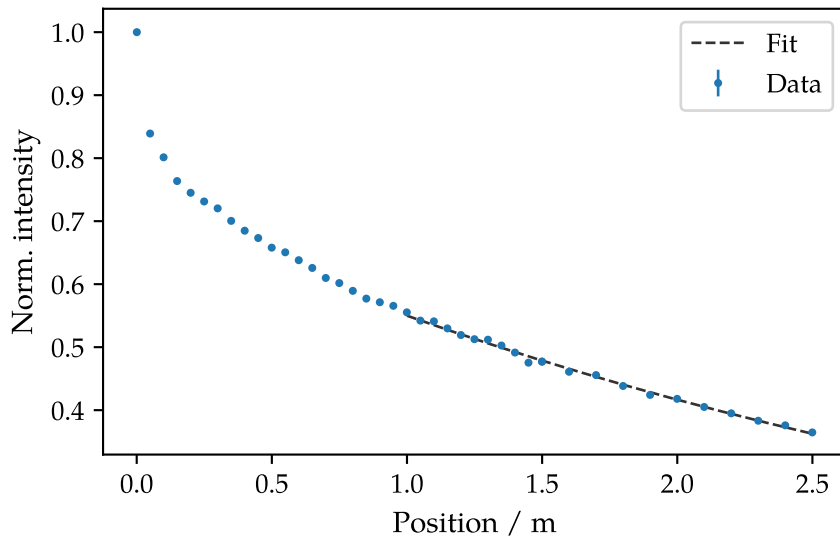
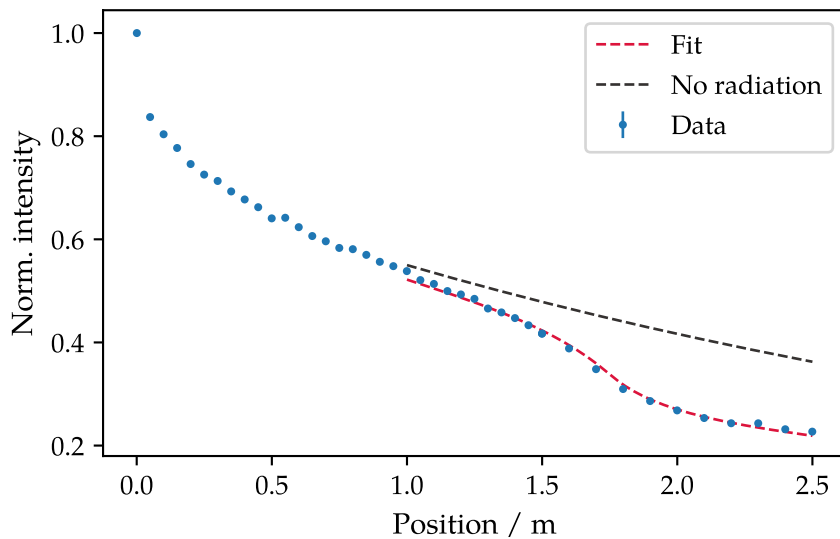Fig. 6.40.: Intensity trend and fit of the simulation output for a non irradiated single fibre.

Fig. 6.41.: Intensity trend and fit of the simulation output for an irradiated single fibre. The radiation induced attenuation was determined by the linear model.
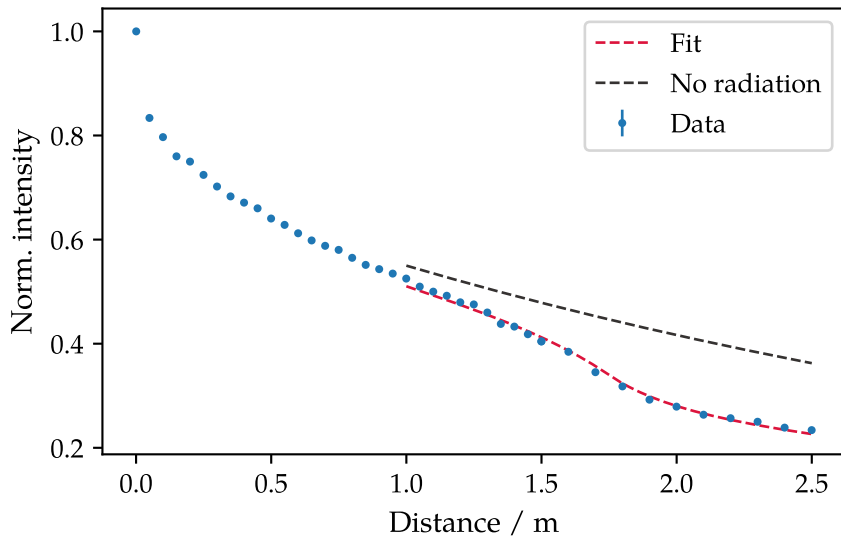
Fig. 6.42.: Intensity trend and fit of the simulation output for an irradiated single fibre. The radiation induced attenuation was determined by the power law model.
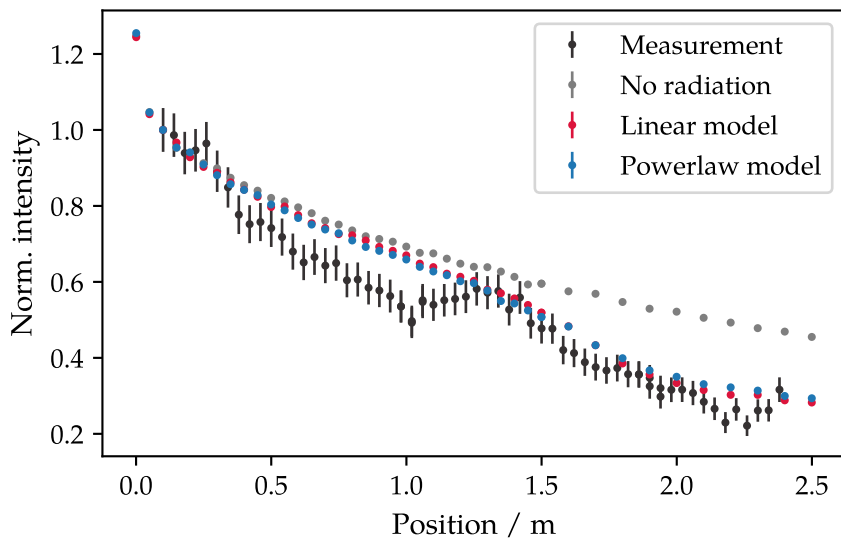

Fig. 6.43.: Intensity trends for the simulation outputs and the measurement of the irradiated module.
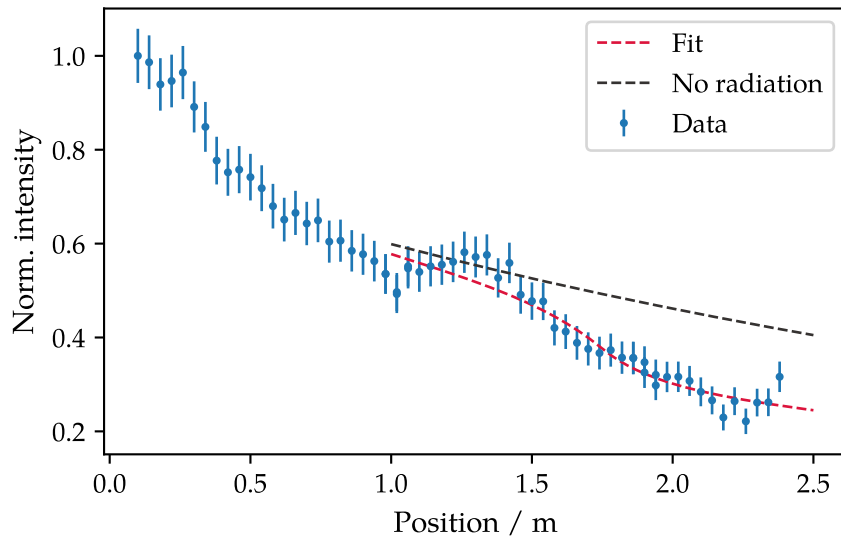
Fig. 6.44.: Attenuation fit to the measured intensity based on the linear model for the radiation induced attenuation.
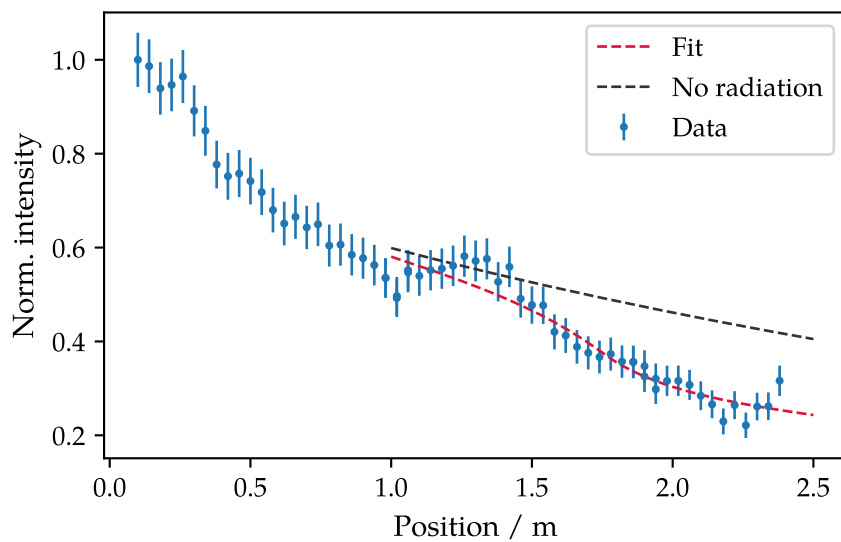

Fig. 6.45.: Attenuation fit to the measured intensity based on the power law model for the radiation induced attenuation.

Tab. 6.2.: Simulated and measured results for the attenuation factors for the in situ irradiated fibre module.

	Simulation	Measurement
a_0 / m^{-1}	0.28 ± 0.10	0.26 ± 0.05
$a_{D,lin}$ / kGy^{-1} m^{-1}	0.16 ± 0.05	0.16 ± 0.01
$a_{D,pow}$ / kGy^{-1} m^{-1}	0.68 ± 0.04	0.82 ± 0.05

loss due to irradiation can be measured to be

$$I_{\text{loss, lin}} = 39 \pm 5\%,$$
$$I_{\text{loss, pow}} = 39 \pm 4\%.$$

However, the obtained attenuation factors for the radiation induced attenuation do match the ones obtained from simulation. As already seen in the simulation results it is not possible to see a big difference either using the linear or the power law model for the radiation induced attenuation. Also the fit to the measured data, does not confirm one model while rejecting the other one. But the measured radiation induced attenuation factor for the linear model fully agree with the simulated factor, as for the power law model factor a small discrepancy is visible.

In addition a light yield measurement after the irradiation has been performed. The measurement have done with the same setup, as for the reference mats. The result is shown in Fig. 6.46 and the light yield was measured to be

$$LY_{\text{irrad}} = 8.99 \pm 0.10 \text{p.e.}.$$

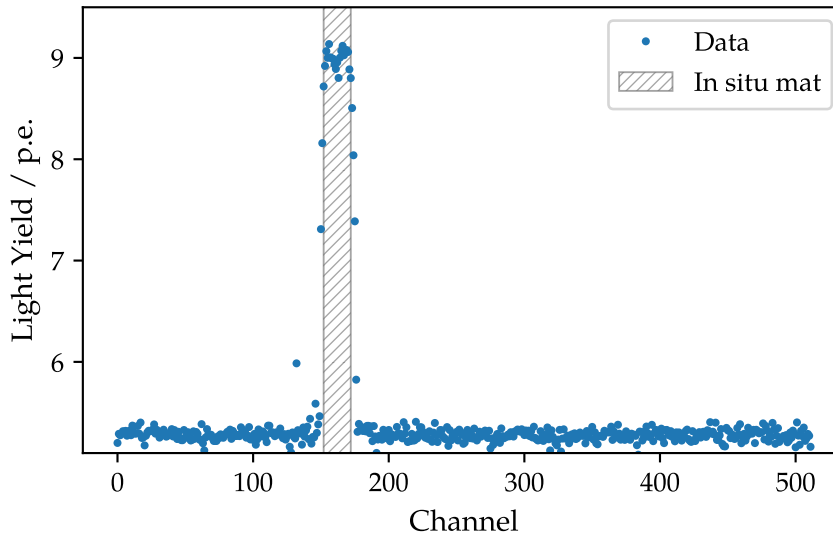With this a degradation of the light yield of

Fig. 6.46.: Measured light yield for the irradiated in situ fibre mat. The corresponding SiPM channels are indicated with the hatched region.

Tab. 6.3.: Simulated and measured results for the intensity losses for the in situ irradiated fibre mat.

	Simulation	Measurement
$I_{\text{loss, lin}}$ / %	39 ± 3	39 ± 5
$I_{\text{loss, pow}}$ / %	37 ± 3	39 ± 4
SiPM signal loss / %	-	40
Mean light yield loss / %	35/40	12 ± 4

$$LY_{\text{loss}} = 12 \pm 4\%$$

can be determined.

The single fibre simulation [63] is used to produce maps which give the expected main light yield loss for different positions of the SciFi Tracker [41]. With these maps a mean light yield loss of about 35% [41] after $50\,\text{fb}^{-1}$ (upgrade conditions) was determined, using the power law model. This number was determined for the worst case fibre, which means the fibre closest to the beam pipe, and at an excitation close to the beam pipe (most irradiated region). Using the linear model results in an additional 11.6% [41] less light, meaning a mean light loss of about 40%. To compare these results to the in situ irradiation, the dose profiles are shown in Fig. 6.47. The dose profiles are different, and
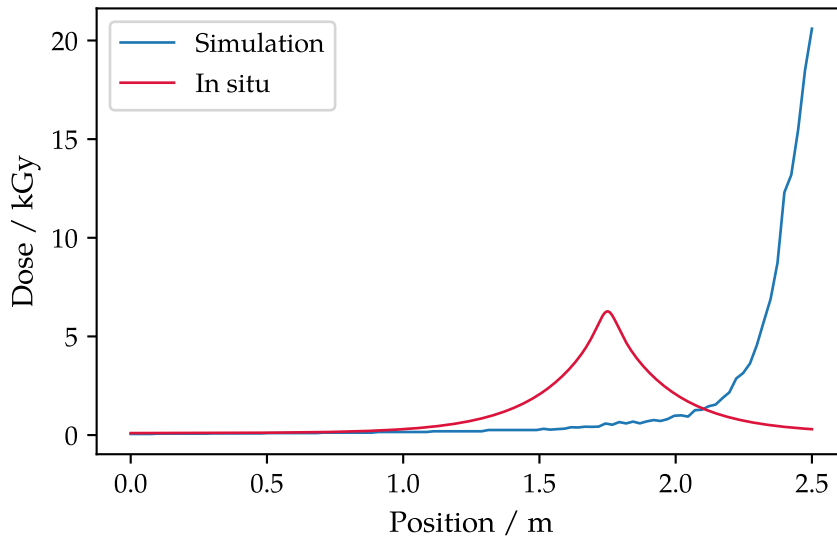

Fig. 6.47.: Dose profile of in situ fibre mat in comparison with the dose profile of the worst case fibre in the SciFi Tracker after an irradiation of $50\,\text{fb}^{-1}$.

the simulated dose profile peaks at higher doses, but it decreases much steeper than the in situ dose profile. The mean dose of the in situ irradiated fibre mat was determined to be $(1.7 \pm 0.2)\,\text{kGy}$ and for the worst case fibre $(1.4 \pm 0.3)\,\text{kGy}$ for a length of 2.5 m, which are compatible within their uncertainties. The determined signal losses from different sources (measurements / simulations) are listed in Tab. 6.3. The numbers are comparable within their errors, which means the measured signal and light losses match the ones obtained from simulations. As these simulations are based on results from

former irradiation campaigns this in situ campaign confirms previous results. In addition the SiPM signal loss prior to irradiation was determined to be 20% (Fig. 6.31), which is much smaller than the measured signal loss. However, only simple assumptions have been made and therefore have the potential for systematic errors. Unfortunately the loss in light yield does not match the other observations. The deviation can be explained with the missing reference measurement prior to irradiation. Further studies will be done but could not be realised in the scope of this thesis. Nevertheless the fibre mat still shows a high light yield (without mirror) after irradiation.

6.5. Summary & outlook

A key parameter for the performance of the LHCb SciFi Tracker is the number of photons detected by the SiPMs, the light yield. The initial number of photons created in the fibre is attenuated along the fibre. This attenuation is a combination of several effects like scattering, absorption and losses at the boundaries. The measured attenuation is dependent on the wavelength and angle of the photons as well as on the used read out electronics. Different studies on the attenuation of scintillating fibres have been presented in this thesis.

In the region close to the beam pipe most tracks pass the detector. This implies the highest dose level and therefore the highest radiation damage. For the worst case fibre the dose reaches 20 kGy but drops quickly with increasing distance to the beam pipe, which refers to (1.4 ± 0.3) kGy in average. This results in a mean light yield loss of 35% prior to irradiation. As these numbers were obtained from simulations based on former irradiation campaigns an in situ irradiation campaign has been performed resulting in a similar average dose of (1.7 ± 0.2) kGy after irradiation. The signal of the irradiated fibre mat was monitored over time and showed a decrease of 40%. In addition attenuation measurements performed on the irradiated fibre mat showed an intensity loss of (39 ± 4)%. In summary the performed in situ irradiation campaign fully agrees with the simulation results and therefore prior irradiation campaigns.

The presented studies of angular dependency of the attenuation length are limited by statistics and have the potential for systematic errors. Currently a more enhanced setup is built to reduce these uncertainties and by using an automatic angle adjustment a finer grained binning of the angles with higher accuracy is possible.

7. Quality assurance for the serial production of fibre mats

For the LHCb SciFi Tracker more than 1000 fibre mats at four different Winding Centres have to be produced. Providing all different production sites with the same equipment and common procedures for each production step, allows to produce appropriate mats at all institutes. Nevertheless reliable and standardised quality assurance procedures along the production line of the fibre mats are required. In addition, quality measurement methods and a mark assignment is necessary to determine the mat quality.

During this thesis, quality assurance procedures and quality measurement methods have been developed and were included in the serial production. Also all quality determining test stands have been set up for the Dortmund serial production as well as taking care of the results. In the following, the quality assurance procedures are described and studies concerning the quality of the scintillating fibre mats are presented.

7.1. Winding Control - Classification using automated image recognition

The most critical part during the winding procedure is the fibre positioning of the scintillating fibre. Before the start of the serial production, bumps on the fibre spools had not been removed. And the knowing that they appeared quite often, lead to a necessary attention to the winding procedure. These bumps, dirt, an excess of glue or vibrations of the fibre could effect the fibre positioning on the wheel. In addition, the axis of the winding wheel can not be machined to be 100% accurate, which leads to a small movement in direction of the radius of the wheel (radial wobbling) and secondly in the direction of the axis (transversal wobbling). As the radial movement does not influence the positioning of the fibres it can be neglected and it is usually much smaller than the transversal movement. The transversal wobbling can be in the order of 100 µm and does indeed affect the positioning of the fibres with a transversal pitch of 250 µm. The effect of such winding errors are displayed in Fig. 7.1. In case of a smooth winding, the fibre positioned correctly with the help of the guiding grooves, either provided by the winding wheel or the fibre layer below (see Fig. 7.1(a)). If the positioning of the fibre is manipulated, it can either jump to the next groove (see Fig. 7.1(b)) or also to a higher layer, like shown in Fig. 7.1(c). It is very important to detect winding defects as quickly as possible, to allow a correction. For this, the winding is stopped, the fibre manually wound back until the positioning is correct and checked what introduced the fibre jump. Afterwards, the winding is continued normally. Due to the transparency of the fibres and the inhomogeneity of the glue, it is difficult to judge by eye if the fibre positioning is done correctly or not. During the R&D phase of the fibre mat winding, it was found that looking to the horizon of the mat, tangential to the wheel, gives the best possibility to monitor the winding procedure. In the beginning, it was just done with the help of a standard consumer digital camera by using its live view modus and a monitor. The
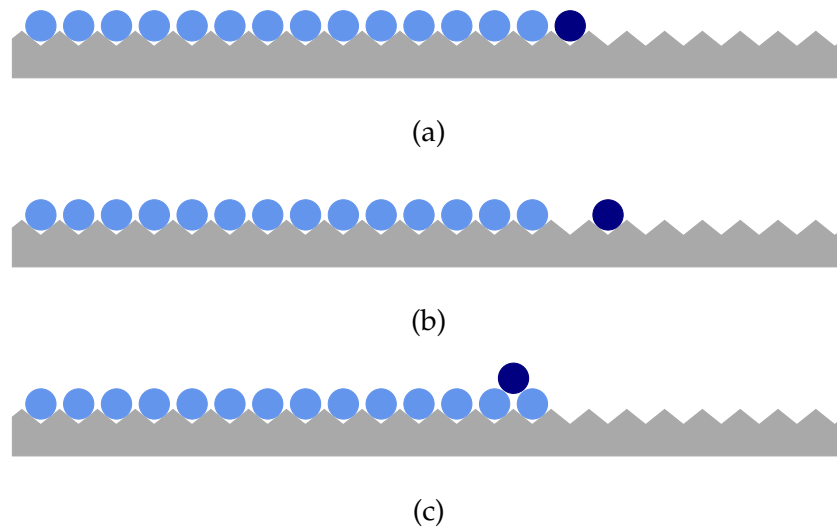
(a)

(b)

(c)

Fig. 7.1.: Pattern on the winding wheel during winding of the first layer. Different types of errors can occur. The actual wound fibre is indicated in dark blue. (a) Winding is running smoothly. (b) Scintillating fibre jumped to an advanced groove. (c) Scintillating fibre jumped to a higher layer.

large aperture of the lens leads to the effect that the fibres can be seen as circles, like illustrated in Fig. 7.1. In this phase, the camera was not mounted on the linear slide of the last guiding spool, but placed in front of the winding wheel and needed to be placed by hand along the fibre mat width during the winding of a layer. Beforehand, no monitoring method of the winding procedure itself was used, so that it was not unusual that fibre layers contained errors like missing or crossed fibres. With the introduction of this method the quality of the mat winding increased immensely.

During this thesis a more robust and convenient solution has been developed. For this purpose an industrial camera was mounted directly on the linear slide of the serial production winding machine, see Fig. 7.2 and also Fig. 5.3 on page 37. As the production of a fibre mat requires a lot of different production steps, it is not practical to watch the monitor during the whole winding time of around 2.5 h. For this reason, an automatic error detection has been developed within this thesis using the video input from the industrial camera.

7.1.1. Setup

For the setup, a monochromatic industrial camera[1] with a resolution of 1600×1200 pixel was used. The chosen lens has a magnification of 1.6 with a working distance of 36 cm. It has a changeable aperture but a fixed focus with a small depth of sharpness, which requires a precise mounting and alignment. A reliable mounting on the serial production winding machine has been achieved by the use of a special camera mounting and the use of a camera macro slide (see Fig. 7.3(a)). Though the winding room is a bright room, additional exposure for a good camera feed is required. For this purpose, a simple so-called softbox has been built, see Fig. 7.3(b). It diffuses the light into a soft, even light,
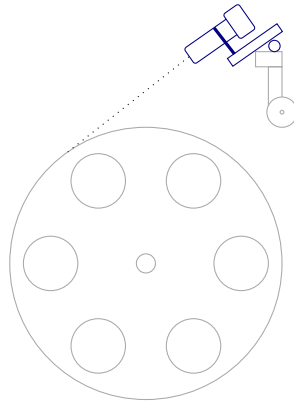
---

[1]Matrix Vision mvBlueFox3

Fig. 7.2.: Camera mounted on the linear slide of the winding machine. It is mounted in such a way that it looks at the horizon of the mat, tangential to the wheel. With this type of mounting, the camera is moving along the mat width and the large aperture leads to the effect that the fibres appear as circles.
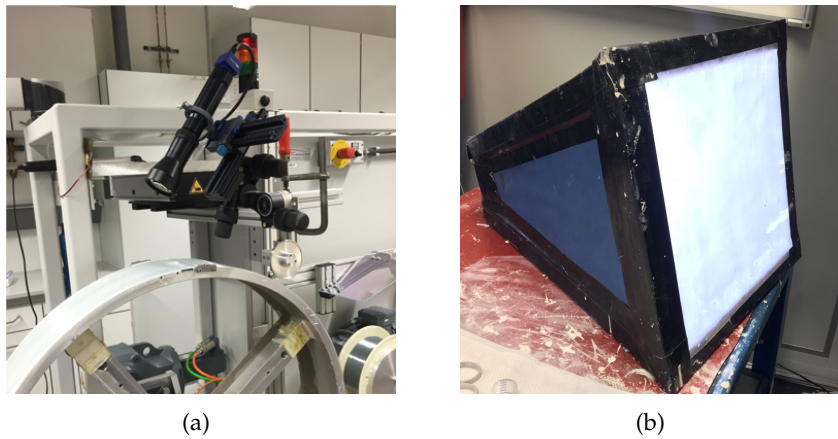

| (a) | (b) |

Fig. 7.3.: (a) Camera mounting on the serial production machine, realised with the help of a special camera mounting and several macro slides. (b) Softbox, which diffuses the light to get a reliable exposure and good camera feed.

which works well for this application. The industrial camera provides an output which is connected directly to the serial production machine and either triggers an alarm or stops the machine if a winding error occurs.

7.1.2. First approaches and challenges

Several approaches have been followed to realise a reliable monitoring of the fibre mat winding procedure. The first idea using a pattern recognition software and fitting circles to the camera feed is shown in Fig. 7.4(a). Circles are fit to each fibre in the camera feed and the position of the actual wound fibre is determined. If the pitch of the newest fibre differs from the nominal one an error has occurred and the winding machine should stop. However, this approach resulted in a huge overhead and was too time- and CPU-consuming as well as too sensitive to the exposure situation.
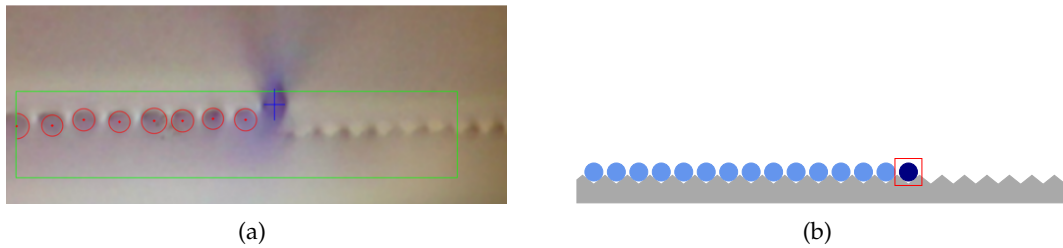
<center>(a)</center> <center>(b)</center>

Fig. 7.4.: Different approaches have been followed to allow a reliable monitoring of the fibre winding. (a) With the help of a pattern recognition the pitch between the fibres are determined. (b) Tracking the first fibre of the wound layer to detect possible deviations from the nominal position.

For a correct positioning of the fibre, it is sufficient to know where the actual wound fibre is positioned with respect to the one wound previously. For this a second method, a tracking approach has been followed. After finding the first fibre, either by manually determine it or by pattern recognition, the position of this fibre is tracked. By applying a certain threshold illustrated as the red box in Fig. 7.4(b), it can be determined if the fibre moved out of its particular position, either because it jumped to the next groove or to a higher layer. Tracking of the fibre requires a precise positioning of the fibre on the camera feed. However, the position of the fibre is a bit unstable, due to the movement of the camera and due to the wobbling of the winding wheel. This fact leads to a non-constant position of the fibre on the camera image. A solution can be to apply the same kind of movement to the threshold box, but due to the mandatory change of the winding wheels during the serial production every day, it would require to determine the wobbling after every exchange. Another solution has been followed to apply a video stabilisation to the camera feed. Different algorithms are available, but was not feasible in real time.

7.1.3. Classification with Convolutional Neural Networks

As shown in the previous section, a reliable approach for an automated winding control should not be based on either the machine or environment conditions. Technically during the winding procedure two types of images can appear. Either everything works correctly and the fibre positioning is good (see Fig. 7.1(a)) or the fibre positioning is manipulated and one of the errors shown in Fig. 7.1 is created. The possibility to divide the images into two groups (positive / negative) allows for a machine learning approach in combination with image recognition. Convolutional Neural Networks (CNN) [73] have been established as a powerful class of models for these type of problems. In addition, one benefit of this approach is the independence of the wheel wobbling and possible deviations between different wheels as only single frames are used for the classification.

Convolutional Neural Networks

The winding control problem is an image classification problem, where the task is to assign an input image to one label from a fixed set of categories. Convolutional Neural Networks (CNNs) are a specialised type of ordinary Neural Networks, an example of machine learning algorithms. Inspired by the biological neural network they are made up of neurons and have learnable weights and biases, such that they can learn tasks by considering examples, without task-specific programming and any a priori knowledge.

A neural network can be trained and improves with every new example it gets. However, the larger the neural network, the more training samples it requires to perform well. Neural Networks receive an input (*e.g.* a single vector) and transform it through a series of so-called hidden layers. Each hidden layer consists of a set of neurons, where each neuron is fully connected to all neurons in the previous layer. Neurons of a single layer function are completely independent and do not share any connections. The last fully connected layer serves as output layer and in classification settings it represents the class scores. A coloured image, 150 pixels wide and 200 pixels tall, would consist of $150 \times 200 \times 3 = 90\,000$ numbers, where each number is an integer in the range from 0 (black) to 255 (red/green/blue). The task of the neural net is to turn this huge amount of numbers into a single label. Architectures based on convolutional layers make the explicit assumption that the inputs are images such that the neurons are arranged in activation volumes with three dimensions (width, height, depth). Neurons of one layer will only be connected to a small region of the previous layer instead of all of the neurons in a fully connected manner. This approach constrains the architecture in a more sensible way as a fully connected structure is clearly wasteful and the huge number of parameters quickly lead to overfitting[2]. An example of an architecture based on convolutional layers is shown in Fig. 7.5. Alternating convolutional and pooling[3] layers decrease the input size and establish feature maps, which then are transferred to fully connected layers to ensure a proper classification. The output is represented by a single number giving the probability that the input belongs to the specific class.
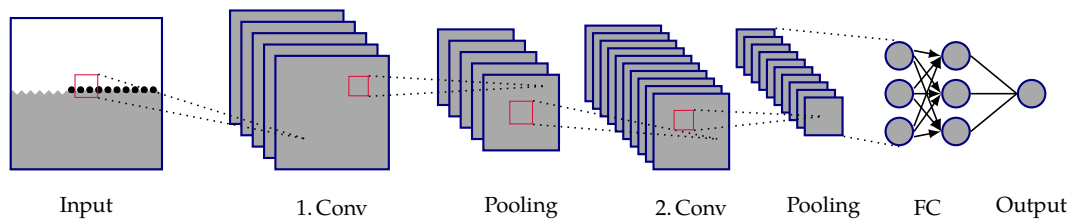

Fig. 7.5.: Example architecture for a CNN trained on image recognition. Two convolutional layers stacked with pooling layers to decrease the resolution are fed into fully connected layers producing the output probability for one class.

Training Data Set

The images of the camera can be separated into two classes - positive, where the fibre positioning is correct and negative, where an error occurred. Thus it is not necessary to know which kind of error happened (Fig. 7.1(b) or (c)); a binary description of the problem is sufficient. The output of the trained neural network gives the probability that the input image belongs to the class of positive (without error) images. This means the output should be

$$1, \text{if input is positive and}$$
$$0, \text{if input is negative.}$$

---

[2]Model fit to closely or exact the given data, but fail to fit additional data

[3]Its function is to progressively reduce the spatial size of the representation to reduce the amount of parameters and computation in the network, and hence to also control overfitting.

Since the task of identifying an error in the winding pattern is relatively trivial for a human to perform, there are a list of challenges involved from the perspective of a Computer Vision algorithm. The main challenges this neural network has to deal with are different exposure conditions (see Fig. 7.6) and a slightly different position of the main structure on the image itself (see Fig. 7.7). All these features need to be covered
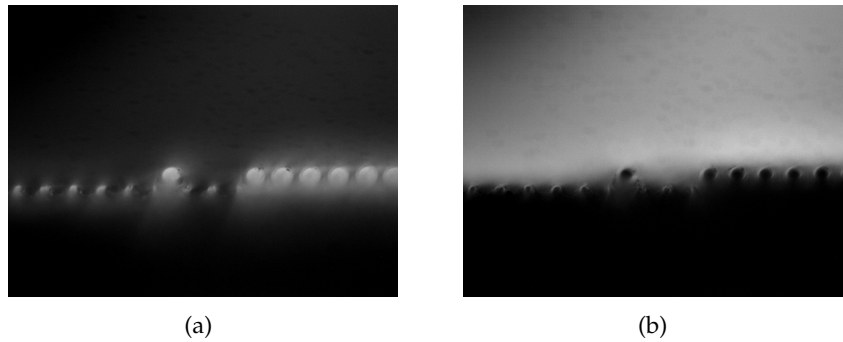

(a)	(b)

Fig. 7.6.: The same winding pattern under different light conditions. (a) The light source shines onto the fibres such that they appear bright on the camera frame, while in (b) the light source directly shines into the camera and the fibres appear as a dark shadow.

(a)	(b)
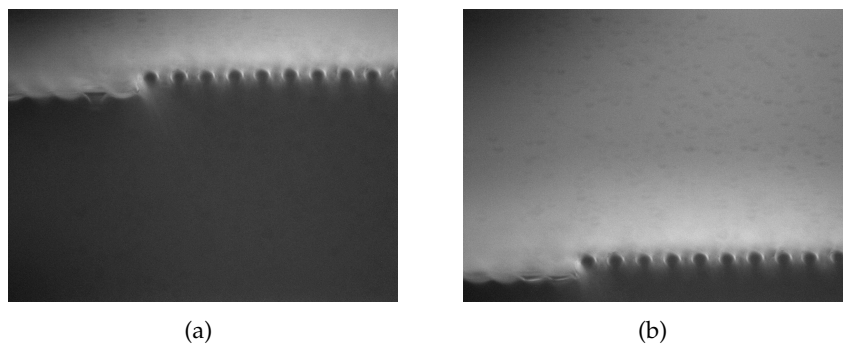
Fig. 7.7.: Depending, on the angle of the camera with respect to the winding wheel and the linear stage, different positions of the interesting pattern on the image can appear.

by the training data set. For this purpose, about 40 000 labelled images were recorded - 20 000 positive and 20 000 negative ones. The dimensions of the images were taken into account and it was found, that a resolution of 75×100 pixels is sufficient to guarantee the recognition of the important features. In addition, the training time and later on the classification time is minimized as the number of calculations directly scales with the amount of pixels. As the camera only provides monochromatic images, it is not necessary to take colour information into account, however, the training would not benefit from these information, as the fibres are transparent.

Architecture of trained CNN

As described previously, a simple CNN is a sequence of layers, where every layer transforms one volume of activations to another through a differential function. The CNN used here uses three main types of layers to build the architecture: Convolutional Layers, Pooling Layers and Fully Connected Layers. In principle, the architecture shown in

Fig. 7.5 is used, but different types of architectures have been studied. The best performance in the lab showed the one which consists of three stacked layers of convolutional and pooling layers, which are fed into two hidden fully connected layers. The kernel size decreases between consecutive convolutional layer. Overfitting is avoided by applying a dropout technique, where randomly units from the neural network are dropped. This prevents neurons from co-adapting. After normalising the previously described training data set, the training was performed for 100 epochs, where an epoch is one complete presentation of the data set to be learned to the CNN.

Performance of trained CNN

In Fig. 7.8, accuracy and loss during the training are shown. Accuracy is the statistical measure of how well the binary classification test correctly identifies the class. The accuracy is defined as the proportion of true results (both true positives and true negatives) among the total number of cases examined. The true positive rate is known as probability of detection and the false positive rate can be described as probability of a false alarm. As the training procedure is a minimizing procedure, the loss represents the price paid for inaccuracy of predictions and should decrease with training time. One can clearly see, that the accuracy of the neural network increases with the training time, while the loss is decreasing constantly.
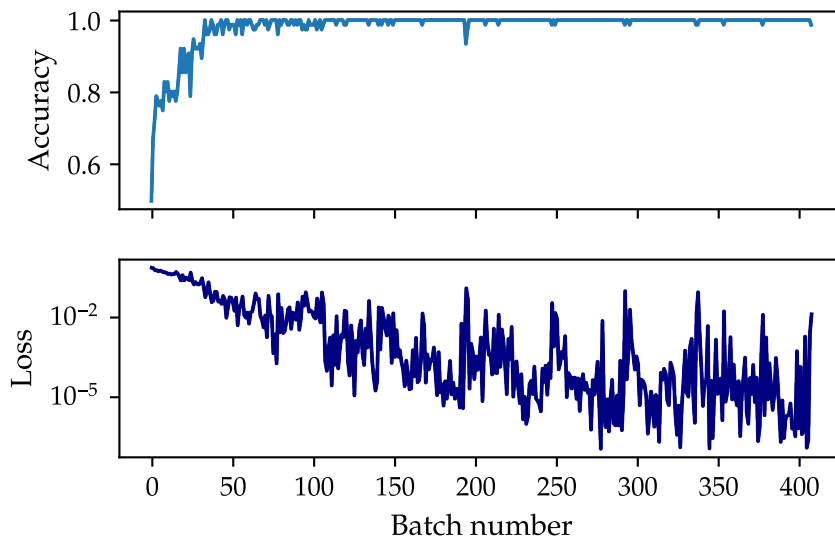

Fig. 7.8.: Accuracy and loss evaluation during the training of the neural network. The accuracy is growing, while the loss is constantly decreasing and then saturating.

After the neural network has been trained, some cross checks on the performance have been done. First, a set of 1000 test images has been produced and the scores for each have been determined. The trained network showed an accuracy of 99.99%. A histogram of the score distribution is shown in Fig. 7.9. Scores for positive and negative images are shown. If the threshold to separate the two classes is set to 0.5, which means scores below 0.5 are rated negative and above 0.5 are classified to be positive, only two negative images have been classified to be a positive one. None of the positive images are rated as negative ones, but their score is spreading from 1 to 0.85. A possibility for a better
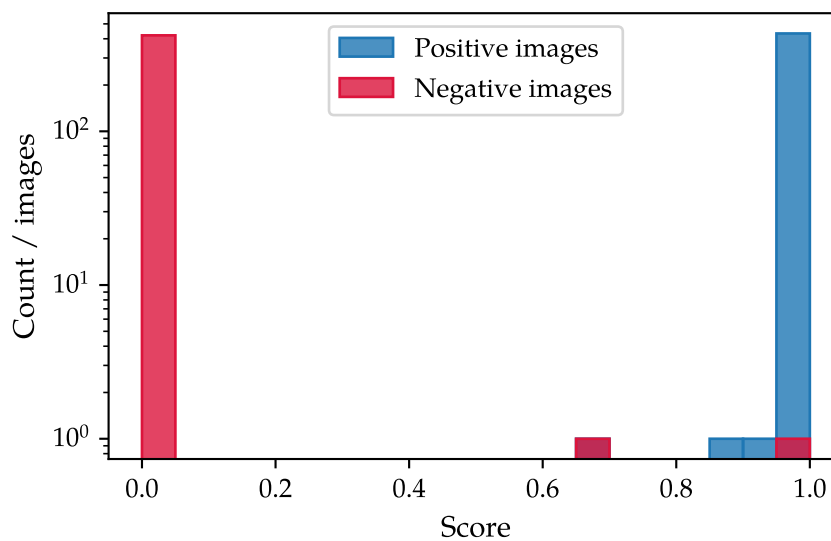
Fig. 7.9.: Score distribution for 1000 tested images. Just two negative images have been classified incorrectly (assuming a threshold at 0.5). The probability for positive images are spread from 0.85 to 1.

separation of the two classes may be achieved by raising the threshold, but here another solution has been followed. As the trained network cannot be 100% correct and therefore false alarms may appear from time to time, another requirement has to be fulfilled to trigger an occurred winding error: a sequence of 5 images need to be classified negative.

Another possibility to look at the probabilities of the tested images are receiver operating characteristic (ROC) curves [74, 75]. In a ROC curve, the true positive rate is plotted against the false positive rate. The area under the ROC curve (AUC) represents a benchmark how well the network with its parameters can distinguish between the two classes and should be close to untiy. In Fig. 7.10, the ROC curve for the used neural network is displayed. The AUC parameter can be determined to be 0.9999, which shows the good performance of the trained neural net.

Furthermore, timing studies have been performed to see if the trained network and the whole method itself fulfil the requirement of a fast and reliable winding error detection method. Four different images have been chosen for a timing study. This set contains two positive and two negative winding images. The two images of each group just differ in their exposure - one image shows dark fibres, one bright ones (see Fig. 7.6). The measurement has been performed on the PC used during the winding. The numbers shown in Fig. 7.11 represent the required time without any parallel programs running on the PC. The slowest measured time is (9.2 ± 0.2) ms, which means it is still possible to run the camera feed at 108 fps (Frames per second). As the used camera provides just 20 fps, which is totally satisfying, this method fulfils the requirement of being fast.

The live performance during the winding of a fibre mat has been tested. First the score output of the trained network has been tested on a static image. For this test, the winding wheel had been stopped and the scores for a positive and a negative image have been recorded. The resulting histogram is shown in Fig. 7.12. For both image types, a sharp distribution is visible which correlates with a high reproducibility of the neural
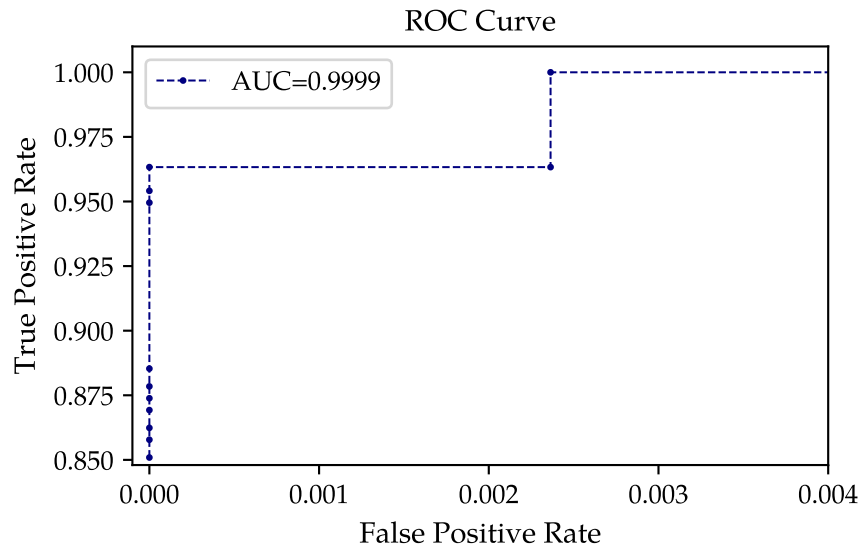
Fig. 7.10.: Receiver operating characteristic (ROC) curve for the trained neural network. The area under the curve (AUC) is with 0.9999 close to unity.
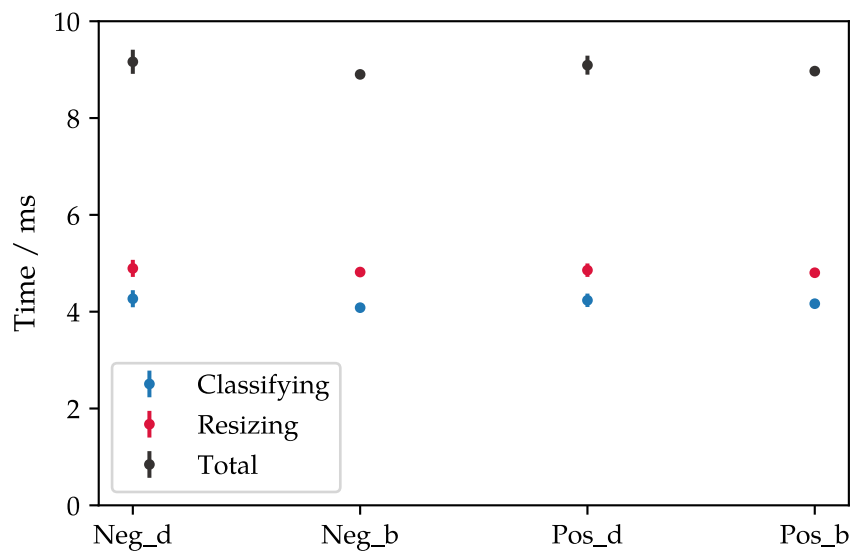

Fig. 7.11.: Timing analysis performed with the trained network on the computer used in the winding lab. The shown times where measured without any parallel programs running on the PC. Neg_d/b: negative image with dark/bright fibres. Pos_d/b: positive image with dark/bright fibres.

net. Thus, the same measurement has been performed during winding of a fibre mat.
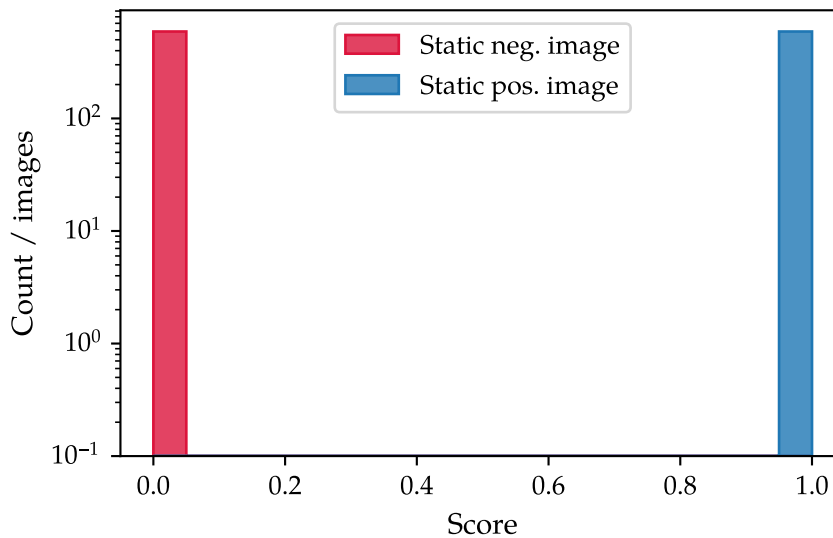
Fig. 7.12.: Live score output of the net for a static image (positive and negative). The sharp distribution show a high reproducibility of the classification procedure.

The score histogram resulting on only positive images can be found in Fig. 7.13. The distribution shows scores from 0.6 to 1, however the threshold for a negative image is below 0.5. The mean of the distribution can be determined to be 1.00 ± 0.02.

7.1.4. Application in the laboratory

This quality assurance application needs to be implemented in the winding lab at the winding machine. The winding procedure itself is mostly done by students and technicians. Hence, it is necessary, that the application provides an easy handling without further knowledge. First of all the application needs to provide a camera feed, which can be seen by the winding operator. In addition the images of the camera feed shall be classified and winding errors recognized on a fast and reliable basis. Also a connection to the winding machine is desirable to stop the winding automatically and fast, if an error occurs. The application has been implemented within a graphical user interface (GUI) and allows an easy usability. A screen shot of the GUI is given in Fig. 7.14. The feed of the camera is shown and depending on the classification of the current image the coloured rectangle around the image appears green (everything is fine) or red (winding error was detected). Furthermore camera settings, like exposure time, gain, black level or frame rate can be accessed and the classification can be started and stopped. Moreover for testing purposes and performance studies the single images or the whole camera feed can be saved and different trained networks loaded. Also the probability output of the network can be saved to file. A special debug window can be opened to see the output of the network over time and the probabilities filled into a histogram.

The application is used in the winding lab with success and the performance of the trained network is reliable. Though the performance is dependent on the exposure conditions and camera settings, the network was trained in a way, that it is working in
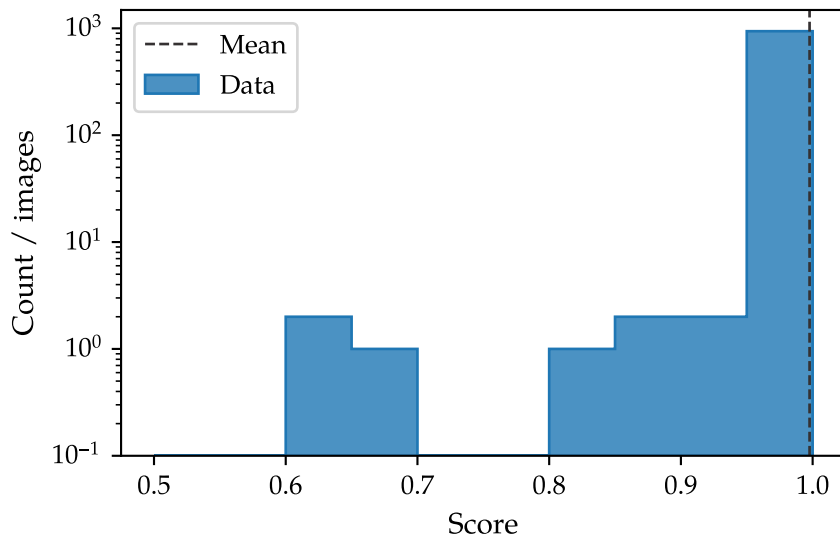
Fig. 7.13.: Score distribution during the winding, for just positive images. Scores until 0.6 appear, but however the threshold for an negative image is below 0.5.
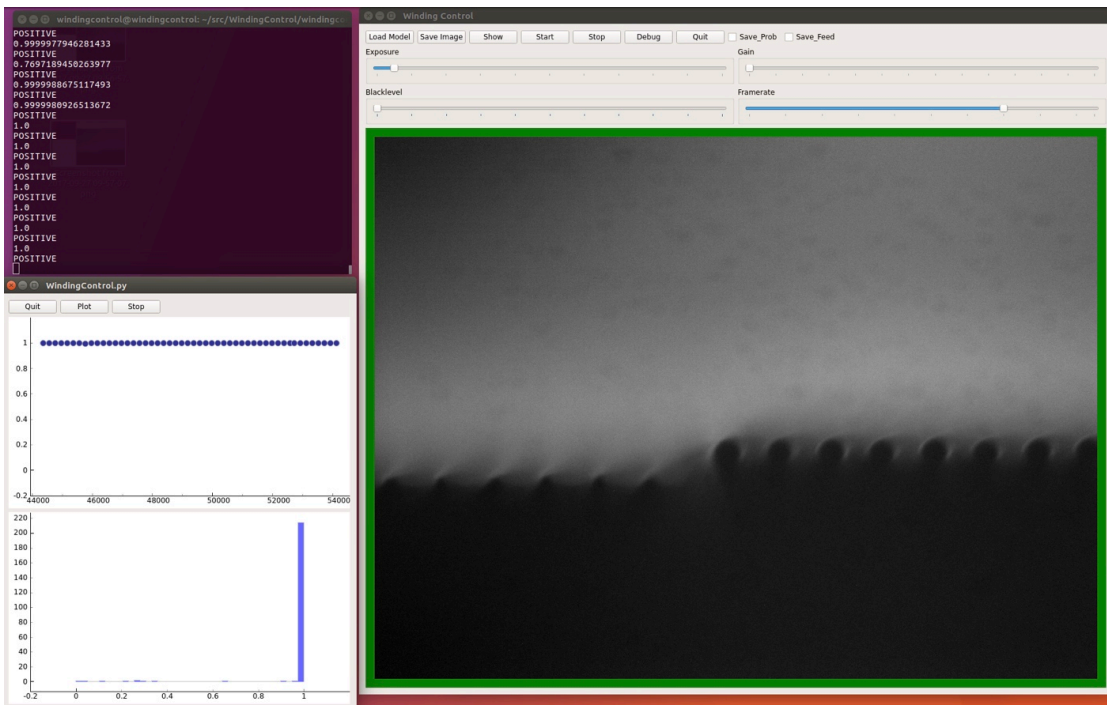

Fig. 7.14.: Screen shot of the developed GUI for the Winding Control application. On the right hand side the camera feed is displayed, with sliders for the camera settings. Also buttons for starting and stopping the classification and other purposes are available. An extra window can be opened to look at the network output by time and as histogram (left side).

91

a wide range of these parameters. However error rates in total are low. The developed winding machine and improved fibre quality allow a sufficient and reliable winding. Hence, if a winding error occurs, it is detected by the Winding Control application. However with the reached accuracy of the trained network (99.99%) and a frame rate of 15 fps of the camera, some positive images may be classified as negative. Requiring a sequence of 5 negative images, provides a higher steadiness of the method. Therefore the machine receives a signal to either stop or just trigger a signal that the Winding Control application recognized a winding error. The winding operator can have a look at the winding pattern, either by looking at the displayed camera feed or at the winding wheel itself, correct the possible winding error and start the winding again. Providing this method to the winding lab allowed to give the winding operators time for other procedures, like lamination of another fibre mat or cleaning the upcoming winding wheel.

7.2. Fibre Mat Shrinking Studies

As mentioned in Sec. 5.2.2, fibres get wound on the winding wheel with a tension of about 50 cN to ensure a proper fibre positioning. This tension was found to be the best value, on the one hand side not damaging the fibre and on the other side allowing a good fibre positioning during the winding of a fibre mat. Several studies have been made to guarantee that the fibre itself is not harmed [76]. In addition it was found out, that the fibre expansion with this tension is about 1 cm [56]. After cutting the mat on the winding wheel, the fibre mat instantly shrinks about this amount, but in the early phase of the fibre mat production it has been noticed that the fibre mat continues shrinking on a longer time scale. The fibre mat length is checked in each Winding Centre by measuring the end piece length and by the use of a special jig. This jig is used during the geometrical measurement (see Sec. 7.5), if the fibre mat fits in, the length should be correct. Though, fibre mats which have been finished did not fit into a special jig any more some weeks after finishing. After this was observed, dedicated studies have been performed of which the results will be presented here.

7.2.1. Setup to measure length variations of a fibre mat

A setup to measure the length variation of a fibre mat is shown in Fig. 7.15. The fibre mat is placed on a jig, which is mounted with a slope. On the one side, the fibre mat is fixed in between two clamps serving as reference position. On the other end of the mat, a small aluminium piece is glued, which serves as stop for a measuring sensor. The stopper is glued outside the nominal length of the fibre mat and is cut away during the optical transversal cut. The sensor records the relative length with respect to the stopper and is read out with Labview [77]. As stated previously, two components of shrinking of the fibre mat appear: a short component for which the winding tension is responsible for and which occurs more or less instantly and a longer one. The aim is to measure both components, which requires that the measurement needs to start immediately after performing the cut on the winding wheel. For a good description for the second and longer component, the measurements were performed over a minimum of 10 days. With this setup, 18 mats were measured in the scope of this thesis.
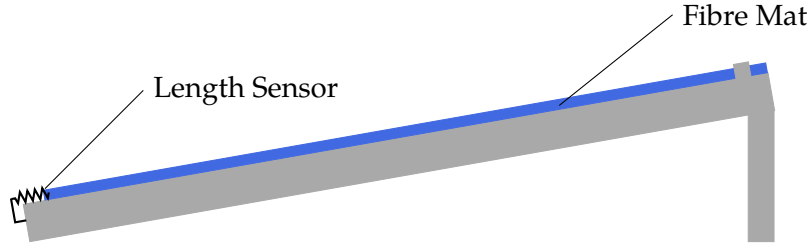
Fig. 7.15.: Setup to measure the length variations of a fibre mat. The fibre mat gets placed on a jig, mounted with a slope, and fixed at one end. On the other side a measuring sensor touching a stop records the relative length.

7.2.2. Data analysis method

The mat shrinking should follow an exponential function with two slopes. The combination of these two exponential functions is done with a sigmoid function, which is defined as:

$$S(t, t_0) = \frac{1}{1 + e^{-s(t-t_0)}}, \tag{7.1}$$

where s represents the steepness of the sigmoid function and t_0 the inflexion point. This approach was chosen to have a continuous and smooth transition of the two exponential functions, taking into account, that in the beginning the length variation is dominated by the first exponential function. Continuity is ensured by demanding $\exp_1(t, t_0) = \exp_2(t, t_0)$. A smooth transition is enabled empirically by setting the steepness factor $s = 5$. According to this, change in length is given by:

$$
\begin{aligned}
\exp_1(t, t_0) &= \exp(b_1 \cdot t) \cdot (1 - S(t, t_0)), \\
\exp_2(t, t_0) &= \exp(b_2 \cdot t) \cdot S(t, t_0), \\
\Delta l(t) &= a_1 \cdot \exp_1(t, t_0) + a_2 \cdot \exp_2(t, t_0) + c, \\
a_2 &= a_1 \cdot \exp((b_1 - b_2) \cdot t_0),
\end{aligned}
\tag{7.2}
$$

where $\exp_1$ represents the first exponential function describing the fast shrinking component with its slope b_1 and start amplitude a_1. The second exponential function is represented by $\exp_2$ with the slope b_2. The second start amplitude is strongly dependent on both slopes, b_1 and b_2, the amplitude a_1 and the inflexion point of the sigmoid function t_0. The relation between these functions is shown in Fig. 7.16.

Fitting this model to data leads to the result as shown in Fig. 7.17. The length variation for a single mat has been recorded over 14 days. The fit result does not describe the data very well as the length variation of the fibre mat is not only affected by the shrinking. Length variations due to a change in temperature and humidity are clearly visible from Fig. 7.18. Therefore temperature and humidity data are recorded and the fit model is adapted accordingly. Changes in temperature affect the fibre mat length on a short time scale, but nevertheless little temperature fluctuations do not exert influence to the fibre mat length. Hence, the temperature progression is smoothed over a time range of 60 min. The influence of the humidity on the fibre mat length is a much slower process as the humidity needs to diffuse into the mat. Therefore the humidity data has been smoothed over a time range of 12 h.
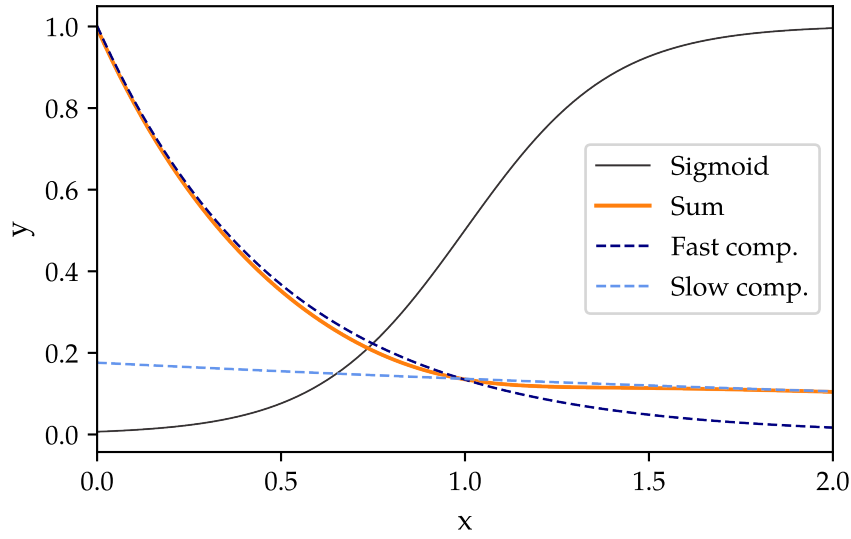
Fig. 7.16.: Sum of two exponential functions with the help of a sigmoid function. In dark blue, the first exponential function (fast shrinking component) and in light blue the second exponential function (slower shrinking component) is shown.

Now, the fit model needs to be adapted in a way, that temperature and humidity effects are taken into account. As already known from literature [78], the temperature coefficient α describes the relative change of a physical property with temperature T. For the length l, it is defined as

$$\frac{\mathrm{d}l}{l} = \alpha \cdot \mathrm{d}T. \tag{7.3}$$

For the relative humidity H, a similar approach has been followed. In Fig. 7.19 the data of a different mat are shown. The length variation due to the temperature happen more or less instantly, but it is visible that the change in length due to the change in humidity is delayed (day 4 to day 6). This effect can be explained by the time the humidity of the room needs to diffuse into the mat and cause a length variation. Therefore an offset t_{off} has been introduced to account for this effect. Finally the fit model, to describe the length variation Δl with time t, takes the following shape:

$$\Delta l(t) = a_1 \cdot \exp_1(t, t_0) + a_2 \cdot \exp_2(t, t_0) + c + \alpha \cdot \mathrm{T}(t) + \beta \cdot \mathrm{H}(t - t_{\text{off}}), \tag{7.4}$$

where $\exp_1$, $\exp_2$, a_1, a_2 and c are defined as in Eq. (7.2). The change in length with humidity is described with the the humidity coefficient β.

The fit is performed with a χ^2 minimizer, where the loss function is defined as:

$$\sum_i \frac{(\Delta L_i - \Delta l_i)^2}{\sigma_i^2}, \tag{7.5}$$

with ΔL representing the measured data of the relative length and Δl the fit model (Eq. (7.4)). As the uncertainty σ_i of a recorded data point is unknown, the assumption has been made that the fit result is the best fit, so that

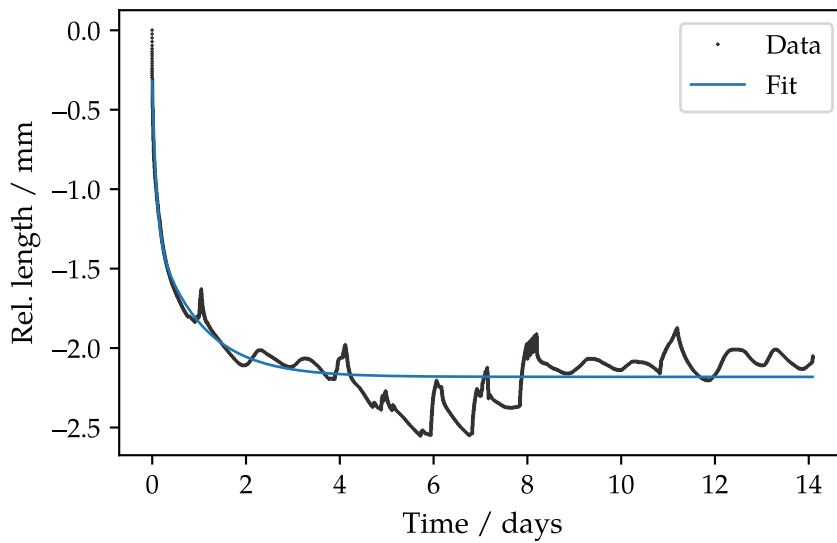$$\frac{\chi^2}{\mathrm{ndof}} = 1 \tag{7.6}$$

Fig. 7.17.: Recorded length variation for fibre mat 72. The fit has been performed with the model described in Eq. (7.2).

should be valid, where ndof stands for number of degrees of freedom. Therefore σ can be calculated, and is the same for each data point. With this assumption, the likelihood is sharper and more Gaussian-like in the region of the estimated value for each parameter. The chosen strategy to handle the fit and its uncertainties is to run a Markov Chain Monte Carlo (MCMC) [79] to sample the likelihood function. A MCMC is a statistical method to sample from a probability distribution based on so-called Markov Chains. This model describes sequences of possible events, where the probabilities are based on the state of the previous event. The equilibrium distribution will be attained as its desired distribution and improves as a function of the number of steps [79].

Performing the 8-dimensional fit on the data presented in Fig. 7.18 results in the plot shown in Fig. 7.20. Free parameters are the amplitude a_1, the slopes b_1 and b_2, a constant of the exponential functions c, the inflexion point t_0 of the sigmoid function, coefficients α, β for temperature and humidity, respectively, as well as the humidity delay t_{off}. The fit describes the recorded length variations very well as well as the temperature and humidity. As previously mentioned, the uncertainties of the fit results are obtained by sampling the likelihood function with a MCMC and determine the estimated values with its standard deviations. The estimated values are the same as given by the minimizer. To allow a better understanding of the 8-dimensional space of the likelihood function, projections as shown in Fig. 7.21 have been made. In addition to the estimated values, correlations between the fit parameters can be seen.

7.2.3. Results and consequences of the fibre mat shrinking

During this thesis, 18 fibre mats have been measured in terms of shrinking. In the beginning, it was the understanding that the fast shrinking component is the one of minor interest. Therefore, the measurements were not started as fast as possible after unforming. This resulted in length measurements starting at different times after unforming. For
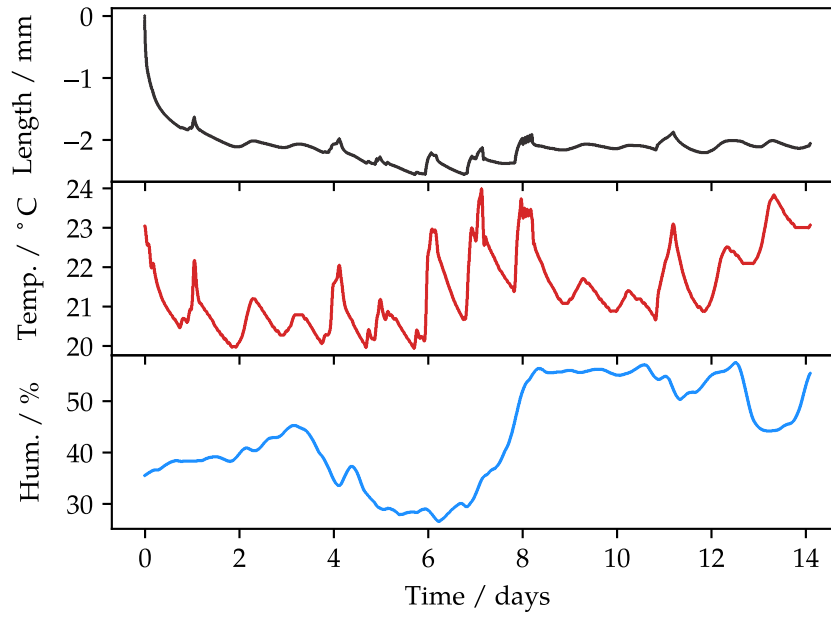
Fig. 7.18.: Recorded length variation for fibre mat 72 and recorded temperature and humidity variations. It is clearly visible, that the fibre mat length is also effected by changes in temperature and humidity.

a better comparison between all measurements, the length measurement was started within 10 min after unforming from the fifth mat on. Hence, for the first four mats a single exponential function for the shrinking behaviour has been used. The analysis method is still the same and for all other mats the model in Eq. (7.4) is used.

The results of all analysed fibre mats are listed in Tab. 7.1. The most interesting parameter is, which determines the time, when the fibre mats does not shrink anymore and hence determines when the fibre mat can be equipped with end pieces. The time t_{100} after which the mat will shrink by 100 μm in addition is determined. For the mats which got fit with a single exponential function, t_{100} can be calculated analytically, but for the combination of two exponential function no analytic solution is available. A numeric method has been chosen to find the root of the resulting function

$$a_1 \cdot \exp_1 + a_2 \cdot \exp_2 - \mu_{100} = 0, \qquad (7.7)$$

where μ_{100} represents the relative length of additional shrinking and the parameters are given by the fit model in Eq. (7.4). A proper description of the parameter is achieved by performing pseudo experiments, where the parameters of the exponential function, a_1, b_1, b_2, c and t_0, are pulled from their Gaussian distribution with the given mean and standard deviation based on the fit result and t_{100} is determined with Eq. (7.7). This results in the distribution like shown in Fig. 7.22, so that the mean and standard deviation can be determined, which are listed in Tab. 7.1 for each mat.

Nevertheless it is possible to combine all results and predict an overall time estimate after which a fibre mat should only shrink by 100 μm. This is a very important parameter, as it declares the period to wait until the fibre mat be equipped with end pieces and be finished. Hence, all fitting parameters are filled into histograms and mean plus
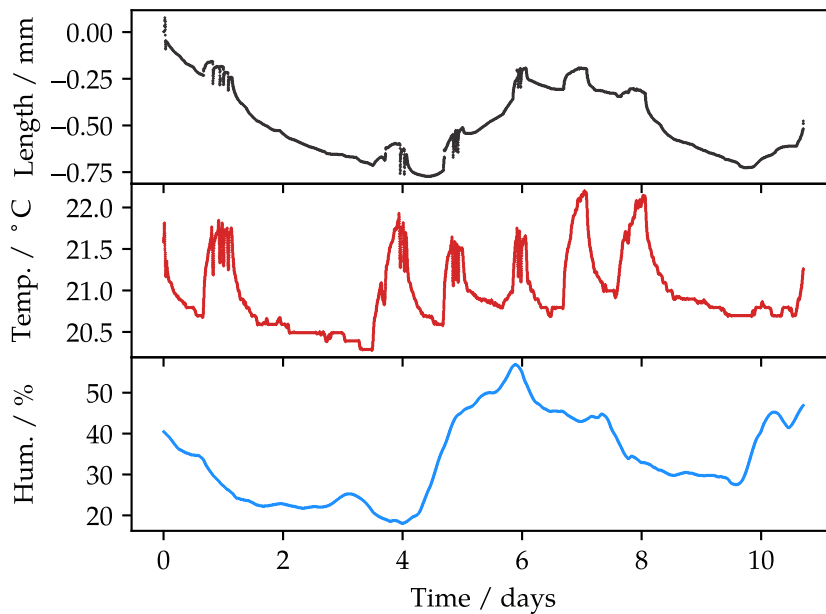
Fig. 7.19.: Recorded length variation for fibre mat 12 and recorded temperature and humidity variations. The temperature effects to the fibre mat length are more or less happening instantly while humidity changes affect the fibre mat length with a delay (between day 4 and day 6).

standard deviation are determined. The resulting histograms can be found in Fig. 7.23 and the overall results are listed in Tab. 7.2. Unfortunately, the value for t_{100} has a large uncertainty. However, for the worst case (largest entry in histogram) the shrinking period would be $28.14 + 0.05 = 28.19$ days, which means a shrinking period of 30 days would be satisfying. Hence, it has been agreed in the mat production group, to wait at least four weeks after unforming to glue the end pieces.

The temperature coefficient α, which was determined to be (0.10 ± 0.03) mm $°C^{-1}$ is compatible with the expectations. It is a combination of the fibres, which are made of polystyrene, and the glue, which is an epoxy. For epoxy, α is given to be 0.055 mm/$°C$ [78] and for polystyrene 0.07 mm/$°C$ [78]. These values agree with the measured value. In addition, the humidity coefficient β was measured. For the end piece glueing of the fibre mats it is essential to know how long the fibre mat is or rather, that the mat is kept at a temperature, that it has the correct length. Hence, the temperature and humidity in the lab is being recorded such that with the help of the determined α and β a target temperature for the end piece glueing jig can be calculated. An interesting parameter in this context is t_{off}, which says, that the fibre mat needs in average half a day to vary its length due to changing humidity conditions. Therefore for calculating the correct end piece glueing temperature not only the current predominating humidity is used, but rather a mean over the last day is determined.

The first, fast phase of shrinking, where the tension due to the winding inside the fibre is released is described by t_0, which means that in average the first shrinking period lasts about half a day. In Fig. 7.23 it is clearly visible, that not all measurements agree with each other, and for some parameters, like t_{100}, a huge spread in visible. Only 18

Tab. 7.1.: Fitting results of all measured fibre mats in terms of shrinking. The complete set of parameters can be found in Tab. A.1. The parameter t_{100} gives the time after which the mat will shrink by only $100\,\mu m$.

Mat	α / mm $°C^{-1}$	β / mm $\%^{-1}$	t_{off} / days	t_{100} / days
12	0.1271 ± 0.0007	$0.014\,09 \pm 0.000\,03$	0.603 ± 0.002	4.33 ± 0.03
22	0.6157 ± 0.0036	$0.004\,27 \pm 0.000\,02$	0.460 ± 0.002	5.06 ± 0.01
23	0.0921 ± 0.0003	$0.005\,52 \pm 0.000\,05$	0.118 ± 0.003	18.89 ± 0.12
26	0.1344 ± 0.0005	$0.009\,02 \pm 0.000\,02$	0.205 ± 0.001	0.47 ± 0.02
42	0.1270 ± 0.0005	$0.012\,06 \pm 0.000\,03$	0.119 ± 0.001	15.71 ± 0.11
51	0.1093 ± 0.0001	$0.012\,43 \pm 0.000\,02$	0.617 ± 0.002	7.07 ± 0.03
54	0.1404 ± 0.0003	$0.014\,92 \pm 0.000\,04$	0.174 ± 0.001	15.71 ± 0.07
63	0.1353 ± 0.0005	$0.012\,76 \pm 0.000\,03$	0.257 ± 0.001	60.13 ± 1.12
72	0.1058 ± 0.0002	$0.014\,38 \pm 0.000\,02$	0.385 ± 0.001	6.19 ± 0.02
88	0.0953 ± 0.0002	$0.018\,07 \pm 0.000\,03$	0.442 ± 0.002	17.37 ± 0.06
105	0.1177 ± 0.0002	$0.014\,91 \pm 0.000\,03$	0.292 ± 0.002	7.66 ± 0.03
127	0.0760 ± 0.0002	$0.013\,76 \pm 0.000\,02$	0.182 ± 0.001	28.14 ± 0.05
148	0.0695 ± 0.0003	$0.012\,38 \pm 0.000\,03$	0.294 ± 0.003	12.29 ± 0.04
161	0.0598 ± 0.0002	$0.009\,76 \pm 0.000\,03$	0.595 ± 0.002	6.41 ± 0.02
173	0.0707 ± 0.0004	$0.006\,86 \pm 0.000\,07$	0.697 ± 0.002	2.36 ± 0.01
179	0.0836 ± 0.0002	$0.011\,80 \pm 0.000\,05$	0.748 ± 0.003	12.00 ± 0.04
240	0.0987 ± 0.0001	$0.009\,96 \pm 0.000\,03$	0.196 ± 0.001	4.41 ± 0.03
262	0.1023 ± 0.0002	$0.011\,53 \pm 0.000\,02$	0.394 ± 0.001	11.72 ± 0.06

Tab. 7.2.: Combined result of all measured fibre mats, which are listed in Tab. 7.1. Mat 63 was not taken into account, as the fit result did not describe the data well.

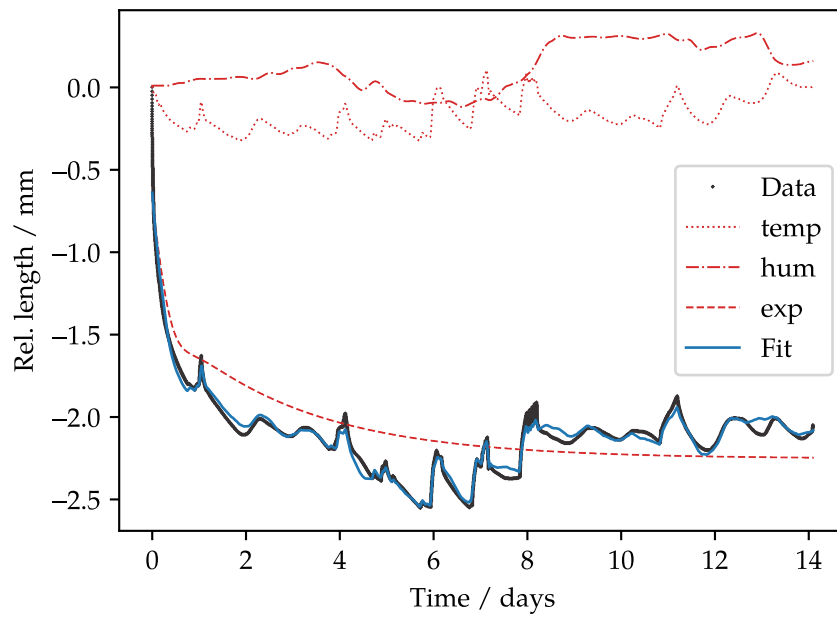| Parameter	Value	Parameter	Value
a_1 / mm	1.77 ± 0.25	b_1 / 1/day	-1.93 ± 1.74
b_2 / 1/day	-0.30 ± 0.26	c / mm	-2.29 ± 0.28
α / $^{mm}/°C$	0.10 ± 0.02	β / $^{mm}/\%$	0.013 ± 0.003
t_{off} / days	0.39 ± 0.21	t_0 / days	0.63 ± 0.41
t_{100} / days	11.31 ± 6.89		

Fig. 7.20.: Result of the performed 8-dimensional fit, with the model listed in Eq. (7.4). The fit is shown in blue, while the individual fit components are shown in red and different line styles. Recorded data of the length variation for fibre mat 72 is display in black.

fibre mats could be measured in the course of this thesis which allow already a quite good conclusion, but measuring more mats would allow reaching higher precisions and therefore a better prediction, how a mat behaves.
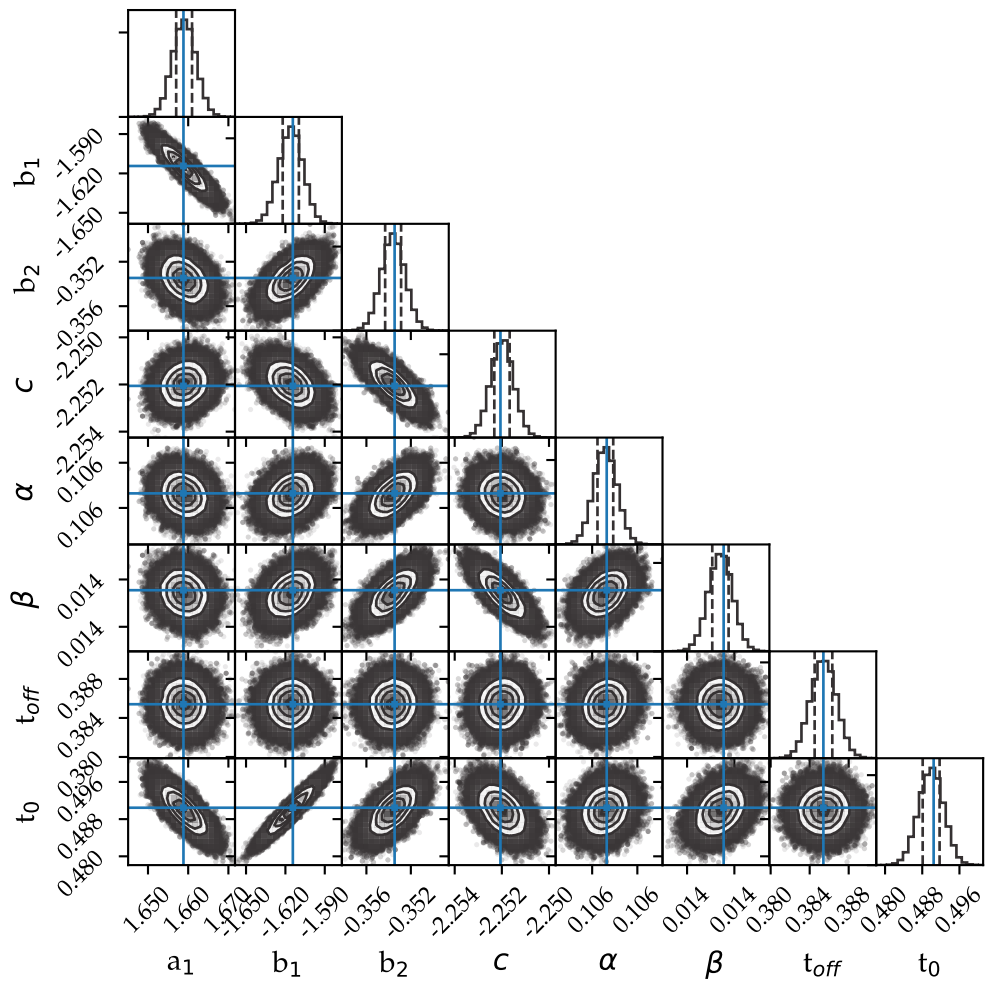
Fig. 7.21.: 1-dimensional and 2-dimensional projections of the sampled likelihood function (Eq. (7.5)). The estimated values are shown in blue. The 25% respectively 0.75% quantiles are marked in the 1D histograms as dashed lines.
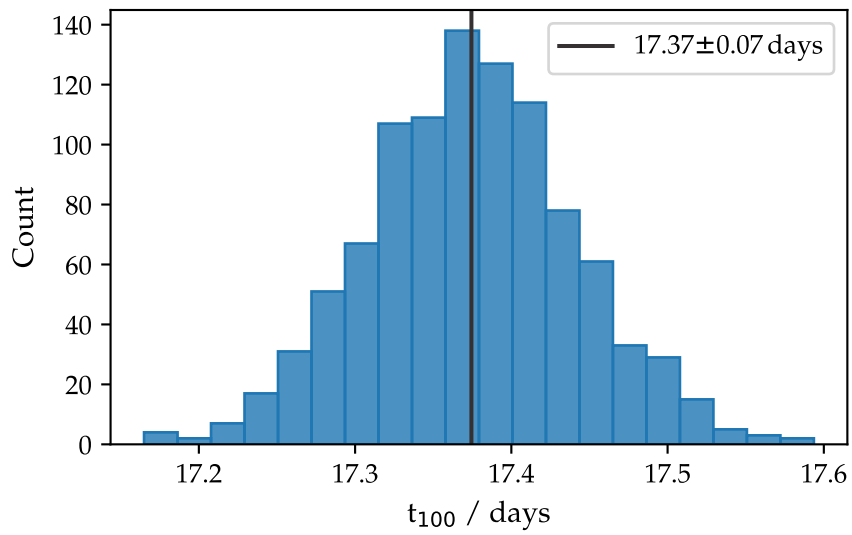
Fig. 7.22.: Distribution of the outcome of performing pseudo experiments to determine t_{100} by finding the root of Eq. (7.7) with a numeric method.
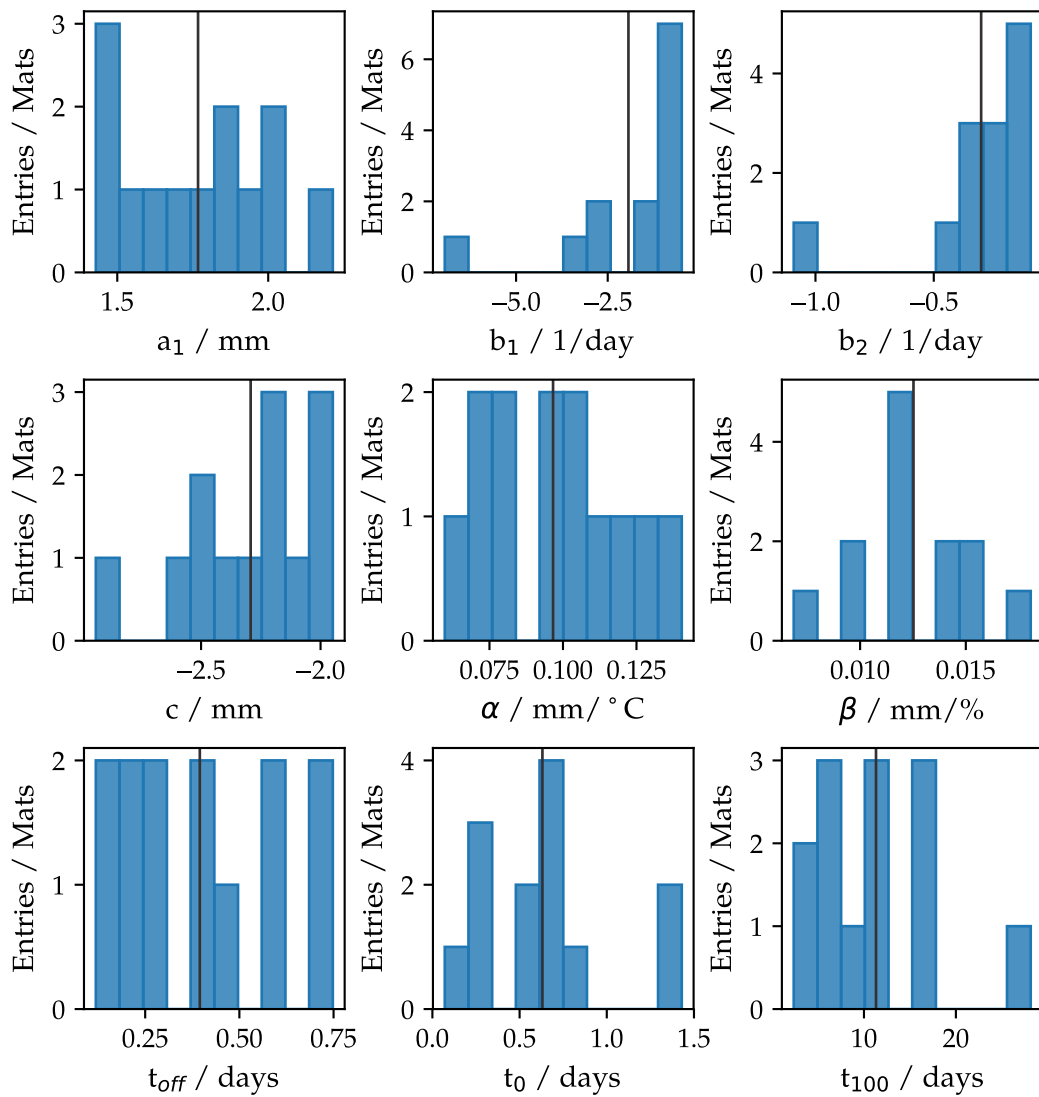
Fig. 7.23.: Histograms of all fit parameters of all measured mats. Mat 63 was not taken into account, as the fit result did not describe the data well. In addition the mean of the distribution is indicated with a black line. Mean and standard deviation for each parameter are listed in Tab. 7.2.

7.3. Optical survey of fibre mat cross section

After the optical cut on the fibre mat the first quality measurement procedure is performed, the so-called Optical Scan. An analysis of the cross sections of the fibres at the end of the mat can be used to determine if the fibre positioning during the winding went well. For this purpose, a test stand like shown in Fig. 7.24 has been developed in the LHCb SciFi group. Based on a previously developed method [80], the gained
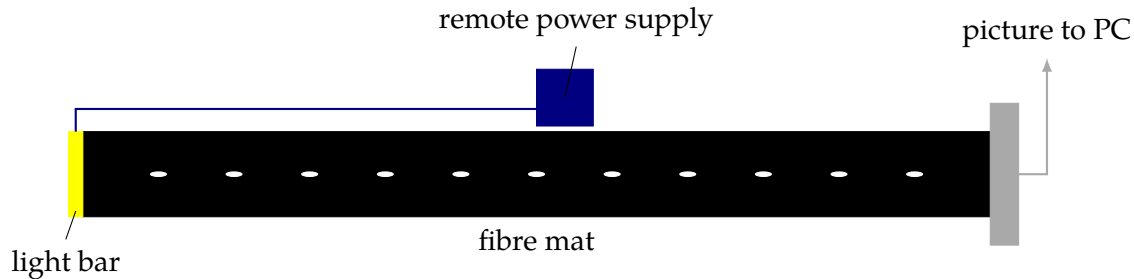
Fig. 7.24.: Optical Scan setup to check the quality of the transversal cut and the fibre matrix. A commercial scanner takes a high resolution image of the fibre mat cross section and with the help of a pattern recognition software, the fibre positioning can be measured.

experience could be used, to give input for the serial production software. It is based on a commercial scanner with a resolution of 9600 dpi and a remote controllable light bar. The fibre mat is placed on a jig with the alignment pins on top. On the one end, the scanner and on the other side a light source is placed. Both components are in contact with the fibre mat. The fibre mat cross section is scanned twice, once just with front light coming directly off the scanner and a second time with additional back light coming off the light bar at the fibre mat end. Afterwards, a pattern recognition software is used to fit circles to the fibre positions (see Fig. 7.25), which gives a hint if the winding overall went well. Also the quality of the optical cut itself can be judged, since with an incorrect
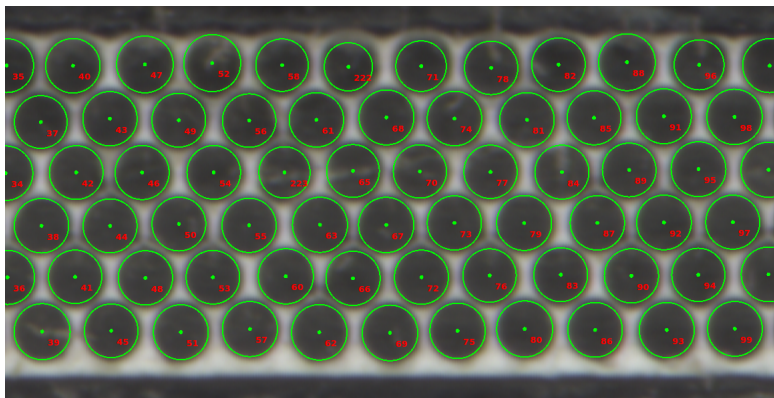
Fig. 7.25.: Scanned cross section of a fibre mat. With the help of a pattern recognition circles are fitted to the fibre positions.

or bad cutting the fibres can be distorted or appear blurry. The difference of the two images (back light and front light) can give a conclusion about the optical transparency of the fibres. Requirements and grades have been found to judge the optical quality of the fibre mat cross section.

7.3.1. Performance grades and requirements

The performance of a fibre mat is dependent on the light output measured at the SiPMs. This is highly dependent on the fibre mat positioning between the end pieces. The SiPMs are aligned to the fibre mat end with help of special alignment holes, which are inserted in the upper SiPM end piece (see Fig. 7.26). However, the SiPM alignment cannot be 100%

Fig. 7.26.: Photograph of a fibre mat cross section on the SiPM side. Three alignment holes are inserted in the upper SiPM end piece.

accurate, wherefore an active window with tolerances has been introduced where the fibre mat has to fit in. The tolerances are fixed to be $\pm 75\,\mu m$. The grades for the optical scan quality are assigned with numbers in the range from 1 to 4, where 1 represents the best and 4 the lowest score. The grade assignment is done with the number of fibres, respectively fibre cross sections lying outside certain boundaries. Therefore two different bounds have been defined. If the SiPM is positioned with an accuracy of 100%, the inner bounds (green in Fig. 7.27) represent the active window of the SiPM. The outer bounds (red in Fig. 7.27) represent the active window of the SiPMs within tolerances. For the grade assignment, the number of fibres exceeding each bound is determined and in addition the total area of calculated which overlaps the boundaries. This area is indicated as an amount of fibre cross sections, with a diameter of $250\,\mu m$, exceeding the boundaries. The concrete grade assignment is listed in Tab. 7.3.

Tab. 7.3.: Grade assignment for the optical scan. The grades are assigned with numbers from 1 to 4, where 1 represents the highest and 4 the lowest score. The number of fibres or fibre cross sections lying outside a certain region is counted and with this the grade determined.

Grade	Specification
1	no fibre outside inner bounds
2	up to 2 fibre cross sections outside
3	more than 2 fibre cross sections outside
4	fibres outside the outer bounds

7.3.2. Fibre mat positioning between the end pieces

In Fig. 7.27, the positions of the 6 layers of fibres is shown, as well as the two bounds, corresponding to the SiPM alignment. The shown mat lays perfectly in between and the fibre layers itself follow a straight line, so that this mat would get the highest grade in terms of optical scan. Is the fibre mat positioning between the end pieces incorrect, the fibres are not laying in front of the active window of the SiPM. In Fig. 7.28, some fibres of the uppermost layer are exceeding the inner limit, such that the mat gets the second lowest grade (3) in terms of the optical scan.
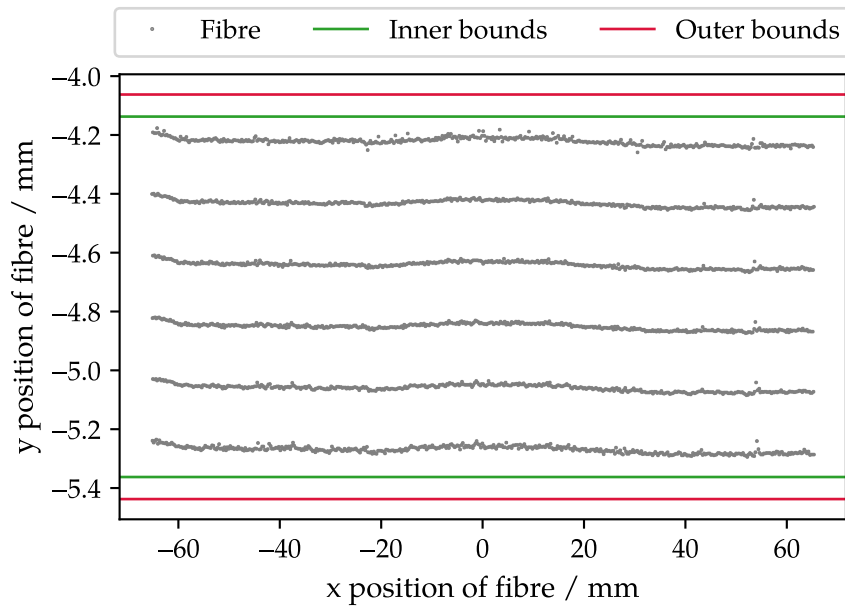
Fig. 7.27.: Fibre positioning between the end pieces. The red lines indicate the bounds of the active area of the SiPM and the green lines the bounds including tolerances. All fibres lay perfectly and straight in between, which corresponds to the highest grade (1).
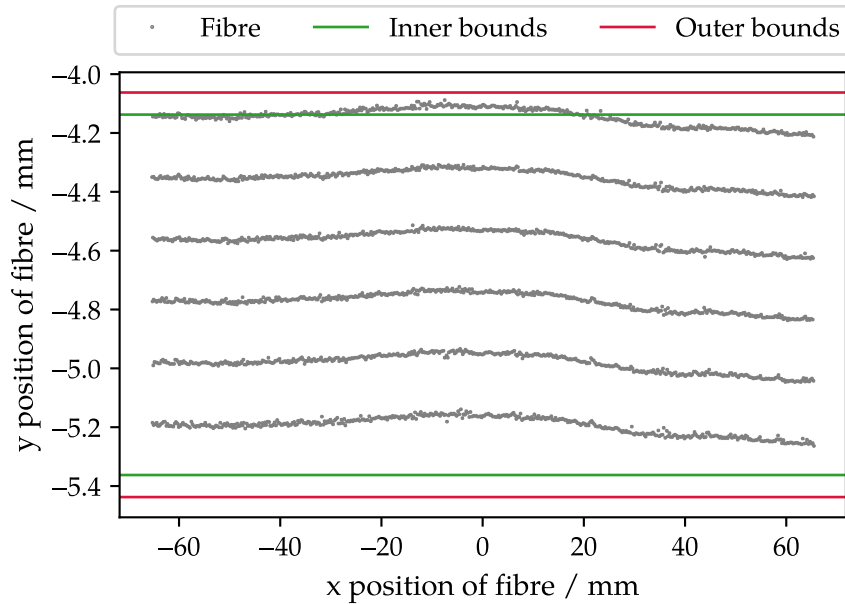

Fig. 7.28.: Fibre positioning between the end pieces. The red lines indicate the bounds of the active area of the SiPM and the green lines the bounds inclusive tolerances. The fibre mat is bent a bit, so that some fibres exceed the SiPM bounds including tolerances, which result in the second lowest grade (3).

The SiPM alignment will be done with the help of alignment holes inside the upper SiPM end piece (see Fig. 7.26). In the optical scan software these pin holes are fitted as well and with respect to their position the bounds of the SiPM region is determined. Therefore the reproducibility of this fit and the depending results have been tested. A mat with several fibres out of bounds has been chosen and then the SiPM alignment holes were fitted several times and the position of the first layer and the number of fibres out of bounds were saved. In Fig. 7.29, both histograms are shown. The first layer is
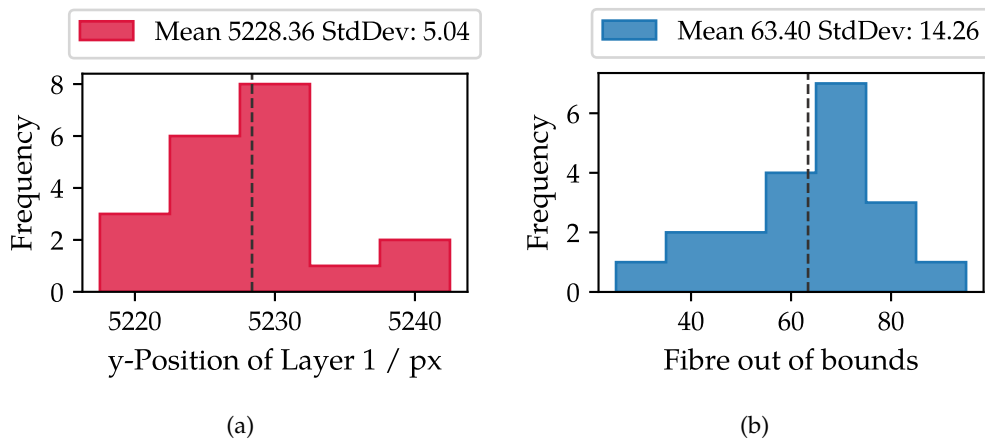
Fig. 7.29.: Distribution of the y-position of the first layer (a) and the number of fibres out of SiPM bounds (b) by repeated fit of the SiPM Alignment hole.

assigned with a standard deviation of 5.04 pixels, which corresponds to 1.33 µm. This value is very low so that a good reproducibility is ensured. The resulting number of fibres exceeding the inner bounds shows a mean of 63 with a standard deviation of 14. Taking the reproducibility of fitting the first layer into account, it is clear, that the fibre can only exceed these bounds with a small percentage of its cross section. Overall this test shows that the software provides a good reproducibility and also with a scanner resolution of 9600 dpi a very good accuracy.

The beginning of the serial production challenges during end piece glueing had to be faced *e.g.* a lot of mats showed fibres exceeding the SiPM bounds. In addition, a non-straight fibre mat trend in between the end pieces was visible (see Fig. 7.30). As the fibre mat is tempered directly after unforming of the fibre mat and pressed in between the end piece sandwich, no transversal bending should be present. In Fig. 7.31 the thickness of the sandwich of fibre mat and SiPM end pieces is shown for several mats. The thickness was measured at several positions along the width and length of the end piece. The blue marker shows the average, while the minimum and maximum is shown in grey. It is clearly visible that some mats show thick spots, which could point out that too much glue was used during the end piece glueing and deforms the fibre mat. For the fibre mat shown in Fig. 7.30, the positions of the edges of the end pieces and of the SiPM alignment hole were measured at the three different positions of the holes. With this, a trend of the end piece form over the fibre mat width can be seen in Fig. 7.32. It is clearly recognizable that the lower end piece is bent towards the upper end piece. As the fibre mat is following the shape of the end piece, it is bent. The thickness of the upper SiPM end piece is greater such that it can hold up and does not bent that much. The clamps which hold the end pieces during glueing are fixed with screws to the end piece glueing
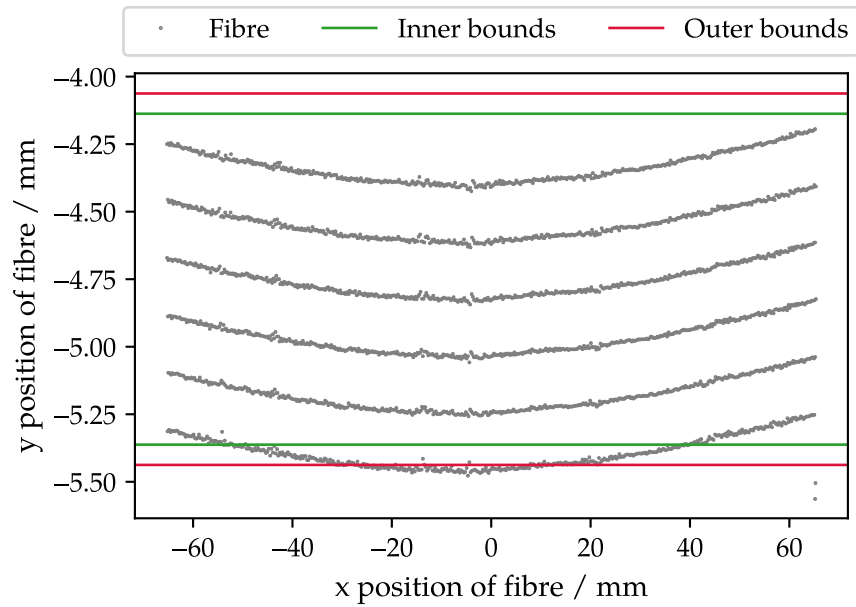
Fig. 7.30.: Fibre positioning between the end pieces. The red lines indicate the bounds of the active area of the SiPM and the green lines the bounds inclusive tolerances. The fibre mat a lot, so that some fibres exceed the SiPM bounds, which results in the worst grade (4).
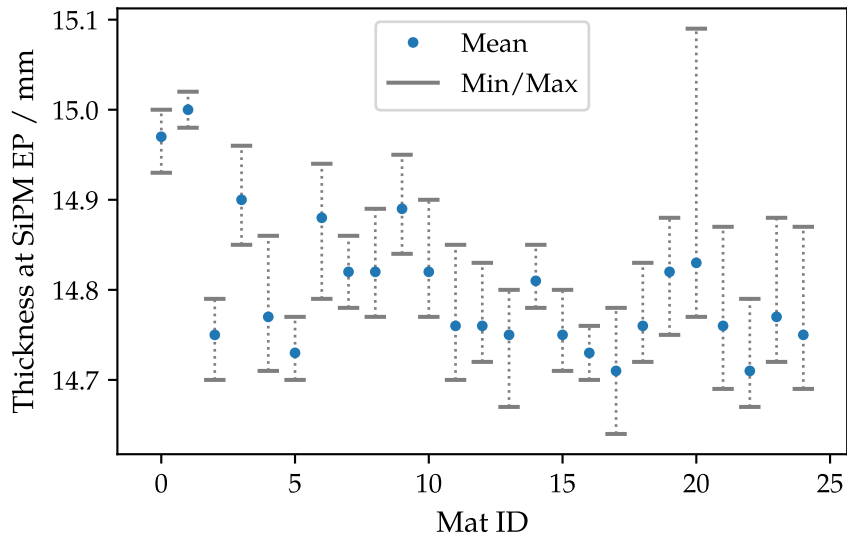

Fig. 7.31.: Thickness at SiPM end piece. The blue marker indicate the mean, while in grey the minimal and maximal measured values are shown.
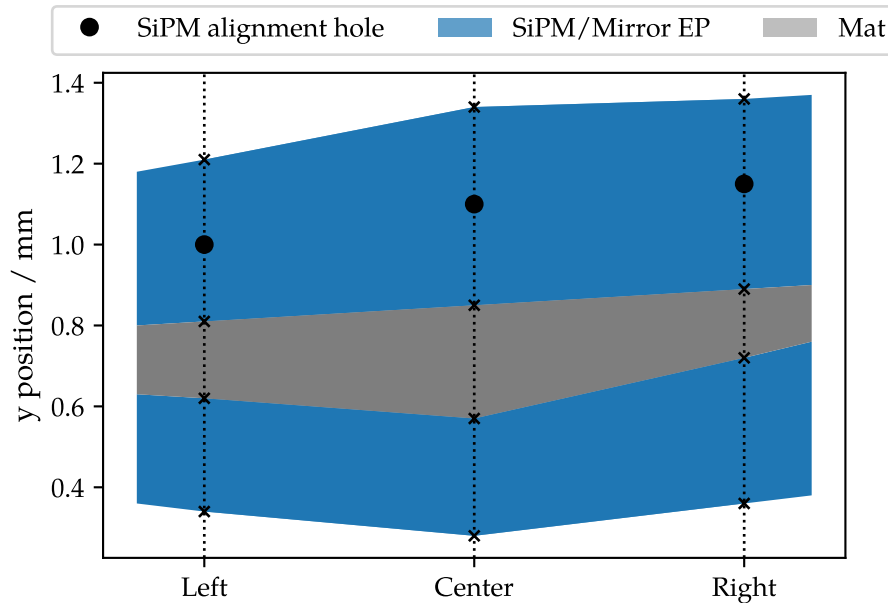
Fig. 7.32.: Positions of the upper and lower edges of the end pieces and SiPM alignment holes, measured at the three positions of the alignment holes (dotted lines). The space holding by the fibre mat and end piece glueing glue is indicated in grey.

jig and apply therefore pressure on the end pieces. Unfortunately, the chosen material of the clamp with its thickness does not hold up the needed force to distribute the pressure over the whole fibre mat width. As a result, the lower SiPM end piece bends, as it is thinner than the upper one. The fibre mat follows its shape and on the upper side of the fibre mat glue piles up, which can also be seen at the scanned images of the fibre mat cross section and result in a too high thickness. The analysis of the taken data during this quality measurement procedure enabled to spot this problem and take corrective actions, so that a proper end piece glueing could be guaranteed. This issue could be solved by adding an additional clamp to the middle of the end piece glueing clamps, such that a smooth distribution of the pressure over the whole end piece width is ensured. This method achieved very good results and the quality in terms of optical scan improved dramatically.

7.3.3. Optical Scan results of the serial production

In the running serial production of fibre mats, about 180 fibre mats were measured with the optical scan setup. Each fibre mat is scanned directly after the optical cut. If the scan shows a bad cut or the mirror has to be removed due to a low gain in light yield, the fibre mat is re-cut and an additional optical scan is performed. Fibre mats are scanned at the SiPM end and the mirror side. A pattern recognition software fits circles to the fibre positions and the SiPM alignment holes, afterwards a summary sheet is created, which holds all important results and information. Also for each scan, a plot, as shown in Fig. 7.27 is created, where the fibre mat shape can be seen. As stated before, the main criterion for the optical scan is the positioning of the fibres between the end pieces with respect to the SiPM bounds. Figure 7.33 shows the evaluation of the number of fibre cross sections lying outside the SiPM bounds for all measured fibre mats. For this number, the
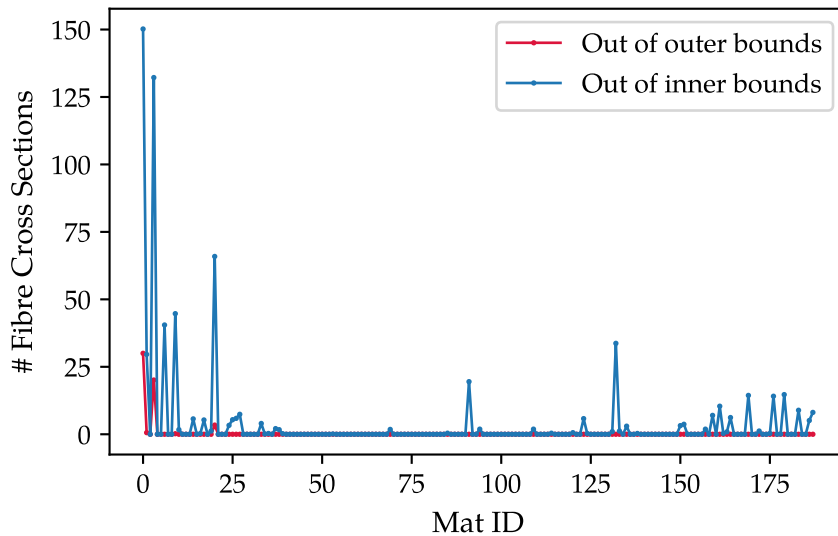
Fig. 7.33.: Number of fibre cross sections exceeding the SiPM tolerances (blue) and active area (red). A clear improvement of the production quality over the time scale of the serial production is observed.

real fibre area exceeding the boundaries is calculated, such that values below unity are possible. With this measure, the quality and therefore the number of fibre cross section outside the inner bounds improved drastically.

7.4. Light Yield measurements

Directly after the optical cut, two quality assurance procedures are applied. First, the previously described optical scan is performed to determine the fibre positioning inside the fibre matrix and between the end pieces. Besides judging the alignment and positioning of the fibres, the light output of a fibre mat is mandatory to judge the performance of the detector. Therefore, a test stand has been developed in the LHCb SciFi group and distributed to all winding centres. A scheme is shown in Fig. 7.34. To measure the light yield of a fibre mat, the scintillation process needs to be stimulated. The fibre mat is excited by the use of a ^{90}Sr source and the response is measured with SiPMs. The setup consists of a jig to place the fibre mat with pins on top. A scintillator with coincidence readout serves as trigger and is placed below the fibre mat. The collimated ^{90}Sr source with an activity of about 16 MBq is situated 14 cm above the fibre mat to ensure an excitation of the total mat width. Before each measurement, the SiPMs need to be calibrated to determine their gain and pedestal. Light pulses coming from a light bar placed below the fibre mat at the SiPM end are shining through the transparent end piece and are guided to the SiPMs. During the fibre mat production, it is necessary to leave this spot free from lamination foil, to enable the light guidance through the end piece. The signal of the SiPMs is sent via an USB board to the PC. A dedicated software ensures an easy handling and the analysis of the data (see Fig. 7.35).

The light yield measurement is performed twice during the production of a fibre mat. Once after the optical cut and optical scan. The number of photons reaching the fibre mat end is measured as well as their uniformity across the fibre mat width, respectively,
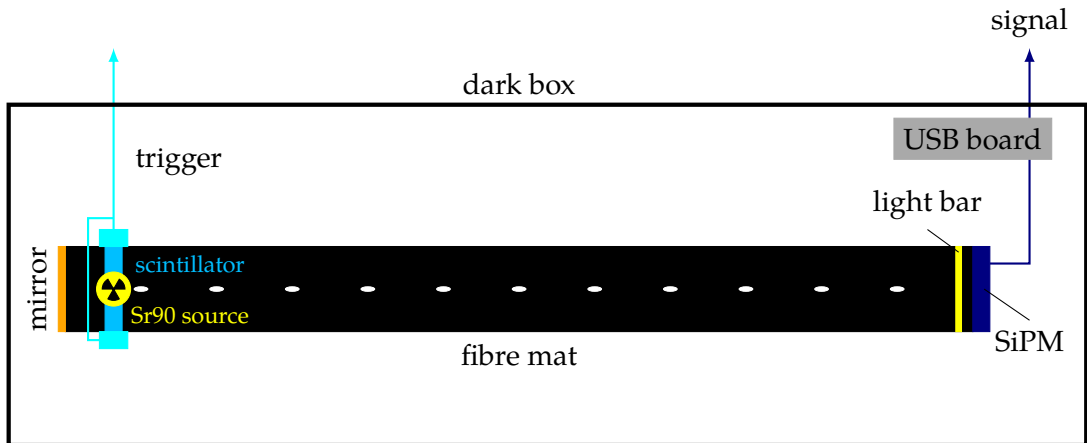
Fig. 7.34.: Setup to measure the light yield of a fibre mat. With the help of a ^{90}Sr source the number of photons reaching the readout end is measured. The measurement is performed in a dark box.

SiPM channels. If these quality control procedures do not show any deviations, a mirror is glued to the fibre mat end. After the mirror glueing, a second light yield measurement is performed to check the mirror efficiency and the glueing itself. In the event of a partial lift off of the mirror, a dip in the light yield on the particular spot is visible (see Fig. 7.36). This requires a new mirror glueing, hence the mirror side needs to be re-cut. Doing so, it needs to be ensured that the fibre mat length does not get to short.

After the fibre mat is geometrically checked (see Sec. 7.5), the fibre mat is shipped to the Module Centres to get assembled to a full size SciFi detector module (see Sec. 5.3). The longitudinal cut to the correct fibre mat width is a dedicated step, therefore the same light yield measurement is performed just before and after the longitudinal cut. Thereby a damage due to the transport of the fibre mats can be excluded or asserted and a possible down graduation of the mat due to a non-perfect longitudinal cut is toggled.

7.4.1. Performance grades and requirements

The light yield of a fibre mat is an essential quality property in terms of the detector performance. Therefore a special grade was introduced to assess the fibre mat quality in terms of its light yield. These specifications are the same for each Winding Centre to ensure comparability. The light yield measurement belongs to the set of performance grades and is assigned in numbers form 1 to 4, where 1 represents the highest and 4 the lowest grade, as for the optical scan grades. The light yield is determined for each SiPM channel and the mean depicts the distribution over all 512 channels with the standard deviation as its width. For the grade assignment, only the light yield per channel is taken into account. For this, channels with a low light yield are counted. Low light yield channels are located with the help of a dataset of several light yield measurements. This data set defines a 2-RMS region[4] around the mean - each channel lying below this region is counted as a low light yield channel. The grades are therefore assigned as listed in Tab. 7.4. The light yield grade is then combined with the grade from the optical scan to result to an overall performance grade, see Sec. 7.6.

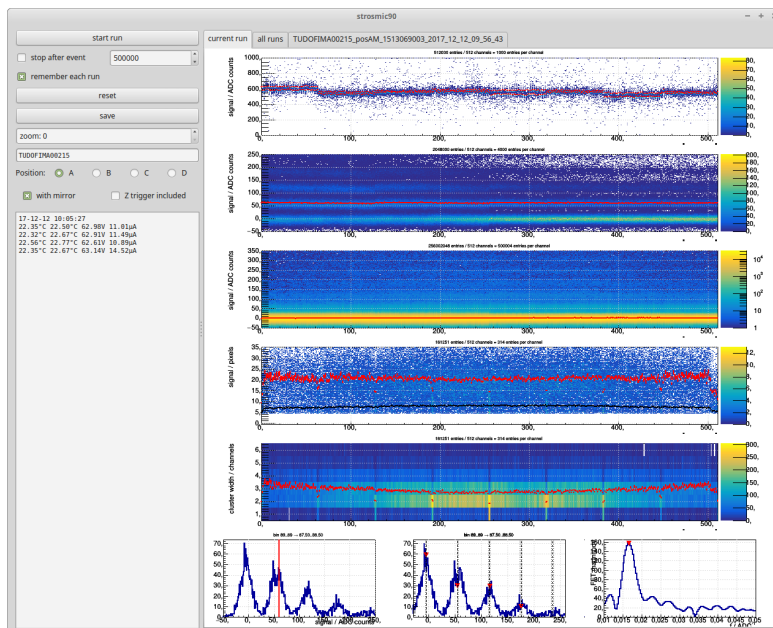[4]The standard deviation of the distribution is used.

Fig. 7.35.: Screen shot of the software used for the light yield measurements. Besides housekeeping data, like the temperature and bias voltages of the SiPMs, the recorded data is displayed. From top to button: pedestal, LED measurement, signal in ADC counts, signal in pixel and cluster width; all per channel. The lowest row shows the respective projections on the y-axis.
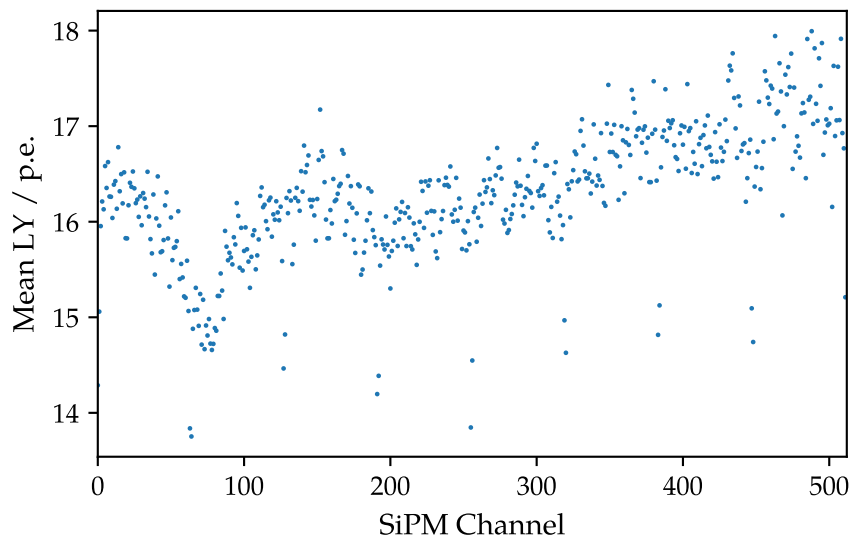

Fig. 7.36.: Light yield per channel of a fibre mat. Between channel 40 and 100, a drop in the light yield is visible. This dip can be caused by a peel off of the mirror.

111

Tab. 7.4.: Grade assignment for the light yield measurement. The grades are assigned with numbers from 1 to 4, where 1 represents the highest and 4 the lowest grade. The number of low light yield channels per fibre mat is counted and the grade determined.

Grade	Low light yield channels
1	less than 20
2	21-50
3	51-200
4	>200

7.4.2. Calibration and alignment measurements

Before using the light yield test stand for the serial production, measurements have to be performed, to understand and verify its behaviour. After the mat is placed into the test stand, the SiPMs have to be placed in front of the one fibre mat end. The height of the SiPMs just fit the height of a six layer fibre mat, hence a correct alignment of the SiPMs is mandatory. This includes the correct distance to the fibre mat end. In Fig. 7.37, the mean light yield[5] of a fibre mat as a function of the distance of the SiPMs to the fibre mat end is shown. It is clearly visible that the light yield drops with increasing distance, as the emergent photons have a higher possibility to be scattered outside the SiPM window. In addition, a small plateau in the beginning of the curve is present, which means that within 100 μm the mean light yield will stay constant and the SiPM distance needs to be accurate within that distance. On the other hand, the cluster width
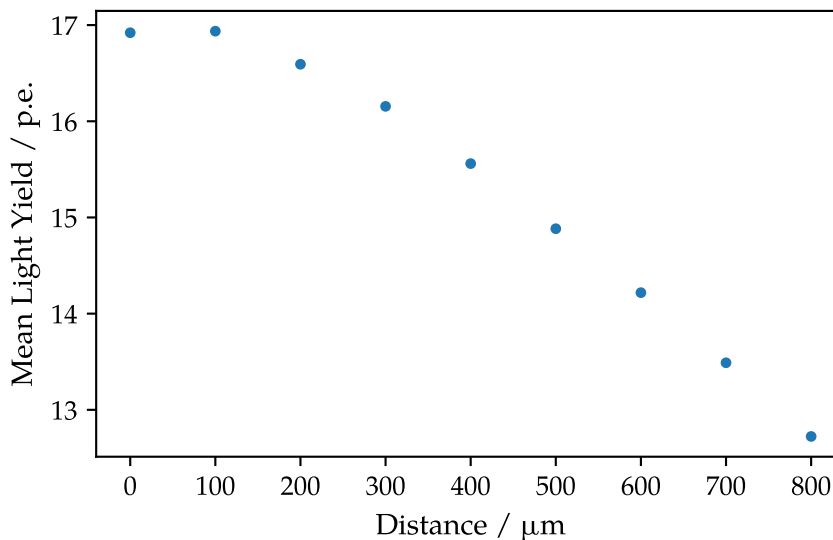
Fig. 7.37.: Mean light yield of a fibre mat as a function of the distance to the SiPMs. After around 100 μm the light yield begins to decrease.

is increasing with a higher distance of the SiPMs to the fibre mat end, see Fig. 7.38. The cluster width represents the number of SiPM channels which form a cluster in one event. With increasing distance, the exiting photons under higher angles hit SiPM channels

---

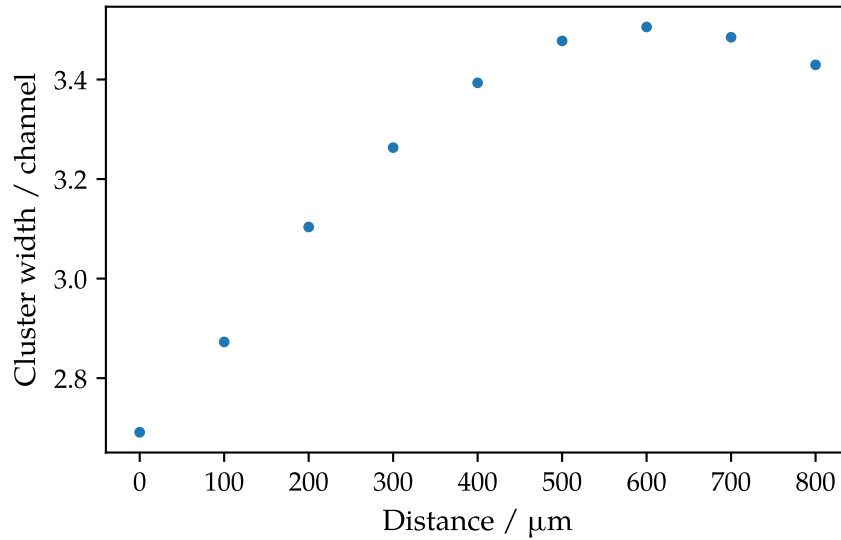[5]The mean of the light yield over all SiPM channels is calculated.

Fig. 7.38.: Cluster width of a fibre mat as a function of the distance to the SiPMs.

which are further away with respect to the exit position. For distances greater than 600 μm, the cluster width is also decreasing as less photons hit the SiPM, which comes along with the decreasing mean light yield.

Besides the distance of the SiPMs to the fibre mat end, even sensitive parameters are the vertical and horizontal alignment of the fibre mat with respect to the fibre mat end. The provided test stand by the LHCb SciFi fibre mat production group did not allow a precise alignment of the SiPM in all axes. Therefore a new mounting (see Fig. 7.39) for the SiPMs has been constructed and dedicated measurements performed to achieve the best SiPM alignment. First, the right-left-alignment of the fibre mat in front of the

(a)

(b)
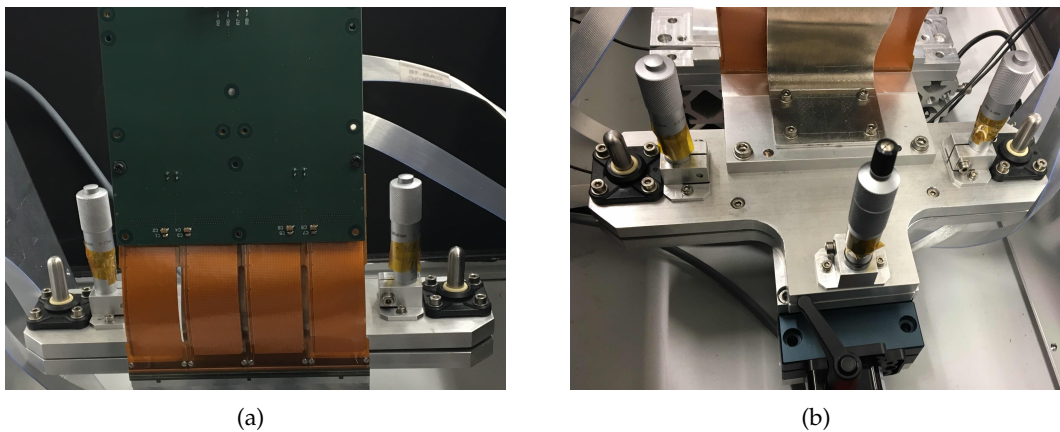
Fig. 7.39.: Improved SiPM mounting; three micrometer screw gauges allow to adjust the horizontal and vertical alignment.

SiPM window is studies. For this, a tape is attached to each edge of the SiPM end piece covering the fibre ends. This tape will prevent the photons from reaching the SiPMs and these regions appear as dead in the light yield scan. The result is shown in Fig. 7.40.

The region between the two blue lines matches the region without tape and is perfectly centred across the SiPM channels. Measurements and adjustments of the vertical and horizontal position followed afterwards, therefore the light yield in this region is not constant but rather drops towards higher channels.
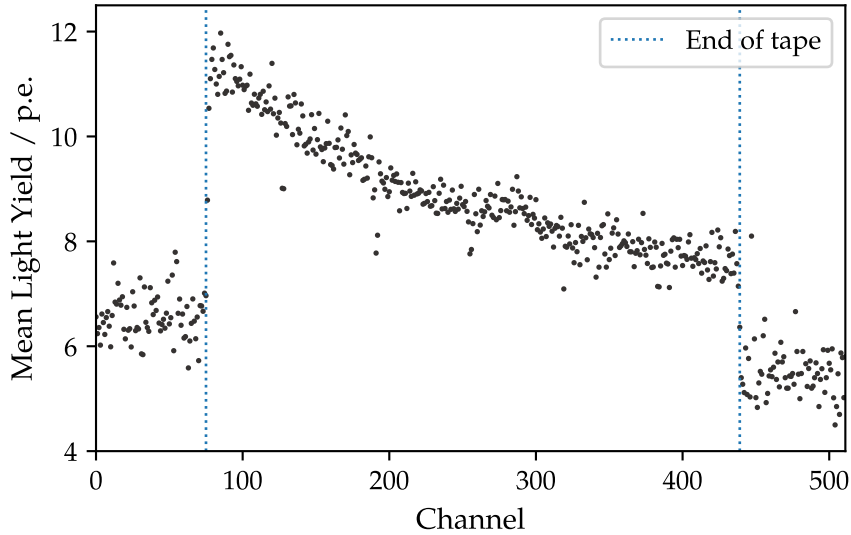

Fig. 7.40.: Mean light yield of a fibre mat. The left and right edge was covered with a tape to check the right-left-alignment of the SiPMs. The active region is perfectly centred, but the light yield drops due to bad vertical and horizontal alignment of the SiPMs.

Three micrometer screw gauges allow to adjust the horizontal and vertical alignment, which leads to a huge amount of possibilities to position the SiPMs. Therefore, multiple systematic measurements have been performed with several different adjustments of the micrometer screw gauges. These measurements are shown in Fig. 7.41. The mean light yield at different positions across the fibre mat width is shown. At the left and right edge, the light yield was averaged over 100 SiPM channels. Adjusting the three different micrometer screw gauges systematically resulted in the best alignment with the highest light output.

In the beginning of the serial production phase the energy spectrum of the ^{90}Sr source has been studied. The best comparability of the light yield of the fibre mat is achieved by using minimum ionizing particles (MIP), as these are the most similar to the created particles in the LHCb detector and at test beam campaigns. Adding an absorber between fibre mat and trigger allows to trigger on highly energetic particles, which are compatible with MIP [81]. It was agreed to add a 3 mm thick acrylic glass absorber. As a consequence a lower mean light yield of the fibre mat is measured, as shown in Fig. 7.42.

Fibre mats are produced at four different Winding Centres and each of them own a similar ^{90}Sr test stand. Although they are identical in construction and the same equipment (SiPMs, trigger, ...) is used, it needs to be ensured that the results are compatible. Hence, is has been agreed on that all light yield results are corrected to the corresponding ones which would be performed with the setup in Aachen. For this purpose, some mats got measured in Dortmund (DO) and in Aachen (AC) - the results are shown in Fig. 7.43. The correction factor for the light yield measured with the Aachen setup could be determined to be 1.048 $\pm$ 0.009. It is clearly different from unity, which shows that the test stand
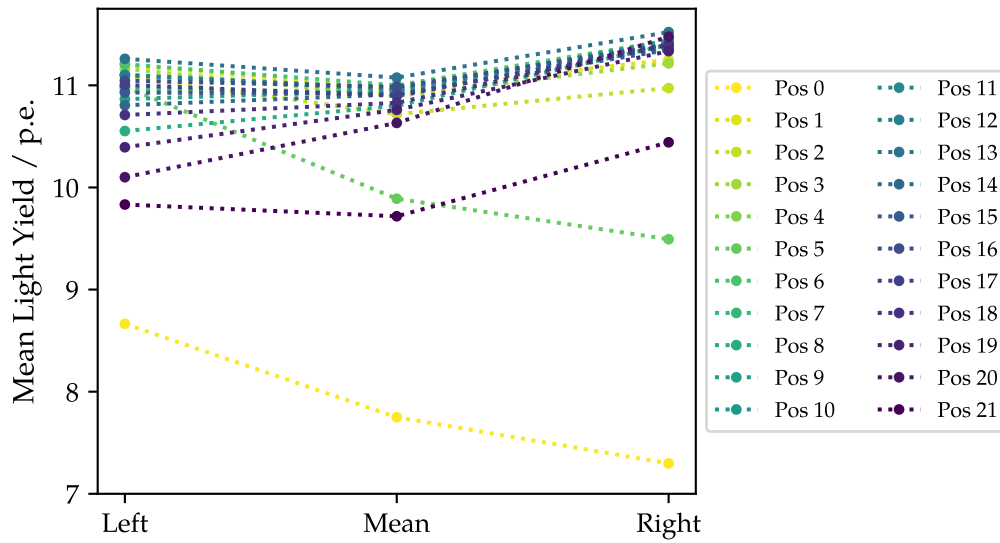
Fig. 7.41.: Measurements for the perfect vertical and horizontal alignment of the SiPMs. The left dot represents the mean light yield over the 100 left and the right dot the mean over the 100 right channels. At position 0 the mean over all SiPM channels is plotted.
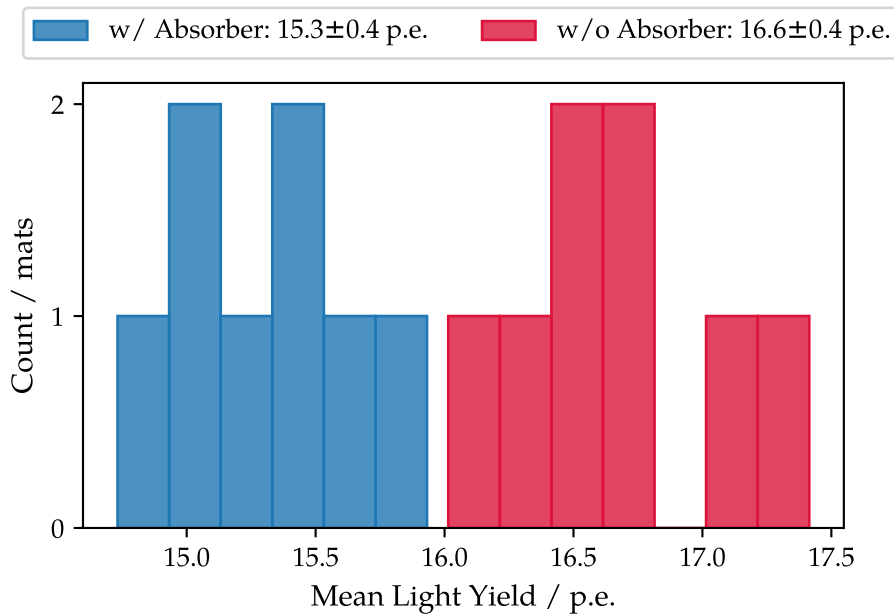

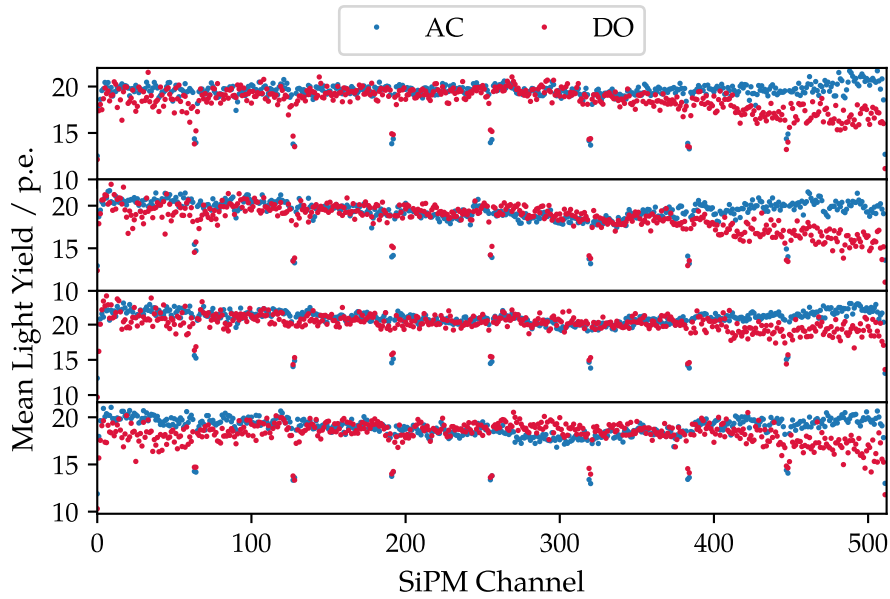Fig. 7.42.: Measurement of 8 fibre mats w/ and w/o acrylic glass absorber plate of 3 mm height.

Fig. 7.43.: Light yield measurement of four mats in Aachen (AC) and Dortmund (DO) to determine a correction factor between the two setups.

behave slightly different. The light yield trends over the SiPM channels show the highest deviation at SiPM channels between 400 and 500. This deviation is visible for all four analysed fibre mats, which means it is systematically. A different SiPM alignment or the end piece alignment inside the clamps could be a reason. But also the used ^{90}Sr source and its radiation geometry can induce this observation.

7.4.3. Light yield results of the serial production

So far about 150 mats have been measured under serial production conditions in Dortmund. On each mat two light yield measurement were performed, one without and one with the mirror attached. The light yield is, as mentioned previously, dependent on the used setup and therefore corrected to the Aachen setup. Besides this dependency, the operation of the SiPMs is temperature dependent and therefore the measured light yield, as shown in Fig. 7.44. With increasing temperature of the SiPM the light yield decreases. It is not a large effect as already corrections are applied in the ^{90}Sr software. However, all shown light yield measurements are therefore as well corrected to a reference temperature reflecting the average temperature. For each mat, a plot as shown in Fig. 7.45 is produced. It shows the light yield per SiPM channel with and without mirror as well as the mirror gain per channel. The dips in light yield trend refer to the dead zones between the SiPM dyes.

All light yield data of all measured mats are collected and fed into the histogram displayed in Fig. 7.46. The mean for fibre mats without the mirror attached is 11.91 ± 0.67 p.e. and for mats with mirror equipped 19.69 ± 1.23 p.e.. Both light yield measurements can also be combined in a plot like in Fig. 7.47. A scatter plot of both light yield measurements is displayed. Straight lines are added which correspond to different percentages of mirror gain. With this the mirror gain of a fibre mat can be seen easily.
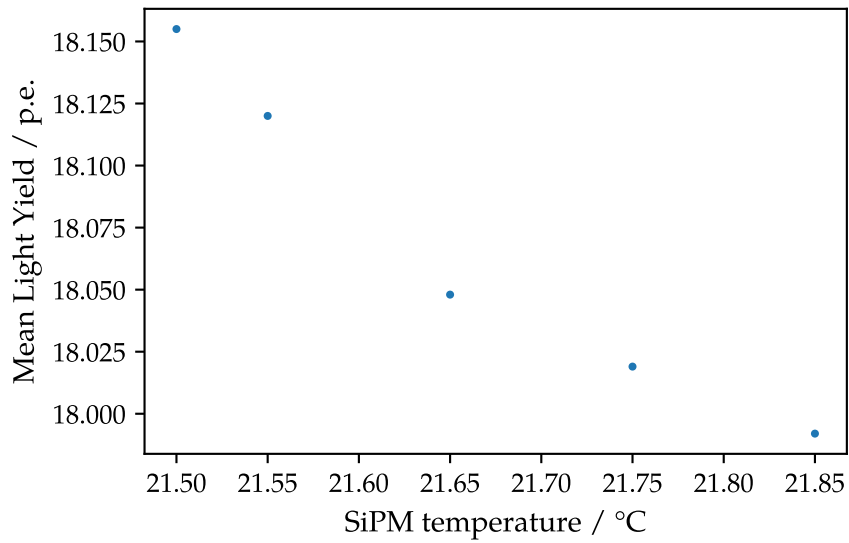
Fig. 7.44.: Mean light yield measured at one fibre mat for as a function of the SiPM temperature. With increasing temperature the light yield decreases.
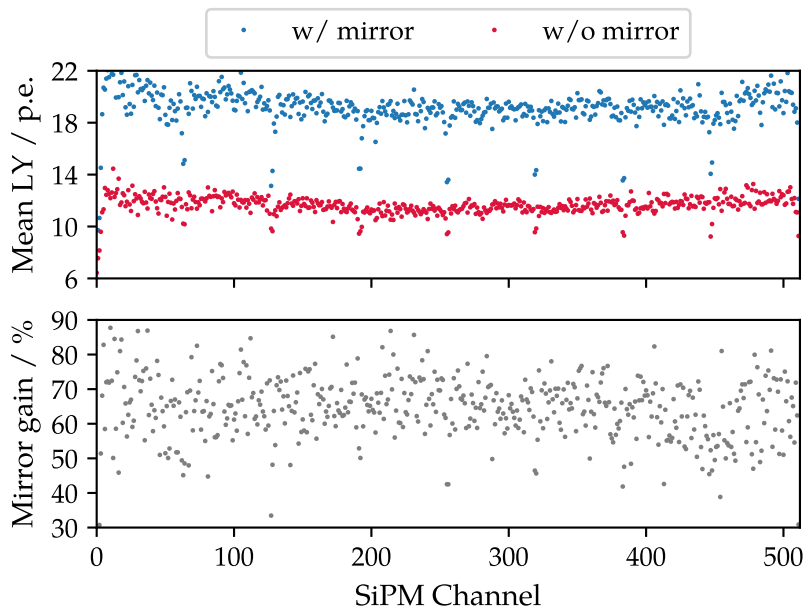

Fig. 7.45.: Light yield per channel with and without mirror for one fibre mat. The lower plot shows the corresponding mirror gain per channel. Regular dips in light yield correspond to dead zones between the SiPM dyes.
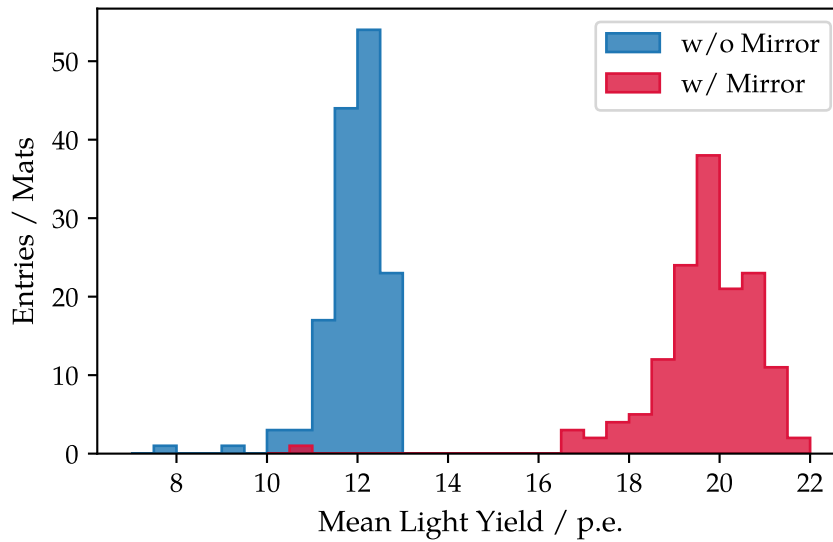
Fig. 7.46.: Mean light yield distribution for all measured mats so far. One fibre mat was damaged during the production which resulted in a low light yield with mirror.
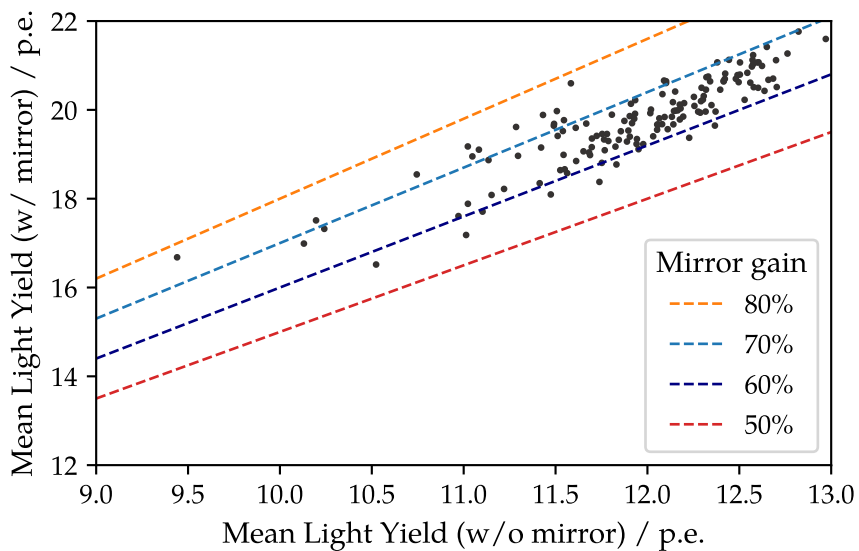
Fig. 7.47.: Scatter plot of the both light yield measurements. Straight lines indicate the different mirror gains.

After the fibre mats are finished in the Winding Centres, they are shipped to the Module Centres, *e.g.* in Heidelberg (HD). After arriving there, the light yield is determined. Once more for two reasons: first with this measurement it can be easily checked if the mat got damaged during transportation. On the other hand, the measurement is used to compare it to another light yield measurement right after the longitudinal cut to the fibre mat width. The longitudinal cut is done with two parallel circular saws to reach a minimal loss of acceptance at the boundary of two neighbouring fibre mats. However, if the longitudinal cut is not accurate fibres inside the acceptance can get scratched and therefore a decreased light output in the SiPM channels at the edges is visible. Moreover, a comparison and the correlation of this data to the data measured in the Winding Centre is interesting. Figure 7.48 shows the light yield measured in Dortmund as a function of the light yield measured in Heidelberg. The measurements scatter a lot, but however
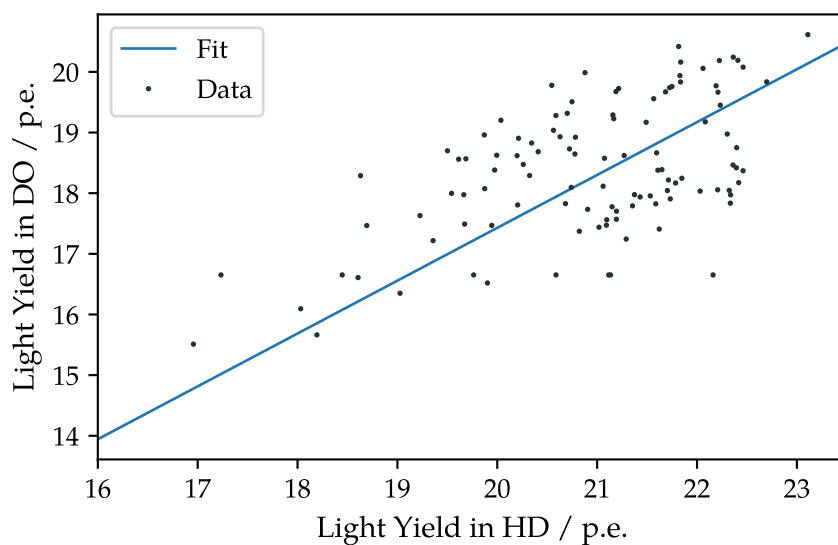

Fig. 7.48.: Correlation of light yield measurements performed in Dortmund and Heidelberg. A linear function through the origin is fitted to the scattering data.

a linear function through origin can be fitted to have the gradient 0.871 ± 0.004. This factor differs from unity as the light yield test stand in HD does not use an absorption plate, such that a higher light yield is measured by default. But also differences like the SiPM alignment can be a reason for having a deviation from unity.

7.4.4. Comparison between different institutes

Studies have been performed to compare the in-house produced fibre mats to the ones produced at other winding institutes. As all fibre mats go firstly to the Module Centre in HD, because only here the longitudinal cut is performed, the data of the measurement performed in HD is used to be independent of the light yield setup. A histogram for each Winding Centre has been filled with their light yield data (see Fig. 7.49). The mean

and standard deviation for each institute are

$$AC = 21.35 \pm 1.36 \, \text{p.e.,}$$
$$EPFL = 20.51 \pm 1.03 \, \text{p.e.,}$$
$$DO = 20.96 \pm 1.17 \, \text{p.e..}$$

Small deviations between the results of the institutes are visible, therefore a closer look
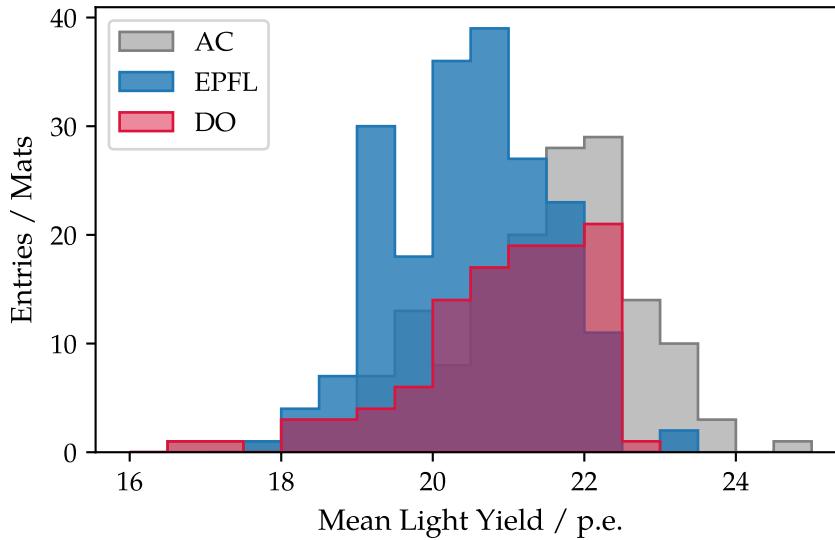

Fig. 7.49.: Distribution of the mean light yield of produced mats, separated by their origin.

into the data is interesting. Plotting the mean light yield as a function of the time[6] gives the plot in Fig. 7.50 and could show a small dependency.

By looking at the light yield of the base material, the single scintillating fibre, the deviations can be explained. Figure 7.51 shows the distribution of the light yield for single fibre spools, which where used to produce a pure[7] fibre mat. Unfortunately it is just a small data sample, but however the histograms show, that all Winding Centres receive the same samples of fibres in terms of light yield. Figure 7.52 shows the mean light yield of a fibre mat as a function of the single fibre light yield. Assuming a correlation between the two parameters, a linear function trough the origin can be fitted for each winding institute, resulting in the following proportional factors

$$a_{AC} = 3.02 \pm 0.04,$$
$$a_{EPFL} = 2.97 \pm 0.04,$$
$$a_{DO} = 3.15 \pm 0.04.$$

Summarising the light yield of a fibre mat is dependent of the light yield of the single scintillating fibre. However, it is not the only contribution, as *e.g.* the mirror gain smears the distribution as well. Overall, taking the varying fibre light yield into account, all Winding Centres produce mats of similar quality in terms of light yield.

---

[6]The time of the measurement in Heidelberg was used.
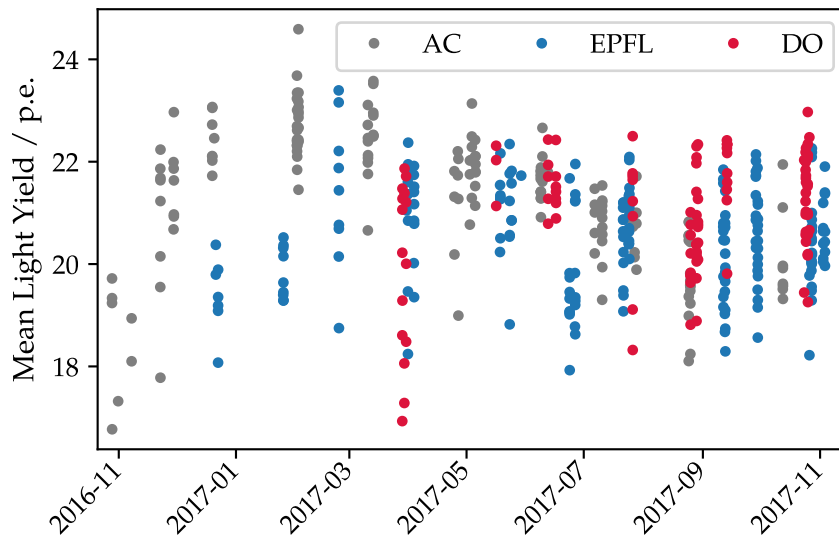[7]Fibre mat produced from one fibre spool.

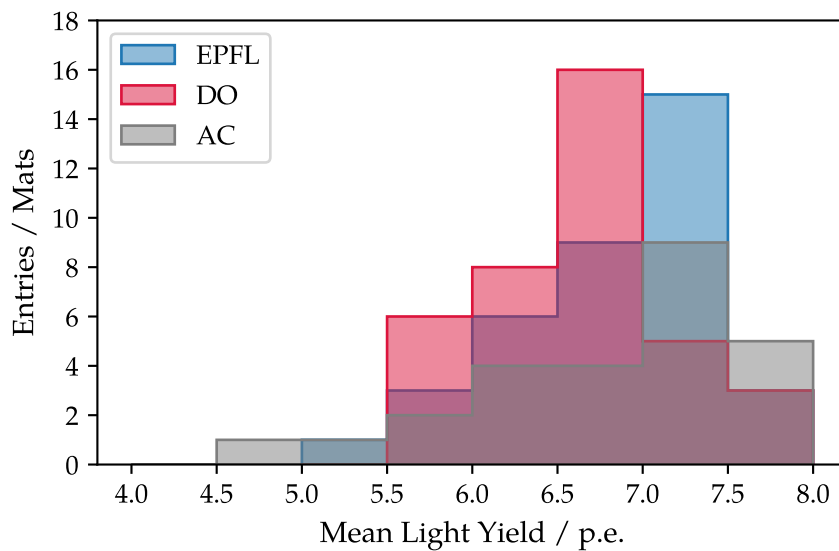Fig. 7.50.: Mean light yield over time for three Winding Centres.

Fig. 7.51.: Single fibre light yield distributions, for fibre mats made from a single spool, grouped by their Winding Centre.
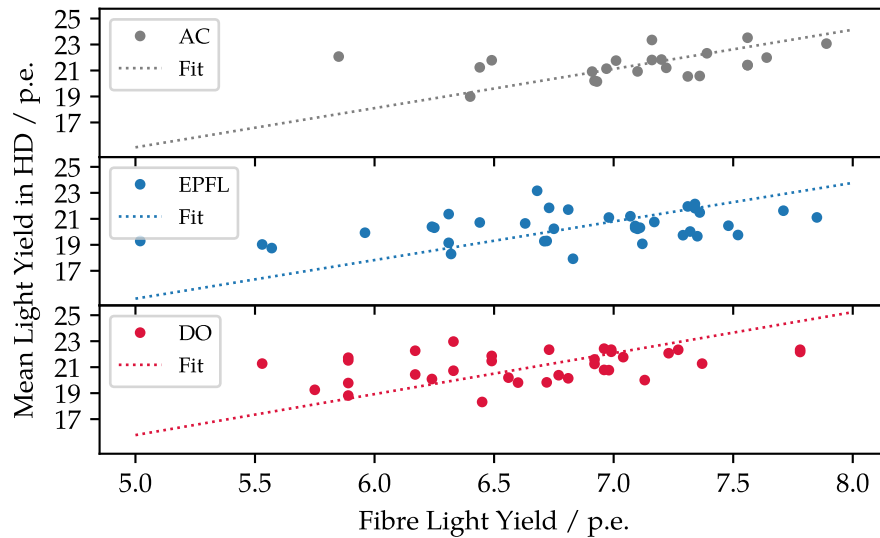
Fig. 7.52.: Mean light yield of a fibre mat as a function of the single fibre light yield, for each winding institute. A linear function through the origin has been fitted to the data.

7.5. Geometry measurements

After finishing and just before shipping to the Module Centres the geometric properties of each fibre mat are measured and geometric scores assigned. Geometrical scores are given in the range from A to D, where A represents the highest and D the lowest score. Besides measuring the geometrical shape like the thickness of the fibre mat, the SiPM end piece, the mirror end piece and the transversal bending, other geometrical properties are determined. The end pieces serve as a support for the SiPMs and the mirror. The edges need to be free from glue and sharp to avoid difficulties during the module production. One geometrical mark is given depending on the status of the end pieces, if residual glue prevents the mat from fitting into the module production jig. To perform this test also in the mat production centres, a special jig was produced in the LHCb SciFi group and distributed to the Winding Centres. It is a mockup of the module production template, with the exception that only one mat fits in, see Fig. 7.53. However, with this jig it is possible to determine if too much glue is present on the end pieces which prevents the mat from fitting into the template. Another quality feature is the fibre mat length. Unfortunately it is not possible to have a dedicated measurement tool to determine the fibre mat length at high precision in each Winding Centre. As previously described, the end pieces are glued to the fibre mat with respect to each other and therefore fix the fibre mat length. During the optical cut, it is aimed to cut to the same end piece length. However, this is not possible and hence tolerances were fixed. The length of the end pieces can be used to calculate the fibre mat length[8].

The fibre mat is a very fragile object and cracks in the fibre mat pattern can appear. In the surrounding of a crack, the fibres always loose their accurate position and therefore this quality criterion is a very harsh one, as only one crack downgrades the mat to a C. The lamination on the two sides of the fibre mat lowers the risk of cracks appearing, but

---

[8]Assuming the end pieces have been glued to the correct position and under the correct environment conditions like temperature and humidity.
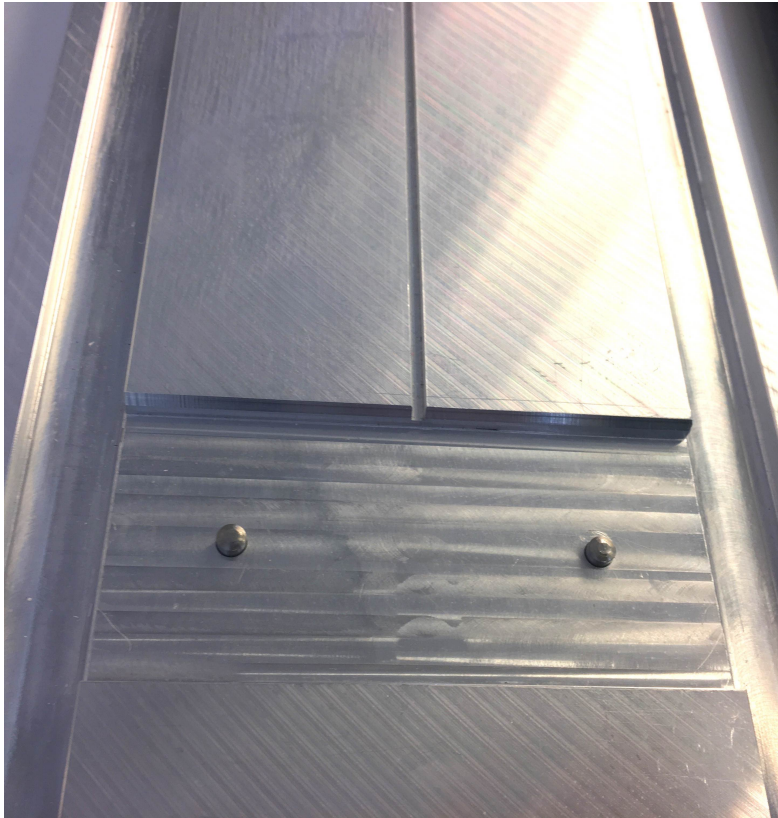
Fig. 7.53.: Geometry template. Placing the fibre mat into the jig makes sure that it will fit into the module template as well.

however until the second lamination procedure is done, the mat is unprotected and has only laminated one side. Even after lamination the mat is still fragile and needs to be handled carefully.

Pins on the fibre mat are mandatory to ensure a precise alignment during the module production. Unfortunately, it can happen that pins get lost during the unforming of the fibre mat off the wheel. Depending on how many and which pins are missing scores for this geometrical property get assigned. In Tab. 7.5, all geometrical scores are listed.

Tab. 7.5.: Grade assignment for geometrical measurements. The grades are assigned with letters from A to D, where A represents the highest and D the lowest grade. Four different properties are rated and the different scores listed.

Property	Grade	Specification
length	A	2424 mm-2424.5 mm
	B	2423 mm-2424 mm, but end pieces fit into jig
	C	<2423 mm, but end pieces fit into jig
	D	end pieces do not fit into jig
residual glue	A	no residual glue
	B	–
	C	–
	D	glue prevents mat from fitting into jig
cracks	A	no cracks
	B	–
	C	one or more cracks
	D	mat destroyed / unusable
pins	A	all pins present
	B	one or two non-adjacent pins missing
	C	3-4 pins (or two adjacent) pins missing
	D	more than 4 pins missing

7.6. Final assertion of quality grades

The quality grades are separated into performance scores and scores on geometrical properties. The final grade will represent both categories, so that it is composed of a letter (geometrical mark) and a number (performance mark). The performance scores are assigned with the results of the light yield measurement (Sec. 7.4) and optical scan (Sec. 7.3). The total performance mark will be the worse one from the two performance marks. Two examples for the final grade assertion are shown in Tab. 7.6. For example, a mat with a 1 in light yield and a 2 in the optical scan will receive a total performance mark of 2. The total geometrical score is assigned in the same way. The worse score sets the total score, such as a mat with an A in three of four categories, but a B in the last one, will have a B for a total geometrical score. Both total scores will get combined to a final score, hence this mat would have a B2 as final score. In addition, the light yield value is included. The measured light yield for each mat is rounded to an integer and appended to the geometry and performance grade. A proper comparison of the light yield values

Tab. 7.6.: Grade assignment for two example mats. For the total geometrical and performance marks always the lowest grade is chosen. Both grades get combined to a total one.

Mat	length	glue	cracks	pins	light yield	optical scan	Total
1	A	A	A	B	1	2	B2
2	A	C	A	B	3	2	C3

is ensured by applying correction factors, see Fig. 7.43. Assuming Mat 1's corrected light yield was measured to be 18.53 p.e. and for Mat 2 17.05 p.e., final marks would be

$$\text{Mat 1}: \quad \text{B2-19,}$$
$$\text{Mat 2}: \quad \text{C3-17.}$$

7.7. Summary & Outlook

The setups presented in this chapter were used to assure the quality of about 200 mats so far. They were almost continuously used since the start of the serial production in Dortmund in December 2016. All mats are measured in terms of light yield and geometry but also the optical scan is performed at both cutting edges. Studies have shown that the produced mats at all winding centres have a similar quality in terms of light yield.

The monitoring of the winding procedure assures the high quality of the fibre mats at the very beginning of the production chain. The result of the lamination and tempering procedures protect the fragile mats during handling. After the fibre mats are finished and get their final marks, they are sent to the module centre in Heidelberg to built the full size SciFi module.

All steps are running smoothly and a winding rate of 6 mats in Dortmund could be realised. No show stoppers are expected and the winding of fibre mats in Dortmund is currently foreseen to be completed by July.

8. Conclusion

The LHCb experiment at the LHC is dedicated to test the Standard Model of particle physics by investigating CP violation in the b and c quark sector as well as rare decays. Since 2010 the LHCb detector is collecting data, which enabled many key results that establish LHCb as the next generation flavour physics experiment. The LHCb upgrade that takes place in the LHC long shutdown 2 in 2019/20 will enable a major improvement of sensitivities to key observables in the indirect search for New Physics. This will be achieved by collecting a data sample of $50\,\mathrm{fb}^{-1}$ in ten years of operation. The upgraded detector will run with an increased instantaneous luminosity of $2 \cdot 10^{33}\,\mathrm{cm}^{-2}\,\mathrm{s}^{-1}$ and a readout rate of $40\,\mathrm{MHz}$. A new trigger scheme will remove current limitations given by the hardware trigger stage. In particular, analyses of decays with hadronic final states will benefit from this.

For the LHCb upgrade the tracking system behind the magnet will be replaced by the Scintillating Fibre Tracker. This tracking detector is based on thin scintillating fibres with silicon photomultiplier read out. The fibre mat serial production started in April 2016 with the first Winding Center, shortly followed by the module production in July 2016. Dortmund is one of the contributing institutes and started in December 2016 with the production of fibre mats. Currently 300 fibre mats have been wound in Dortmund with a rate of about 6 mats per week, as shown in Fig. 8.1. No show stoppers are expected and the fibre mat winding in Dortmund is currently foreseen to be finished by July.
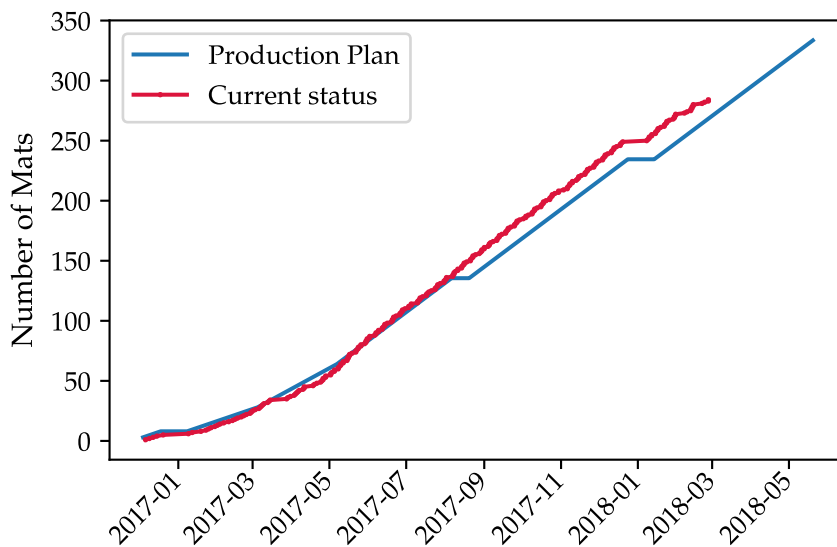

Fig. 8.1.: Progress of Fibre Mat Winding in Dortmund.

Reliable and standardised quality assurance procedures along the production line of the fibre mats are required. In addition, quality measurement methods and a mark assignment is necessary to judge the mat quality. During this thesis, quality assurance

procedures and quality measurement methods have been developed and were implemented in the serial production. Also quality determining test set ups have been set up for the Dortmund serial production as well as analysis their results.

Currently more than 1000 fibre mats have been wound and about 800 finished by all four winding centres. The successful and reliable quality assurance enabled a smooth running serial production with high quality fibre mats. In addition, these procedures helped to detect possible misbehaviours of the fibre mats as the fibre mat shrinking was detected at the beginning of the serial production. The measurement and analysis of the fibre mat shrinking presented in this thesis enabled to set a threshold for the end piece glueing procedure.

One key parameter of the LHCb SciFi Tracker is the hit efficiency. A high hit efficiency is achieved by low noise rates of the SiPMs and a high light yield of the scintillating fibres. Different studies on the light guidance of the scintillating fibres are presented in this thesis. It has been shown, that a heating of 80 °C reduces the light output immensely and that the tempering procedure with a temperature of 40 °C is not crucial. The amount of light reaching the fibre end is mainly reduced by radiation damage in the LHCb environment. An in situ irradiation campaign with a continuous monitoring of the light output has been presented in this thesis. The obtained results confirm previous irradiation campaigns and a light loss of about 40% at the end of the operation of the SciFi Tracker.

The studies presented in this thesis have been contributed for further R&D by the LHCb SciFi group and the serial production of fibre mats. Having the serial production running successfully sets the ground for installing the LHCb SciFi Tracker in the upcoming long shutdown 2 of the LHC.

A. Appendix

Fig. A.1.: Aluminium support, which holds the SiPMs and the fibre module. In addition it serves as mounting point for the installation in the cavern.

Fig. A.2.: Fibre module installed in the LHCb cavern at the shielding wall near the VELO.

Tab. A.1.: Fitting results of all measured fibre mats in terms of shrinking. For the first four mats just a single exponential function has been used, as the measurement was not directly started after unforming. The parameter t_{100} gives the time after which the mat will shrink only 100 μm.

Mat	a_1 / mm	b_1 / 1/day	b_2 / 1/day	c / mm	α / mm °C^{-1}	β / mm·%$^{-1}$	t_{off} / days	t_0 / days	t_{100} / days
12	0.405 ± 0.001	−0.323 ± 0.002		−0.4168 ± 0.0008	0.1271 ± 0.0007	0.014 09 ± 0.000 03	0.603 ± 0.002		4.33 ± 0.03
22	0.645 ± 0.001	−0.368 ± 0.001		−0.7585 ± 0.0011	0.6157 ± 0.0036	0.004 27 ± 0.000 02	0.460 ± 0.002		5.06 ± 0.01
23	0.677 ± 0.002	−0.101 ± 0.001		−0.6480 ± 0.0020	0.0921 ± 0.0003	0.005 52 ± 0.000 05	0.118 ± 0.003		18.89 ± 0.12
26	0.116 ± 0.001	−0.317 ± 0.004		−0.1123 ± 0.0006	0.1344 ± 0.0005	0.009 02 ± 0.000 02	0.205 ± 0.001		0.47 ± 0.02
42	1.429 ± 0.003	−1.115 ± 0.007	−0.1252 ± 0.0009	−2.1555 ± 0.0024	0.1270 ± 0.0005	0.012 06 ± 0.000 03	0.119 ± 0.001	0.701 ± 0.003	15.71 ± 0.11
51	1.715 ± 0.004	−3.280 ± 0.020	−0.2927 ± 0.0005	−1.9872 ± 0.0003	0.1093 ± 0.0001	0.012 43 ± 0.000 02	0.617 ± 0.002	0.258 ± 0.001	7.07 ± 0.03
54	1.962 ± 0.002	−0.714 ± 0.002	−0.1390 ± 0.0006	−2.5506 ± 0.0014	0.1404 ± 0.0003	0.014 92 ± 0.000 04	0.174 ± 0.001	1.381 ± 0.003	15.71 ± 0.07
63	2.331 ± 0.024	−0.590 ± 0.010	−0.0469 ± 0.0009	−2.9872 ± 0.0245	0.1353 ± 0.0005	0.012 76 ± 0.000 03	0.257 ± 0.001	0.610 ± 0.004	60.13 ± 1.12
72	1.659 ± 0.003	−1.616 ± 0.009	−0.3536 ± 0.0011	−2.2520 ± 0.0005	0.1058 ± 0.0002	0.014 38 ± 0.000 02	0.385 ± 0.001	0.490 ± 0.003	6.19 ± 0.02
88	1.834 ± 0.003	−0.956 ± 0.005	−0.1337 ± 0.0004	−2.4046 ± 0.0010	0.0953 ± 0.0002	0.018 07 ± 0.000 03	0.442 ± 0.002	0.712 ± 0.003	17.37 ± 0.06
105	1.540 ± 0.003	−1.101 ± 0.006	−0.2857 ± 0.0008	−2.2284 ± 0.0004	0.1177 ± 0.0002	0.014 91 ± 0.000 03	0.292 ± 0.002	0.671 ± 0.004	7.66 ± 0.03
127	2.214 ± 0.001	−0.480 ± 0.001	−0.0903 ± 0.0002	−2.9404 ± 0.0008	0.0760 ± 0.0002	0.013 76 ± 0.000 02	0.182 ± 0.001	1.430 ± 0.003	28.14 ± 0.05
148	2.055 ± 0.003	−1.010 ± 0.005	−0.2023 ± 0.0005	−2.5271 ± 0.0009	0.0695 ± 0.0003	0.012 38 ± 0.000 03	0.294 ± 0.003	0.664 ± 0.003	12.29 ± 0.04
161	1.884 ± 0.003	−2.640 ± 0.015	−0.3721 ± 0.0009	−2.2009 ± 0.0007	0.0598 ± 0.0002	0.009 76 ± 0.000 03	0.595 ± 0.002	0.243 ± 0.001	6.41 ± 0.02
173	1.999 ± 0.003	−6.945 ± 0.050	−1.0919 ± 0.0065	−2.0420 ± 0.0020	0.0707 ± 0.0004	0.006 86 ± 0.000 07	0.697 ± 0.002	0.071 ± 0.001	2.36 ± 0.01
179	1.794 ± 0.002	−1.333 ± 0.007	−0.1909 ± 0.0005	−2.4994 ± 0.0012	0.0836 ± 0.0002	0.011 80 ± 0.000 05	0.748 ± 0.003	0.521 ± 0.002	12.00 ± 0.04
240	1.458 ± 0.005	−2.876 ± 0.032	−0.4532 ± 0.0018	−1.9487 ± 0.0006	0.0987 ± 0.0001	0.009 96 ± 0.000 03	0.196 ± 0.001	0.281 ± 0.003	4.41 ± 0.03
262	1.436 ± 0.003	−1.084 ± 0.006	−0.1664 ± 0.0007	−2.0655 ± 0.0006	0.1023 ± 0.0002	0.011 53 ± 0.000 02	0.394 ± 0.001	0.779 ± 0.005	11.72 ± 0.06

Bibliography

[1] D.J. Griffiths, *Introduction to elementary particles; 2nd rev. version*, Physics textbook, New York, NY: Wiley, 2008, URL: https://cds.cern.ch/record/111880.

[2] D.H. Perkins, *Introduction to High Energy Physics*, Cambridge University Press, 2000, ISBN: 9780521621960, URL: https://books.google.de/books?id=e63cNigcmOUC.

[3] K. A. Olive et al., *Review of Particle Physics*, in: *Chin. Phys.* C38 (2014), DOI: 10.1088/1674-1137/38/9/090001.

[4] ATLAS Collaboration, *Observation of a new particle in the search for the Standard Model Higgs boson with the ATLAS detector at the LHC*, in: *Phys. Lett.* B716 (2012), DOI: 10.1016/j.physletb.2012.08.020, arXiv: 1207.7214 [hep-ex].

[5] CMS Collaboration, *Observation of a new boson at a mass of 125 GeV with the CMS experiment at the LHC*, in: *Phys. Lett.* B716 (2012), DOI: 10.1016/j.physletb.2012.08.021, arXiv: 1207.7235 [hep-ex].

[6] P. W. Higgs, *Broken symmetries, massless particles and gauge fields*, in: *Phys. Lett.* 12 (1964), DOI: 10.1016/0031-9163(64)91136-9.

[7] L. Evans and P. Bryant, *LHC machine*, in: *Journal of Instrumentation* 3.08 (2008), DOI: http://dx.doi.org/10.1088/1748-0221/3/08/S08001.

[8] F. Marcastel, *CERN's Accelerator Complex*, General Photo, Oct. 2013, URL: https://cds.cern.ch/record/1621583.

[9] ATLAS Collaboration, *The ATLAS Experiment at the CERN Large Hadron Collider*, in: *JINST* 3 (2008), DOI: 10.1088/1748-0221/3/08/S08003.

[10] CMS Collaboration, *The CMS Experiment at the CERN LHC*, in: *JINST* 3 (2008), DOI: 10.1088/1748-0221/3/08/S08004.

[11] ATLAS and CMS Collaboration, *Combined Measurement of the Higgs Boson Mass in pp Collisions at $\sqrt{s}$ = 7 and 8 TeV with the ATLAS and CMS Experiments*, in: *Phys. Rev. Lett.* 114 (2015), DOI: 10.1103/PhysRevLett.114.191803, arXiv: 1503.07589 [hep-ex].

[12] ALICE Collaboration, *The ALICE experiment at the CERN LHC*, in: *JINST* 3 (2008), DOI: 10.1088/1748-0221/3/08/S08002.

[13] LHCb Collaboration, *The LHCb detector at the LHC*, in: *Journal of Instrumentation* 3.08 (2008), DOI: http://dx.doi.org/10.1088/1748-0221/3/08/S08005.

[14] Planck collaboration, *Planck 2015 results. XIII. Cosmological parameters*, in: *Astron. Astrophys.* 594 (2016), DOI: 10.1051/0004-6361/201525830, arXiv: 1502.01589 [astro-ph.CO].

[15] LHCb Speakers Bureau, *Material for Presentations*, URL: http://lhcb.wmakeb.cern.ch/lhcb/speakersbureau/html/Material_for_Presentations.html.

[16] M. Pepe Altarelli and F. Teubert, *B Physics at LHCb*, in: *Int. J. Mod. Phys.* A23 (2008), DOI: 10.1142/S0217751X08042791, arXiv: 0802.1901 [hep-ph].

[17] LHCb Speakers Bureau, *b̄b production angle plots*, URL: https://lhcb.web.cern.ch/lhcb/speakersbureau/html/bb_ProductionAngles.html.

[18] Roel Aaij et al., *LHCb Detector Performance*, in: *Int. J. Mod. Phys.* A30.07 (2015), DOI: 10.1142/S0217751X15300227, arXiv: 1412.6352 [hep-ex].

[19] Ch. Ilgner et al., *The Beam Conditions Monitor of the LHCb Experiment*, in: (2010), arXiv: 1001.2487 [physics.ins-det].

[20] R. Arink et al., *Performance of the LHCb Outer Tracker*, in: *JINST* 9.01 (2014), DOI: 10.1088/1748-0221/9/01/P01002, arXiv: 1311.3893 [physics.ins-det].

[21] LHCb Collaboration, *LHCb Trigger Plots*, URL: https://twiki.cern.ch/twiki/bin/view/LHCb/LHCbTriggerConferenceDiagramsPlots.

[22] R. B. Palmer and J. C. Gallardo, *High-energy colliders*, in: *Critical problems in physics. Proceedings, Conference celebrating the 250th Anniversary of Princeton University, Princeton, USA, October 31-November 2, 1996*, 1997, arXiv: physics/9702016 [physics].

[23] LHCb Collaboration, *LHCb Operations Plots Webpage*, URL: http://www.lhcb-operationsplots.web.cern.ch/lhcb-operationsplots/index.htm.

[24] LHCb Collaboration, *Observation of J/ψp Resonances Consistent with Pentaquark States in $\Lambda_b^0 \to J/\psi K^- p$ Decays*, in: *Phys. Rev. Lett.* 115 (7 Aug. 2015), DOI: 10.1103/PhysRevLett.115.072001, URL: https://link.aps.org/doi/10.1103/PhysRevLett.115.072001.

[25] R Aaij et al., *Measurement of the CKM angle γ from a combination of $B^\pm \to Dh^\pm$ analyses*, in: *Phys. Lett.* B726 (2013), DOI: 10.1016/j.physletb.2013.08.020, arXiv: 1305.2050 [hep-ex].

[26] C. Cauet, *Precision measurement of the CKM parameter* sin(2β) *with the LHCb experiment*, PhD thesis, Tech. U., Dortmund, 2015-08-21, URL: http://inspirehep.net/record/1429405/files/fulltext_eG5tMF.pdf.

[27] LHCb Collaboration, *First Evidence for the Decay $B_s^0 \to \mu^+\mu^-$*, in: *Phys. Rev. Lett.* 110 (2 Jan. 2013), DOI: 10.1103/PhysRevLett.110.021801, URL: https://link.aps.org/doi/10.1103/PhysRevLett.110.021801.

[28] CMS Collaboration and LHCb Collaboration, *Observation of the rare $B_s^0 \to \mu^+\mu^-$ decay from the combined analysis of CMS and LHCb data*, in: *Nature* 522.7554 (June 2015), Letter, ISSN: 0028-0836, DOI: 10.1038/nature14474, URL: https://doi.org/10.1038/nature14474.

[29] LHCb Collaboration, *Letter of intent for the LHCb upgrade*, tech. rep. CERN-LHCC-2011-001. LHCC-I-018, Geneva: CERN, Mar. 2011, URL: https://cds.cern.ch/record/1333091.

[30] T. Gerson, *Updated sensitivity projections for the LHCb Upgrade*, tech. rep. LHCb-PUB-2013-015. CERN-LHCb-PUB-2013-015, Geneva: CERN, Sept. 2013, URL: https://cds.cern.ch/record/1604468.

[31] LHCb Collaboration, *LHCb Tracker Upgrade Technical Design Report*, tech. rep. CERN-LHCC-2014-001. LHCB-TDR-015, Feb. 2014, URL: http://cds.cern.ch/record/1647400.

[32] V. Gligorov, *Performance and Upgrade Plans of the LHCb Trigger System*, in: *Nucl. Instrum. Methods Phys. Res., A* 718.LHCb-PROC-2012-018. CERN-LHCb-PROC-2012-018 (June 2012), URL: https://cds.cern.ch/record/1443000.

[33] LHCb Collaboration, *LHCb VELO Upgrade Technical Design Report*, tech. rep. CERN-LHCC-2013-021. LHCB-TDR-013, Nov. 2013, URL: https://cds.cern.ch/record/1624070.

[34] LHCb Collaboration, *LHCb PID Upgrade Technical Design Report*, tech. rep. CERN-LHCC-2013-022. LHCB-TDR-014, Nov. 2013, URL: https://cds.cern.ch/record/1624074.

[35] Ph. d'Argent et al., *Improved performance of the LHCb Outer Tracker in LHC Run 2*, in: (2017), arXiv: 1708.00819 [physics.ins-det].

[36] M. Tobin, *The LHCb Silicon Tracker Performance in pp Collisions at the LHC*, in: *Proceedings, 13th ICATPP Conference on Astroparticle, Particle, Space Physics and Detectors for Physics Applications (ICATPP 2011): Como, Italy, October 3-7, 2011*, 2012, DOI: 10.1142/9789814405072_0102.

[37] T. Nakada, O. Ullaland, and W. Witzelling, *Expression of Interest for an LHCb Upgrade*, tech. rep. LHCC-G-139. CERN-LHCC-2008-007, Geneva: CERN, Apr. 2008, URL: https://cds.cern.ch/record/1100545.

[38] LHCb Collaboration, *Framework TDR for the LHCb Upgrade: Technical Design Report*, tech. rep. CERN-LHCC-2012-007. LHCb-TDR-12, Apr. 2012, URL: https://cds.cern.ch/record/1443882.

[39] B. Beischer et al., *A high-resolution scintillating fiber tracker with silicon photomultiplier array readout*, in: *Nucl. Instrum. Meth.* A622 (2010), DOI: 10.1016/j.nima.2010.07.059, arXiv: 1011.0226 [physics.ins-det].

[40] Kuraray, *Plastic Scintillating Fibers*, URL: http://kuraraypsf.jp/psf/index.html.

[41] M. Demmer, R. Ekelhof, and J. Wishahi, *Simulation of Light Yield Attenuation Maps for the LHCb SciFi Tracker Upgrade*, tech. rep. LHCb-INT-2016-015. CERN-LHCb-INT-2016-015, Geneva: CERN, Mar. 2016, URL: https://cds.cern.ch/record/2141533.

[42] D. Renker, *Geiger-mode avalanche photodiodes, history, properties and problems*, in: 567.1 (Nov 2006).

[43] A. Kuonen et al., *LHCb Scintillating Fibre Tracker Engineering Design Review: Silicon Photomultipliers*, tech. rep. LHCb-INT-2016-019. CERN-LHCb-INT-2016-019, Geneva: CERN, Apr. 2016, URL: https://cds.cern.ch/record/2147853.

[44] Ch. Joram et al., *LHCb Scintillating Fibre Tracker Engineering Design Review Report: Fibres, Mats and Modules*, tech. rep. LHCb-PUB-2015-008. CERN-LHCb-PUB-2015-008, Geneva: CERN, Mar. 2015, URL: https://cds.cern.ch/record/2004811.

[45] N. Meinert, J. Van Tilburg, and H. Viemann, *Geometry description of the SciFi detector in the LHCb simulation*, tech. rep. LHCb-INT-2017-027. CERN-LHCb-INT-2017-027, Geneva: CERN, Oct. 2017, URL: https://cds.cern.ch/record/2289871.

[46] U. Uwer, *Revised SciFi stereo-layer geometry*, tech. rep. LHCb-INT-2017-010. CERN-LHCb-INT-2017-010, Geneva: CERN, May 2017, URL: https://cds.cern.ch/record/2264922.

[47] B. Leverington, *C-Frames: Mechnics and Services*, SciFi General Meeting.

[48] A. Rodrigues Cavalcante et al., *LHCb Scintillating Fibre Tracker: Test Beam Report 2015*, tech. rep. LHCb-PUB-2015-025. CERN-LHCb-PUB-2015-025, Geneva: CERN, Nov. 2015, URL: https://cds.cern.ch/record/2108337.

[49] Ph. Azzarello, *Tests and production of the AMS-02 silicon tracker detectors*, PhD thesis, Geneva U., 2004, URL: http://inspirehep.net/record/922933/files/AZZARELLO_these.pdf.

[50] K. Akiba et al., *The Timepix Telescope for High Performance Particle Tracking*, in: *Nucl. Instrum. Meth.* A723 (2013), DOI: 10.1016/j.nima.2013.04.060, arXiv: 1304.5175 [physics.ins-det].

[51] L. An et al., *Testbeam analysis for a scintillating fibre telescope*, tech. rep. LHCb-INT-2016-042. CERN-LHCb-INT-2016-042, Geneva: CERN, Oct. 2016, URL: https://cds.cern.ch/record/2219595.

[52] Ch. Joram, *SciFi Tracker Planning*, URL: https://twiki.cern.ch/twiki/bin/view/LHCb/SciFiTrackerPlanning.

[53] Ch. Joram, *Technical specifications of the scintillating fibres*, tech. rep. LHCb-PUB-2014-019. CERN-LHCb-PUB-2014-019. LHCb-INT-2013-061, Geneva: CERN, Feb. 2014, URL: https://cds.cern.ch/record/1662541.

[54] A. Rodigues Cavalcante et al., *Scanners for the quality contol of scintillating plastic fibres*, tech. rep. LHCb-PUB-2015-009. CERN-LHCb-PUB-2015-009, Geneva: CERN, Apr. 2015, URL: https://cds.cern.ch/record/2009352.

[55] A. Rodrigues Cavalcante et al., *Shrinking of bumps by drawing scintillating fibres through a hot conical tool*, tech. rep. LHCb-PUB-2016-010. CERN-LHCb-PUB-2016-010, Geneva: CERN, Apr. 2016, URL: https://cds.cern.ch/record/2144875.

[56] R. Ekelhof, *Studies for the LHCb SciFi Tracker - Development of Modules from Scintillating Fibres and Tests of their Radiation Hardness*, PhD thesis, TU Dortmund, 2016-03-31, URL: http://inspirehep.net/record/1503590/files/CERN-THESIS-2016-098.pdf.

[57] B. Leverington, private communication, Feb. 17, 2015.

[58] H. Leutz, *Scintillating fibres*, in: *Nuclear Instruments and Methods in Physics Research Section A: Accelerators, Spectrometers, Detectors and Associated Equipment* 364.3 (1995), ISSN: 0168-9002, DOI: https://doi.org/10.1016/0168-9002(95)00383-5, URL: http://www.sciencedirect.com/science/article/pii/0168900295003835.

[59] F.D. Brooks, *Development of organic scintillators*, in: *Nuclear Instruments and Methods* 162.1 (1979).

[60] I.B. Berlman, *Handbook of fluorescence spectra of aromatic molecules; 2nd ed.* New York, NY: Academic Press, 1971, URL: https://cds.cern.ch/record/108019.

[61] L.J. Basile, *Transfer of excitation energy in rigid solutions of organic scintillators*, in: *Trans. Faraday Soc.* 60 (0 1964), DOI: 10.1039/TF9646001702, URL: http://dx.doi.org/10.1039/TF9646001702.

[62] Th. Förster, *Zwischenmolekulare Energiewanderung und Fluoreszenz*, in: *Annalen der Physik* 437.1-2 (1948), ISSN: 1521-3889, DOI: 10.1002/andp.19484370105, URL: http://dx.doi.org/10.1002/andp.19484370105.

[63] M. Deckenhoff, *Scintillating Fibre and Silicon Photomultiplier Studies for the LHCb upgrade*, PhD thesis, TU Dortmund, 2015-12-22, URL: http://inspirehep.net/record/1503898/files/CERN-THESIS-2015-318.pdf.

[64] P. Rebourgeard et al., *Fabrication and measurements of plastic scintillating fibers*, in: *Nuclear Instruments and Methods in Physics Research Section A: Accelerators, Spectrometers, Detectors and Associated Equipment* 427.3 (1999), issn: 0168-9002, doi: https://doi.org/10.1016/S0168-9002(99)00053-4, url: http://www.sciencedirect.com/science/article/pii/S0168900299000534.

[65] J.S. Wallace et al., *Color center annealing in γ - irradiated polystyrene, under vacuum and air atmospheres*, vol. 41, Feb. 1993.

[66] A. Bross and A. Pla-Dalmau, *Radiation Damage of Plastic Scintillators*, vol. 39, Nov. 1992.

[67] W. Busjan, K. Wick, and T. Zoufal, *Shortlived absorption centers in plastic scintillators and their influence on the fluorescence light yield*, in: *Nuclear Instruments and Methods in Physics Research Section B: Beam Interactions with Materials and Atoms* 152.1 (1999), issn: 0168-583X.

[68] T. Soestwöhner, *Messung der Winkelverteilung der austretenden Photonen am Ende von szintillierenden Fasern für den SciFi-Tracker des LHCb-Experiments*, Bachelor thesis, Technische Universität Dortmund, 2014.

[69] J. Broll, *Simulation der Winkelverteilung der austretenden Photonen am Ende von szintillierenden Fasern für den SciFi-Tracker des LHCb-Experiments*, Bachelor thesis, Technische Universität Dortmund, 2014.

[70] R. Manderfeld, *in preparation*, Master thesis, Technische Universität Dortmund, 2018.

[71] A. Ferrari et al., *FLUKA: a multi-particle transport code*, in: *CERN 2005-10 (2005), INFN/TC 05/11, SLAC-R-773*.

[72] M. Karacson, private communication, Sept. 25, 2017.

[73] Y. LeCun and Y. Bengio, *The Handbook of Brain Theory and Neural Networks*, in: Cambridge, MA, USA: MIT Press, 1998, chap. Convolutional Networks for Images, Speech, and Time Series, isbn: 0-262-51102-9, url: http://dl.acm.org/citation.cfm?id=303568.303704.

[74] A.P. Bradley, *The use of the area under the ROC curve in the evaluation of machine learning algorithms*, in: *Pattern Recognition* 30 (1997).

[75] C.E. Metz, *CE: Basic principles of ROC analysis*, in: *Seminars in Nuclear Medicine*, 1978.

[76] S. Swientek, *Mechanische Belastungen von szintillierenden Fasern*, Diplomarbeit, Technische Universität Dortmund, 2010.

[77] J. Travis and J. Kring, *LabVIEW for Everyone: Graphical Programming Made Easy and Fun*, Upper Saddle River, NJ, USA: Prentice Hall PTR, 2006, isbn: 0131856723.

[78] D.R. Askeland, *The science and engineering of materials*, Cengage Learning, 2006, isbn: 978-0-495-29602-7.

[79] S. Brooks et al., *Handbook of Markov Chain Monte Carlo*, Chapman & Hall/CRC Handbooks of Modern Statistical Methods, CRC Press, 2011, isbn: 9781420079425, url: https://books.google.de/books?id=qfRsAIKZ4rIC.

[80] J. Müller, *Entwicklung einer Qualitätskontrolle von Matten aus szintillierenden Fasern für den LHCb SciFi Tracker*, Master thesis, Technische Universität Dortmund, 2014.

[81] R. Greim, *Sr90 updates and improvements*, Fibre Mat Production Meeting.

Acknowledgements (Danksagung)

Zu Beginn meines Studiums habe ich Stefanie Roese kennen gelernt. Auch wenn ich sie leider nach unserem Bachelor an die Festkörperphysik verloren habe, freue ich mich immer auf unsere wöchentlichen Kaffeemeetings und habe eine sehr, sehr gute Freundin gewonnen.

Außerhalb der Arbeit haben mir vor allem Frederik Möller und Daniela Fink geholfen meinen Stress mithilfe von Sport abzubauen und mal nicht über Physik sprechen zu müssen. Vielen Dank dafür.

Meiner Familie möchte ich für die Unterstützung während meines Studiums und der Promotion danken. Vielen Dank für euer Vertrauren, eure Liebe, Motivation und Support in jeder Lebenslage.

Zu guter Letzt danke ich Thorben Menne. Vielen Dank für deinen Rückhalt, deine Unterstützung, deine Liebe und das gelegentliche Auffangen und Wiederaufbauen in Zeiten von Frustration und Stress. Mit dem Einreichen dieser Arbeit lässt sich unsere bevorstehende Hochzeit noch viel besser genießen.